Title

Spatially Quasi-Periodic Gravity-Capillary Waves

Author

Zhao, Xinyu

Publication Date

2021

Peer reviewed|Thesis/dissertation

Spatially Quasi-Periodic Gravity-Capillary Waves

by

Xinyu Zhao

A dissertation submitted in partial satisfaction of the

requirements for the degree of

Doctor of Philosophy

in

Applied Mathematics

in the

Graduate Division

of the

University of California, Berkeley

Committee in charge:

Professor Jon Wilkening, Chair
Professor Daniel Tataru
Professor Panayiotis Papadopoulos

Spring 2021

Spatially Quasi-Periodic Gravity-Capillary Waves

Abstract

Spatially Quasi-Periodic Gravity-Capillary Waves

by

Xinyu Zhao

Doctor of Philosophy in Applied Mathematics

University of California, Berkeley

Professor Jon Wilkening, Chair

In this thesis, we study the problem of two dimensional spatially quasi-periodic gravity-capillary waves on the surface of an ideal fluid of infinite depth. We formulate the water wave equations in a spatially quasi-periodic setting and present a numerical study of solutions of both the initial value problem and the traveling wave problem. We propose a Fourier pseudo-spectral discretization of the equations of motion in which one dimensional quasi-periodic functions are represented by two dimensional periodic functions on a torus. We adopt a conformal mapping formulation and employ a quasi-periodic version of the Hilbert transform to determine the normal velocity of the free surface. Two time-stepping schemes of the initial value problem are proposed, an explicit Runge-Kutta (ERK) method and an exponential time-differencing (ETD) scheme. We present an example of a periodic wave profile containing vertical tangent lines that is set in motion with a quasi-periodic velocity potential. We formulate the traveling wave problem as a nonlinear least squares problem that we solve using a variant of the Levenberg-Marquardt method. Two types of quasi-periodic traveling solutions are computed: small-amplitude solutions that bifurcate from the zero solution and large-amplitude solutions that bifurcate from finite-amplitude periodic traveling solutions. Solutions of the first type are identified by two bifurcation parameters. We also compute the leading terms of the asymptotic expansion of the solution using these parameters. For solutions of the second type, we apply the Fourier-Bloch decomposition to study the linearization around periodic traveling solutions and obtain a one-parameter family of quasi-periodic solutions bifurcating from the branch of periodic solutions. As an example, we compute a branch of quasi-periodic overturning traveling solutions that bifurcate from a periodic overturning traveling solution.

To everyone who accompanied me in my journey.

Contents

List of Figures

List of Tables

Acknowledgments

First and foremost, I wish to thank my advisor Jon Wilkening for his guidance and support throughout my graduate studies. His cheerful and helpful attitude towards others made it a very enjoyable experience. I am grateful to my committee, including Daniel Tataru and Panayiotis Papadopoulos, for their guidance throughout my graduate studies. It was a great pleasure to learn about partial differential equations from Daniel Tataru. I was impressed by his vast knowledge on the subject and his good sense of humor. I also appreciate all the support I received from my family and my friends; they trusted every decision I made and were always there for me in my time of need. Lastly, I would like to thank Ritvik Ramkumar, raccoons, skunks and deers for accompanying me on my way home at nights.

Chapter 1

Introduction

In fluid dynamics, gravity-capillary waves are surface waves generated by the restoring effects of both gravity and surface tension [4]. The motion of these waves on a fluid of arbitrary depth is described by the Euler equations. There have been many wave models derived as approximations of Euler equations, such as the Korteweg-De-Vries (KdV) equation and the Kawahara equation in the shallow water regime, and the nonlinear Schrodinger equation in the deep water regime. These equations are usually studied under the periodic boundary condition or the assumption that the solution decays to zero at infinity [29, 54, 77]. However, in many situations, assuming the waves decay to zero at infinity is not a realistic model. For example, a large body of water such as the ocean is often covered in surface waves in every direction over vast distances. Similarly, assuming spatial periodicity may limit one's ability to observe interesting dynamics. The goal of this thesis is to study free surface Euler equations under the assumption that the solutions only satisfy spatially quasi-periodic boundary conditions. Particularly, we introduce a conformal mapping formulation of the wave equations in this setting and develop numerical methods to compute solutions of the initial value problem as well as the traveling wave problem.

The Modulational Instability and Quasi-Periodic Dynamics of Water Waves

In 1847, Stokes [70] proposed the existence of periodic traveling gravity waves on deep water and constructed asymptotic expansions of these waves. The convergence of the Stokes expansion was first proved by Levi-Civita [55] in 1925 and extended by Struik [71] to traveling waves on water of finite depth in 1926. Even though the existence of Stokes waves was established, the instability of Stokes waves went unnoticed for a long time. In 1967, Benjamin and Feir [14] first discovered that the Stokes waves are unstable under long-wave perturbations; they observed that the nonlinear interactions between the perturabation and the Stokes wave led to exponential growth of the wave perturbation. This is called the modulational instability, or Benjamin-Feir instability, which is believed to be a mechanism responsible for the formation of rogue waves [1, 66, 67]. Modulational

instability has been proved by Bridges and Mielke [20] for the case of finite depth water and Nguyen and Strauss [64] recently for the case of deep water.

Modulational instability is usually studied by examining the subharmonic stability of periodic traveling waves, where the wavelength of the perturbation is longer than the original traveling wave [31, 57, 73]. One can obtain the full spectrum of the stability problem using a Fourier-Bloch decomposition, where the eigenfunctions of the linearization around a periodic traveling wave possess a spatial period different from the traveling wave [72]. The time evolution of traveling waves under subharmonic perturbations leads to spatially quasi-periodic dynamics, which is usually computed by linear approximation [31]. No method currently exists to compute the exact nonlinear motion, which includes the complicated interactions between wave modes of different wavelengths. In this thesis, we develop numerical methods to compute the exact solutions of the wave equations under spatially quasi-periodic initial conditions. This method makes it possible to study the dynamics of perturbed traveling waves in the fully nonlinear setting and can also be used to improve the accuracy of wave forecasting, where the wave motion is usually computed through weakly nonlinear models [52].

Recently, the quasi-periodic dynamics of water waves have drawn considerable attention. Berti and Montalto [17] and Baldi et. al. [13] used Nash-Moser theory to prove the existence of small-amplitude temporally quasi-periodic gravity-capillary standing waves. With different assumptions on the form of solutions, Berti et. al. [16] have proved the existence of time quasi-periodic gravity-capillary waves with constant vorticity while Feola and Giuliani [41] have proved the existence of time quasi-periodic irrotational gravity waves. New families of relative-periodic [80] and traveling-standing [81] water wave solutions have been computed by Wilkening. As with [13, 16, 17, 41], these solutions are quasi-periodic in time rather than space. For spatially quasi-periodic waves, there are studies of the well-posedness of solutions of the KdV equation [30] and the Schrodinger equation [32]; however, to our knowledge, the spatially quasi-periodic gravity-capillary wave problem has not been studied previously in the fully nonlinear regime.

Spatially Quasi-Periodic Traveling Waves

The dispersion relation for linearized traveling gravity-capillary waves in deep water reads

$$c^2 = gk^{-1} + \tau k. \tag{1.1}$$

Here c is the phase speed, k is the wave number, g is the acceleration due to gravity and τ is the coefficient of surface tension. Notice that $c = \sqrt{(g/k) + \tau k}$ has a positive minimum, denoted by c_{crit}. For any fixed phase speed $c > c_{\text{crit}}$, there are two distinct positive wave numbers satisfying the dispersion relation (1.1), denoted k_1 and k_2. Any traveling solution of the linearized problem with this speed can be expressed as a superposition of waves with these wave numbers. If k_1 and k_2 are rationally related, the motion is spatially periodic and corresponds to the well-known Wilton ripples [2, 5, 73, 85]. However, if k_1

and k_2 are irrationally related, the motion will be spatially quasi-periodic. Thus it is natural to ask whether the solution of the linearized problem in this case can be perturbed to quasi-periodic traveling solutions of the nonlinear problem.

Bridges and Dias [19] first studied quasi-periodic traveling gravity-capillary waves as small-amplitude perturbations of the solution of the linearized problem; they used a spatial Hamiltonian structure to construct weakly nonlinear approximations of these waves for two special cases: deep water and shallow water. The existence of such waves is still an open problem. In this thesis, we demonstrate their existence numerically and explore their properties. Unlike [19], we use a conformal mapping formulation [26, 33, 34, 36, 37, 49, 56, 87] of the gravity-capillary wave problem. Particularly, we consider the conformal mapping that maps the lower half plane to the fluid domain such that the real line is mapped to the free surface. This makes it possible to compute the normal velocity of the fluid from the velocity potential on the free surface via a quasi-periodic variant of the Hilbert transform. Analogous to the periodic case, the Hilbert transform is a Fourier multiplier operator that acts on functions defined on a higher-dimensional torus.

We first study the problem of quasi-periodic traveling waves in the setting of a bifurcation problem with a two-dimensional kernel, where the solutions are considered as bifurcations from the zero solution. These solutions are close to the solution of the linearized problem and are of relatively small amplitudes due to small divisors. Next we proceed to compute large-amplitude quasi-periodic traveling waves by searching for quasi-periodic bifurcations of finite-amplitude periodic traveling waves. This is motivated by the study of periodic secondary bifurcations of Stokes waves. In [22], Buffoni, Dancer and Toland showed that for each sufficiently large value of the integer n, there exists a secondary bifurcation branch of solutions of period $2n\pi$ bifurcating from a 2π periodic solution. Chen and Saffman [24] computed subharmonic bifurcations corresponding to $n = 2, 3$. Vanden-Broeck [76] further extended their results to $n = 9$ and provided numerical evidence that the bifurcated solution approaches a non-periodic wave when n approaches infinity; this limit configuration is no longer periodic. We further extend their ideas to quasi-periodic secondary bifurcations and obtain quasi-periodic overturning traveling waves that bifurcate from periodic traveling waves.

An Overview of The Thesis

In this thesis, we study the problem of two-dimensional spatially quasi-periodic gravity-capillary waves on the surface of an ideal fluid of infinite depth, including the initial value problem and the traveling wave problem. The thesis consists of three main sections: equations of motion for spatially quasi-periodic waves, the problem of quasi-periodic traveling waves and the corresponding numerical methods and results.

In Chapter 2, we introduce the definition of quasi-periodic functions and discuss the equations of motion for spatially quasi-periodic gravity-capillary waves. Following the definitions in [40, 62], we represent a quasi-periodic function of d quasi-periods in terms of a periodic function defined on the torus $\mathbb{T}^d$. We present the usual graph-based formulation

as well as the conformal mapping formulation of the governing equations in the spatially quasi-periodic setting. We also derive the corresponding equations of motion on the torus. We demonstrate that by using the conformal mapping method, one can reduce the computation of the Dirichlet-Neumann operator to the computation of a Hilbert transform, which is essentially a Fourier multiplier operator and easy to compute in Fourier space. We show that similar to the periodic case, the equations of motion for spatially quasi-periodic waves can be written as a canonical Hamiltonian system in physical variables and non canonical Hamiltonian system in conformal variables; we also discuss the conserved quantities such as energy, momentum and mass in both formulations.

In Chapter 3, we study the problem of quasi-periodic traveling waves using the conformal mapping formulation of governing equations and focus on solutions with two quasi-periods. We examine the linearization of the governing equations around the zero solution and construct asymptotic expansions of the quasi-periodic traveling solutions that are small-amplitude perturbations of the linear solution. The computation of the expansion inevitably leads to small divisor problems; as a consequence, the amplitudes of the solutions have to be relatively small to overcome the unboundedness caused by small divisors. The convergence of expansions is still an open problem as one would need to overcome the small divisor problem in a proof. Besides small-amplitude solutions, we also discuss how to obtain quasi-periodic traveling solutions of relatively large amplitudes. The idea is to search for quasi-periodic bifurcations of finite-amplitude periodic traveling solutions. We adopt a Fourier-Bloch decomposition to study the linearization. This method has been used in the studies of the subharmonic stability of traveling waves [31]. These solutions are of relatively large amplitudes and far from the linear solution.

In Chapter 4, we develop numerical methods for both the initial value problem and the traveling wave problem discussed in Chapters 2 and 3. The basic idea is to perform the computations on the torus version of the quasi-periodic water wave equations using a Fourier pseudo-spectral method and reconstruct quasi-periodic functions from periodic functions on the torus. In the computations, we focus on quasi-periodic functions with two quasi-periods. For the initial value problem, we present a high-order explicit Runge-Kutta method and an exponential time-differencing (ETD) method. The former is suitable for the case of zero or small surface tension while the latter makes use of the small-scale decomposition [47, 48] to eliminate stiffness due to surface tension. The conformal mapping method has not been implemented in an ETD framework before, even for periodic boundary conditions. We present a convergence study of the methods as well as a large-scale computation of a quasi-periodic wave in which some of the wave crests overturn. Due to the torus representation of solutions, there are infinitely many wave crests and no two of them evolve in exactly the same way. For the traveling wave problem, we formulate the traveling wave computation as a nonlinear least-squares problem and use the Levenberg-Marquardt method to search for solutions. This approach builds on the overdetermined shooting methods developed by Wilkening and collaborators [8, 9, 43, 69, 82] to compute standing waves and other time-periodic solutions. We show that the spatially quasi-periodic traveling waves that bifurcate from the zero-amplitude wave

come in two-parameter families in which the amplitudes of the base modes with wave numbers k_1 and k_2 satisfying (1.1) serve as bifurcation parameters. The wave speed and surface tension depend nonlinearly on these parameters as well. We also compute a set of periodic traveling solutions where there exist quasi-periodic bifurcations and obtain large-amplitude quasi-periodic overturning traveling waves when surface tension effects are stronger than gravitational effects.

Chapter 2

Equations of Motion

2.1 Governing Equations in Physical Space

2.1.1 The Two Dimensional Free Surface Euler Equations

We study the problem of two-dimensional gravity-capillary waves on the surface of an ideal fluid of infinite depth. An ideal fluid is a fluid that is incompressible, irrotational and inviscid. We assume that the density of the fluid, denoted by ρ, is a fixed constant that does not depend on time or space. We define the fluid domain by

$$\Omega_\eta := \{\boldsymbol{x} = (x, y) : -\infty < y < \eta(x, t), \quad x \in \mathbb{R}\}, \tag{2.1}$$

where $\eta(x, t)$ is the free surface elevation that changes with time. We denote the velocity field of the fluid as $\boldsymbol{u} = (u, v)^T$, which satisfies the following incompressible Euler equations [27]

$$\begin{cases} \boldsymbol{u}_t + \boldsymbol{u} \cdot \nabla \boldsymbol{u} + \nabla(\frac{P}{\rho} + gy) = 0, \\ \nabla \cdot \boldsymbol{u} = 0, \end{cases} \tag{2.2}$$

where $\nabla = (\partial_x, \partial_y)^T$, g is the acceleration of gravity and $P : \Omega_\eta \to \mathbb{R}$ is the pressure. We also assume that $v \to 0$ when $y \to -\infty$, which is compatible with the impenetrable condition for fluid of finite depth.

We pose two boundary conditions on the free surface. The first one is called the kinematic boundary condition, which states that the fluid particles on the free surface always remain on the free surface; this implies that the normal velocity of the fluid particles and the free surface should be the same. Therefore we have

$$(0, \eta_t)^T \cdot \boldsymbol{n} = \boldsymbol{U} \cdot \boldsymbol{n}, \qquad \boldsymbol{U} = (U, V)^T = \boldsymbol{u}|_{y=\eta}, \tag{2.3}$$

where

$$\boldsymbol{n} = \frac{1}{\sqrt{1 + \eta_x^2}}(-\eta_x, 1)^T \tag{2.4}$$

is the outward unit norm on the free surface. The above equation can be simplified to

$$\eta_t = \sqrt{1+\eta_x^2}\boldsymbol{U}\cdot\boldsymbol{n}. \tag{2.5}$$

The second boundary condition is with regard to the force equilibrium at the free surface: the force due to the surface tension balances the outward force due to the pressure difference between the fluid and air. If we assume that the air pressure is zero without loss of generality, then we have

$$P|_{y=\eta} = -\rho\tau\kappa, \tag{2.6}$$

where τ is the surface tension coefficient and

$$\kappa = \partial_x\left(\frac{\eta_x}{\sqrt{1+\eta_x^2}}\right) \tag{2.7}$$

is the mean curvature. This condition is called the dynamic boundary condition.

Since the fluid is irrotational, we have

$$\operatorname{curl}\boldsymbol{u} = u_y - v_x = 0. \tag{2.8}$$

Using the fact that the fluid domain is simply connected, we know that there exists a function Φ such that

$$\boldsymbol{u} = \nabla\Phi. \tag{2.9}$$

The function Φ is called the velocity potential. Substituting the above equation into the incompressible Euler equations (2.2), we obtain

$$\begin{cases}\Phi_t + \frac{1}{2}|\nabla\Phi|^2 + gy + \frac{P}{\rho} = C(t),\\ \Phi_{xx}+\Phi_{yy} = 0.\end{cases} \tag{2.10}$$

The first equation is called the Bernoulli's equation and the function $C(t)$ is an arbitrary integration constant which is allowed to depend on time but not space. On the free surface, the substitution of the dynamic boundary condition (2.6) into the Bernoulli's equation gives

$$\Phi_t + \frac{1}{2}|\nabla\Phi|^2 + gy - \tau\kappa = C(t), \qquad y = \eta(x,t). \tag{2.11}$$

The second equation of (2.10) shows that Φ is a harmonic function in the fluid domain. We define

$$\varphi(x,t) = \Phi(x,\eta(x,t)), \tag{2.12}$$

which is the boundary value of the velocity potential on the free surface. The time evolution of φ is given by (2.11). Knowing φ, one can obtain Φ by solving the following

Dirichlet-Neumann boundary value problem

$$\begin{cases} \Phi_{xx} + \Phi_{yy} = 0, & -\infty < y < \eta(x,t), \\ \Phi = \varphi, & y = \eta(x,t), \\ \Phi_y \to 0, & y \to -\infty. \end{cases} \tag{2.13}$$

The motion of the waves is also determined by the evolution of the free surface elevation η, which is obtained by substituting (2.11) into the kinematic boundary condition (2.5)

$$\eta_t = \Phi_y - \eta_x \Phi_x, \qquad y = \eta(x,t). \tag{2.14}$$

In summary, the motion of gravity-capillary waves is governed by the two-dimensional free-surface Euler equations [29,86]

$$\eta(x,0) = \eta_0(x), \qquad \varphi(x,0) = \varphi_0(x), \qquad t = 0, \quad x \in \mathbb{R}, \tag{2.15}$$

$$\begin{aligned} \Phi_{xx} + \Phi_{yy} = 0, &\qquad -\infty < y < \eta(x,t), \\ \Phi = \varphi, &\qquad y = \eta(x,t), \\ \Phi_y \to 0, &\qquad y \to -\infty, \end{aligned} \tag{2.16}$$

$$\eta_t = \Phi_y - \eta_x \Phi_x, \qquad y = \eta(x,t), \tag{2.17}$$

$$\varphi_t = \Phi_y \eta_t - \frac{1}{2}\Phi_x^2 - \frac{1}{2}\Phi_y^2 - g\eta + \tau\kappa + C(t), \qquad y = \eta(x,t). \tag{2.18}$$

Following [29,86], only the surface variables η and φ are evolved in time; the velocity potential Φ in the bulk fluid is reconstructed from η and φ by solving (2.16), which causes the problem to be nonlocal. In [29], Craig and Sulem showed that one can write the whole system in terms of η and φ only. To do so, they introduce the Dirichlet-Neumann operator

$$G(\eta)\varphi = \Phi_y - \eta_x \Phi_x|_{y=\eta}. \tag{2.19}$$

This operator relates the function φ, defined on the free surface, to the normal derivative of its harmonic extension Φ on the free surface. The differentiation of (2.12) with respect to x yields

$$\varphi_x = \Phi_x + \Phi_y \eta_x, \qquad y = \eta(x,t). \tag{2.20}$$

Combining the equation above with $G(\eta)\varphi$, one can obtain

$$\begin{pmatrix} \varphi_x \\ G(\eta)\varphi \end{pmatrix} = \begin{pmatrix} 1 & \eta_x \\ -\eta_x & 1 \end{pmatrix} \begin{pmatrix} \Phi_x \\ \Phi_y \end{pmatrix}, \qquad y = \eta(x,t). \tag{2.21}$$

Therefore the velocity of the fluid particles on the free surface can be expressed by

$$U = \Phi_x = \frac{1}{1+\eta_x^2}(\varphi_x - \eta_x G(\eta)\varphi), \qquad V = \Phi_y = \frac{1}{1+\eta_x^2}(\eta_x \varphi_x + G(\eta)\varphi). \tag{2.22}$$

Substituting the above equations into (2.17) and (2.18), we obtain the time evolution equations of η_t and φ_t

$$\begin{aligned} \eta_t &= G(\eta)\varphi, \\ \varphi_t &= \frac{1}{2}\left(\frac{\left(G(\eta)\varphi + \eta_x\varphi_x\right)^2}{1+\eta_x^2} - \varphi_x^2\right) - g\eta + \tau\kappa + C(t). \end{aligned} \tag{2.23}$$

2.1.2 Governing Equations of Spatially Quasi-Periodic Waves

As defined in [40, 62], a quasi-periodic, real analytic function $f(x)$ is a function of the form

$$f(x) = \tilde{f}(\boldsymbol{k}x), \qquad \tilde{f}(\boldsymbol{x}) = \sum_{j\in\mathbb{Z}^d} \hat{f}_j e^{i\langle j, x\rangle}, \qquad x \in \mathbb{R}, \quad \boldsymbol{x}, \boldsymbol{k} \in \mathbb{R}^d, \tag{2.24}$$

where $\langle\cdot,\cdot\rangle$ denotes the standard inner product in $\mathbb{R}^d$ and $\tilde{f}$ is a periodic, real analytic function defined on the d-dimensional torus

$$\mathbb{T}^d := \mathbb{R}^d \Big/ (2\pi\mathbb{Z})^d, \qquad d \geq 2. \tag{2.25}$$

Entries of the vector $\boldsymbol{k}$ are called the basic wave numbers (or basic frequencies) of f and are required to be linearly independent over $\mathbb{Z}$ to exclude periodic functions. If $\boldsymbol{k}$ is given, one can reconstruct the Fourier coefficient $\hat{f}_j$ from f via

$$\hat{f}_j = \lim_{a\to\infty} \frac{1}{2a} \int_{-a}^{a} f(\alpha) e^{-i\langle j,k\rangle x}\, dx, \qquad j \in \mathbb{Z}^d. \tag{2.26}$$

A similar averaging formula holds for functions in the more general class of almost periodic functions [10, 18, 42, 45, 62], which is the closure with respect to uniform convergence on $\mathbb{R}$ of the set of trigonometric polynomials $p(x) = \sum_{n=1}^{N} c_n e^{i\kappa_n x}$. Before taking limits to obtain the closure, this set includes polynomials of any degree and there is no restriction on the real numbers κ_n. Within the framework of almost periodic functions, one obtains quasi-periodic functions if one assumes the κ_n in the approximating polynomials are integer linear combinations of a fixed, finite set of basic wave numbers $k_1, \ldots, k_d$.

We have not attempted to formulate the water wave problem in the full generality of almost periodic functions, and instead assume the basic wave numbers are given and the torus representation (2.24) is available. Thus, the average over $\mathbb{R}$ on the right-hand side of (2.26) can be replaced by the simpler Fourier coefficient formula

$$\hat{f}_j = \frac{1}{(2\pi)^d} \int_{\mathbb{T}^d} \tilde{f}(\boldsymbol{x}) e^{-i\langle j,x\rangle}\, dx_1 \cdots dx_d. \tag{2.27}$$

Our assumption that $\tilde{f}(\boldsymbol{x})$ is real analytic is equivalent to the conditions that $\hat{f}_{-j} = \overline{\hat{f}_j}$ for $j \in \mathbb{Z}^d$ and there exist positive numbers M and σ such that $|\hat{f}_j| \leq Me^{-\sigma\|j\|}$, i.e. the Fourier modes $\hat{f}_j$ decay exponentially as $\|j\| \to \infty$. This is proved e.g. in Lemma 5.6 of [21].

For spatially quasi-periodic waves, we assume that η and φ are quasi-periodic functions of the same quasi-periods

$$\eta(x,t) = \tilde{\eta}(\boldsymbol{k}x,t), \qquad \varphi(x,t) = \tilde{\varphi}(\boldsymbol{k}x,t). \tag{2.28}$$

In correspondence, the velocity potential Φ is also quasi-periodic in x

$$\Phi(x,y,t) = \tilde{\Phi}(\boldsymbol{k}x,y,t), \tag{2.29}$$

where $\tilde{\Phi}(\boldsymbol{x},y,t)$ is periodic in $\boldsymbol{x}$. In the case where η and φ are quasi-periodic, the domain is unbounded and the functions do not decay to zero at infinity, which brings up both analytical and computational difficulties. To circumvent this issue, instead of working on the governing equations of η and φ directly, we study the equations of motion for $\tilde{\eta}$, $\tilde{\varphi}$, which are posed on a bounded domain $\mathbb{T}^d$; the motion of η, φ can be reconstructed from $\tilde{\eta}$, $\tilde{\varphi}$ using (2.28).

We define the fluid domain for tilde functions as

$$\Omega_{\tilde{\eta}} = \left\{(\boldsymbol{x},y) : -\infty < y < \tilde{\eta}(\boldsymbol{x},t), \quad \boldsymbol{x} \in \mathbb{T}^d\right\}. \tag{2.30}$$

The tilde velocity potential $\tilde{\Phi}$ satisfies the following Dirichlet-Neumann boundary value problem

$$\begin{cases} \left(\tilde{\partial}_x\right)^2 \tilde{\Phi} + \left(\partial_y\right)^2 \tilde{\Phi} = 0, & -\infty < y < \tilde{\eta}(\boldsymbol{x},t), \\ \partial_y \tilde{\Phi} = 0, & y \to -\infty, \\ \tilde{\Phi} = \tilde{\varphi}, & y = \tilde{\eta}(\boldsymbol{x},t), \end{cases} \tag{2.31}$$

where the quasi-periodic partial derivative operator is defined by

$$\tilde{\partial}_x := \boldsymbol{k} \cdot \nabla_{\boldsymbol{x}}, \qquad \nabla_{\boldsymbol{x}} = (\partial_{x_1}, \partial_{x_2}, \cdots, \partial_{x_d})^T. \tag{2.32}$$

Similar to (2.23), we are able to write the governing equations of tilde functions in terms of $\tilde{\eta}$ and $\tilde{\varphi}$; $\tilde{\Phi}$ can be reconstructed from $\tilde{\eta}$ and $\tilde{\varphi}$ by solving the boundary value problem (2.31). We define the quasi-periodic Dirichlet-Neumann operator

$$\tilde{G}(\tilde{\eta})(\tilde{\varphi}) = \partial_y \tilde{\Phi} - \left(\tilde{\partial}_x \tilde{\eta}\right)\left(\tilde{\partial}_x \tilde{\Phi}\right)\Big|_{y=\tilde{\eta}}. \tag{2.33}$$

Substituting (2.28) and (2.33) back into (2.23), we obtain the evolution equations of $\tilde{\eta}$ and $\tilde{\varphi}$ as follows

$$\begin{aligned} \tilde{\eta}_t &= \tilde{G}(\tilde{\eta})\tilde{\varphi}, \\ \tilde{\varphi}_t &= \frac{1}{2}\left(\frac{\left(\tilde{G}(\tilde{\eta})\tilde{\varphi} + \left(\tilde{\partial}_x \tilde{\eta}\right)\left(\tilde{\partial}_x \varphi\right)\right)^2}{1 + \left(\tilde{\partial}_x \tilde{\eta}\right)^2} - \left(\tilde{\partial}_x \tilde{\varphi}\right)^2\right) - g\tilde{\eta} + \tau\tilde{\kappa} + C(t), \end{aligned} \tag{2.34}$$

where the quasi-periodic mean curvature $\tilde{\kappa}$ is given by

$$\tilde{\kappa} = \tilde{\partial}_x \left(\frac{\tilde{\partial}_x \eta}{\sqrt{1 + (\tilde{\partial}_x \eta)^2}}\right). \tag{2.35}$$

2.1.3 The Hamiltonian System of Spatially Quasi-Periodic Waves

The governing equations given by (2.34) can be formulated as a Hamiltonian system [29,86] with energy

$$\tilde{E} = \int_{\mathbb{T}^d} \frac{1}{2}\tilde{\varphi}\tilde{G}(\tilde{\eta})\tilde{\varphi} + \frac{1}{2}g\tilde{\eta}^2 + \tau\left(\sqrt{1+\left(\tilde{\partial}_x\tilde{\eta}\right)^2} - 1\right) d\boldsymbol{x}. \tag{2.36}$$

The surface variables $\tilde{\eta}$ and $\tilde{\varphi}$ are canonical conjugate variables of the Hamiltonian system and the evolution equations (2.34) can be rewritten as

$$\tilde{\eta}_t = \frac{\delta\tilde{E}}{\delta\tilde{\varphi}}, \qquad \tilde{\varphi}_t = -\frac{\delta\tilde{E}}{\delta\tilde{\eta}}. \tag{2.37}$$

We define the mass and momentum by

$$\begin{aligned} \tilde{M} &= \int_{\mathbb{T}^d} \tilde{\eta}\, dy\, d\boldsymbol{x}, \\ \tilde{P} &= \int_{\mathbb{T}^d}\int_{-\infty}^{\tilde{\eta}} \tilde{\partial}_x\tilde{\Phi}\, dy d\boldsymbol{x} = -\int_{\mathbb{T}^d} \tilde{\Phi}|_{y=\tilde{\eta}}\tilde{\partial}_x\tilde{\eta}\, d\boldsymbol{x}. \end{aligned} \tag{2.38}$$

One can check that these two quantities are conserved in the time evolution. We remark that the definitions of $\tilde{H}$, $\tilde{M}$ and $\tilde{P}$ are similar to the ones in the periodic problem except that the definitions of the partial derivative with respect to x and the Dirichlet-Neumann operator [29] are different.

2.2 Governing Equations in Conformal Space

2.2.1 The Quasi-Periodic Hilbert Transform

We consider a bounded holomorphic function

$$z(w) = x(w) + iy(w), \qquad w = \alpha + i\beta, \tag{2.39}$$

that is defined on the lower half plane

$$\mathbb{C}^- = \{\alpha + i\beta \,:\, \alpha \in \mathbb{R},\, \beta < 0\}. \tag{2.40}$$

We assume that z can be extended continuously to $\overline{\mathbb{C}^-}$ and the imaginary part of z on the real line, denoted $v(\alpha)$, is a quasi-periodic function of the form (2.24)

$$v(\alpha) = \tilde{v}(\boldsymbol{k}\alpha), \qquad \tilde{v}(\boldsymbol{\alpha}) = \sum_{j\in\mathbb{Z}^d} \hat{v}_j e^{i\langle j,\boldsymbol{\alpha}\rangle}. \tag{2.41}$$

One can check that the function z takes the following form

$$z(w) = \hat{u}_{\mathbf{0}} + i\hat{v}_{\mathbf{0}} + \sum_{\langle j,k\rangle<0} 2i\hat{v}_j e^{i\langle j,k\rangle w}, \qquad w = \alpha + i\beta\,, \quad \beta \le 0, \tag{2.42}$$

where $\hat{u}_{\mathbf{0}}$ and $\hat{v}_{\mathbf{0}}$ are integration constants. We denote the value of the real part of z on the real line by $u(\alpha)$. According to (2.42), we know that u is determined by v up to an additive constant

$$u(\alpha) = \hat{u}_{\mathbf{0}} + \sum_{j\neq\mathbf{0}} (-i)\,\mathrm{sgn}(\langle \boldsymbol{j}, \boldsymbol{k}\rangle)\hat{v}_j e^{i\langle j,k\rangle\alpha}, \tag{2.43}$$

where $\mathrm{sgn}(q) \in \{1, 0, -1\}$ depending on whether $q > 0$, $q = 0$ or $q < 0$, respectively. We introduce a quasi-periodic Hilbert transform as follows.

Definition 2.2.1 *The Hilbert transform of a quasi-periodic $f(\alpha)$ of the form (2.24) is defined to be*

$$H[f](\alpha) = \sum_{j\in\mathbb{Z}^d} (-i)\,\mathrm{sgn}(\langle \boldsymbol{j},\ \boldsymbol{k}\rangle)\hat{f}_j e^{i\langle j,\,k\rangle\alpha}, \tag{2.44}$$

The symbol of the Hilbert transform is denoted by $\hat{H}_j = (-i)\,\mathrm{sgn}(\langle \boldsymbol{j},\ \boldsymbol{k}\rangle)$.

This agrees with the standard definition [38] of the Hilbert transform as a Cauchy principal value integral:

$$H[u](\alpha) = \frac{1}{\pi}\,\mathrm{PV}\int_{-\infty}^{\infty} \frac{u(\xi)}{\alpha - \xi}\,d\xi. \tag{2.45}$$

Indeed, it is easy to show that for functions of the form $u(\alpha) = e^{i\rho\alpha}$ with ρ real, the integral in (2.45) gives $H[u](\alpha) = -i\,\mathrm{sgn}(\rho)e^{i\rho\alpha}$. For extensions to the *upper* half-plane, the sum in (2.42) is over $\langle \boldsymbol{j}, \boldsymbol{k}\rangle > 0$, the last formula in (2.43) becomes $\hat{u}_j = i\,\mathrm{sgn}(\langle \boldsymbol{j}, \boldsymbol{k}\rangle)\hat{v}_j$.

Using the Hilbert transform, we can related u and v by

$$v = \hat{v}_{\mathbf{0}} - H[u], \qquad u = \hat{u}_{\mathbf{0}} + H[v], \tag{2.46}$$

where the constant $\hat{v}_{\mathbf{0}} = P_0[v]$ or $\hat{u}_{\mathbf{0}} = P_0[u]$ is a free parameter when computing v or u, respectively. H returns the "zero-mean" solution, i.e. $P_0 H[u] = 0$. Below is the definition of the projection operator P_0.

Definition 2.2.2 *Let $f(\alpha)$ be a quasi-periodic of the form (2.24). The projection operators P and P_0 are defined by*

$$P = \mathrm{id} - P_0, \qquad P_0[f] = \hat{f}_{\mathbf{0}} = \lim_{a\to\infty} \frac{1}{2a}\int_{-a}^{a} f(\alpha)\,d\alpha. \tag{2.47}$$

We can extend the definitions of the Hilbert transform and the projection operators of quasi-periodic functions to periodic functions in $L^2(\mathbb{T}^d)$ as follows

Definition 2.2.3 *For a periodic function $\tilde{f} \in L^2(\mathbb{T}^d)$, we define*

$$\begin{aligned} P = \mathrm{id} - P_0, \qquad P_0[\tilde{f}] = \hat{f}_{\mathbf{0}} = \frac{1}{(2\pi)^d} \int_{\mathbb{T}^d} \tilde{f}(\boldsymbol{\alpha})\, d\boldsymbol{\alpha}, \\ H[\tilde{f}](\boldsymbol{\alpha}) = \sum_{j \in \mathbb{Z}^d} (-i)\, \mathrm{sgn}(\langle \boldsymbol{j},\, \boldsymbol{k} \rangle) \hat{f}_j e^{i\langle j,\, \boldsymbol{\alpha} \rangle}. \end{aligned} \tag{2.48}$$

Let f be a quasi-periodic function of the form (2.24) and $\tilde{f}$ be the corresponding tilde function, the above two definitions of H, P and P_0 are consistent in the sense that

$$P[f](\alpha) = P[\tilde{f}](\boldsymbol{k}\alpha), \qquad P_0[f] = P_0[\tilde{f}], \qquad H[f](\alpha) = H[\tilde{f}](\boldsymbol{k}\alpha). \tag{2.49}$$

In the end of this section, we would like to introduce some properties of the Hilbert transform and the projection operator.

Lemma 2.2.4 *Suppose that f and g are two quasi-periodic functions of the form (2.24), then the following equalities are true*

(1) $P_0\left[f(Hg) + g(Hf)\right] = 0$;

(2) $P_0\left[fg - (Hf)(Hg)\right] = P_0[f]P_0[g]$;

(3) $H\left[fg - (Hf)(Hg)\right] = f(Hg) + g(Hf)$;

(4) $H\left[g(Hf) + f(Hg)\right] = P\left[(Hf)(Hg) - fg\right]$.

Proof: The equality (1) and (2) can be proved using the fact that $\hat{H}_j = -\hat{H}_{-j}$ and $\hat{H}_j \hat{H}_{-j} = 1$ for $\langle \boldsymbol{j}, \boldsymbol{k} \rangle \neq 0$. To show that the equality (3) is true, we consider the bounded holomorphic extensions of $Hf + if$ and $Hg + ig$ to the lower half plane, denoted z_f and z_g respectively. The value of the product $z_f z_g$ on the real line reads

$$z_f z_g|_{\beta=0} = (Hf + if)(Hg + ig) = \left[(Hf)(Hg) - fg\right] + i\left[g(Hf) + f(Hg)\right]. \tag{2.50}$$

Since $z_f z_g$ is still a bounded holomorphic function in the lower half plane, we can relate the real and imaginary part of $z_f z_g|_{\beta=0}$ by the Hilbert transform as follows

$$(Hf)(Hg) - fg = H\left[g(Hf) + f(Hg)\right] + C, \quad g(Hf) + f(Hg) = -H\left[(Hf)(Hg) - fg\right], \tag{2.51}$$

where C is an additive constant. We remark that there is no additive constant in the second equality as a result of equality (1). □

The preceding lemma is also true in the periodic case with $d = 1$ and $\boldsymbol{k} = (1)$. In the case where the fluid is of finite depth, equality (1) in the lemma still holds but (2) does not. This is because the symbol of the finite-depth Hilbert transform is $\hat{H}_j = -i \tanh\left(\langle \boldsymbol{j}, \boldsymbol{k} \rangle h\right)$ and $\hat{H}_j \hat{H}_{-j}$ is no longer 1 for $\langle \boldsymbol{j}, \boldsymbol{k} \rangle \neq 0$. Here h is the fluid depth in conformal space, which evolves in time to maintain constant fluid depth in physical space [56, 74].

Lemma 2.2.5 *Suppose that $\tilde{f}$, $\tilde{g} \in L^2(\mathbb{T}^d)$, the equalities (1) - (4) in Lemma 2.2.4 still hold.*

Proof: We are just going to prove the equality (3) as the rest are similar. It suffices to show that this equality holds for functions in

$$\Lambda := \{e_j = e^{i\langle j,\alpha\rangle}, j \in \mathbb{Z}^d\}. \tag{2.52}$$

For any $e_{j_1}, e_{j_2} \in \Lambda$, we have

$$H\left[e_{j_1}e_{j_2} - (He_{j_1})(He_{j_2})\right] = (-i)\,\mathrm{sgn}(\langle j_1 + j_2, k\rangle)(1 + \mathrm{sgn}(\langle j_1, k\rangle)\,\mathrm{sgn}(\langle j_2, k\rangle))e_{j_1+j_2}, \tag{2.53}$$

$$e_{j_1}(He_{j_2}) + e_{j_2}(He_{j_1}) = (-i)(\mathrm{sgn}(\langle j_1, k\rangle) + \mathrm{sgn}(\langle j_2, k\rangle))e_{j_1+j_2}. \tag{2.54}$$

If $j_1 + j_2 = \mathbf{0}$, the above two equalities are both equal to 0; otherwise, using the fact that $\mathrm{sgn}(\langle j_1 + j_2, k\rangle)^2 = 1$, we have

$$\begin{aligned} &H\left[e_{j_1}e_{j_2} - (He_{j_1})(He_{j_2})\right] - e_{j_1}(He_{j_2}) - e_{j_2}(He_{j_1}) \\ =&(-i)\,\mathrm{sgn}(\langle j_1 + j_2, k\rangle)(\mathrm{sgn}(\langle j_1 + j_2, k\rangle) - \mathrm{sgn}(\langle j_1, k\rangle))(\mathrm{sgn}(\langle j_1 + j_2, k\rangle) - \mathrm{sgn}(\langle j_2, k\rangle)) \\ =&0, \end{aligned} \tag{2.55}$$

which proves the equality (3). □

2.2.2 The Conformal Mapping

We consider a time dependent conformal mapping

$$z(w,t) = x(w,t) + iy(w,t), \qquad w = \alpha + i\beta. \tag{2.56}$$

that maps the lower half plane $\mathbb{C}^-$ to the fluid domain Ω_η and satisfies

$$z_w(w,t) \to 1, \qquad \beta \to -\infty. \tag{2.57}$$

We assume that $z(w,t)$ can be extended continuously to $\overline{\mathbb{C}^-}$ and maps the real line $\beta = 0$ to the free surface

$$\Gamma(t) = \{x + iy \,:\, y = \eta(x,t)\}. \tag{2.58}$$

We also introduce the notation $\zeta = z|_{\beta=0}$, $\xi = x|_{\beta=0}$ and $\eta = y|_{\beta=0}$ so that the free surface is parametrized by

$$\zeta(\alpha,t) = \xi(\alpha,t) + i\eta(\alpha,t), \qquad \alpha \in \mathbb{R}. \tag{2.59}$$

This allows us to denote a generic field point in the physical fluid by $z = x + iy$ while simultaneously discussing points $\zeta = \xi + i\eta$ on the free surface. To avoid ambiguity, we will henceforth denote the free surface elevation function in physical space from Section 2.1.1 by $\eta^{\mathrm{phys}}(x,t)$. Thus,

$$\eta(\alpha,t) = \eta^{\mathrm{phys}}(\xi(\alpha,t),t), \qquad \eta_\alpha = \eta^{\mathrm{phys}}_x \xi_\alpha, \qquad \eta_t = \eta^{\mathrm{phys}}_x \xi_t + \eta^{\mathrm{phys}}_t. \tag{2.60}$$

Our goal is to investigate the case where the free surface is quasi-periodic in α. This differs from conformal mappings discussed in [33,34,56,58,59,87], where the free surface is assumed to be periodic. If $\eta(\alpha, t)$ is a quasi-periodic function of the form (2.24)

$$\eta(\alpha, t) = \tilde{\eta}(\boldsymbol{k}\alpha, t), \qquad \tilde{\eta}(\boldsymbol{\alpha}, t) = \sum_{j \in \mathbb{Z}^d} \hat{\eta}_j(t) e^{i\langle j, \boldsymbol{\alpha}\rangle}, \qquad x \in \mathbb{R}, \quad \boldsymbol{\alpha}, \boldsymbol{k} \in \mathbb{R}^d, \tag{2.61}$$

according to Section 2.2.1 and (2.57), we know that ξ can be expressed by η up to an additive constant that possibly depends on time

$$\xi(\alpha, t) = \alpha + x_0(t) + H[\eta](\alpha, t). \tag{2.62}$$

Differentiating the above equation with respect to x gives

$$\xi_\alpha(\alpha, t) = 1 + H[\eta_\alpha](\alpha, t). \tag{2.63}$$

2.2.3 The Complex Velocity Potential

Let $\Phi^{\text{phys}}(x, y, t)$ denote the velocity potential in physical space from Section 2.1.1 and let $W^{\text{phys}}(x + iy, t) = \Phi^{\text{phys}}(x, y, t) + i\Psi^{\text{phys}}(x, y, t)$ be the complex velocity potential, where Ψ^{phys} is the stream function. Using the conformal mapping (2.56), we pull back these functions to the lower half plane and define

$$W(w, t) = \Phi(\alpha, \beta, t) + i\Psi(\alpha, \beta, t) = W^{\text{phys}}(z(w, t), t), \qquad w = \alpha + i\beta. \tag{2.64}$$

We also define $\varphi = \Phi|_{\beta=0}$ and $\psi = \Psi|_{\beta=0}$ and use (2.16) and (2.60) to obtain

$$\varphi(\alpha, t) = \varphi^{\text{phys}}(\xi(\alpha, t), t), \qquad \psi(\alpha, t) = \psi^{\text{phys}}(\xi(\alpha, t), t), \tag{2.65}$$

where $\psi^{\text{phys}}(x, t) = \Psi^{\text{phys}}(x, \eta^{\text{phys}}(x, t), t)$. We assume φ is quasi-periodic with the same quasi-periods as η

$$\varphi(\alpha, t) = \tilde{\varphi}(\boldsymbol{k}\alpha, t), \qquad \tilde{\varphi}(\boldsymbol{\alpha}, t) = \sum_{j \in \mathbb{Z}^d} \hat{\varphi}_j(t) e^{i\langle j, \boldsymbol{\alpha}\rangle}, \qquad x \in \mathbb{R}, \quad \boldsymbol{\alpha}, \boldsymbol{k} \in \mathbb{R}^d. \tag{2.66}$$

The fluid velocity $\nabla\Phi^{\text{phys}}(x, y, t)$ is assumed to decay to zero as $y \to -\infty$ (since we work in the lab frame). From Section 2.2.1 and the chain rule (see (2.68) below), $dW/dw \to 0$ as $\beta \to -\infty$. Thus, $\psi_\alpha = -H[\varphi_\alpha]$. Writing this as $\partial_\alpha[\psi + H\varphi] = 0$, we conclude that

$$\psi(\alpha, t) = \hat{\psi}_{\boldsymbol{0}} - H[\varphi](\alpha, t). \tag{2.67}$$

Considering that adding Φ and Ψ by constants (or functions of time only) will not affect the fluid motion, we set $\hat{\psi}_{\boldsymbol{0}} = P_0[\psi] = 0$ and $\hat{\varphi}_{\boldsymbol{0}} = P_0[\varphi] = 0$ in the scope of this thesis.

2.2.4 Governing Equations in Conformal Space

Following [26, 34, 56, 74, 78, 87], we present a derivation of the equations of motion for surface water waves in a conformal mapping formulation, modified as needed to handle quasi-periodic solutions.

From the chain rule, we have

$$\frac{dW}{dw} = \frac{dW^{\text{phys}}}{dz} \cdot \frac{dz}{dw} \qquad \Rightarrow \qquad \Phi_x^{\text{phys}} + i\Psi_x^{\text{phys}} = \frac{\Phi_\alpha + i\Psi_\alpha}{x_\alpha + iy_\alpha}. \tag{2.68}$$

Since $\Phi_y^{\text{phys}} = -\Psi_x^{\text{phys}}$, we can express the velocity of the fluid, which is the gradient of Φ^{phys} in terms of Φ_α and Ψ_α

$$\Phi_x^{\text{phys}} = \frac{\Phi_\alpha x_\alpha + \Psi_\alpha y_\alpha}{x_\alpha^2 + y_\alpha^2}, \qquad \Phi_y^{\text{phys}} = \frac{\Phi_\alpha y_\alpha - \Psi_\alpha x_\alpha}{x_\alpha^2 + y_\alpha^2}. \tag{2.69}$$

Evaluating (2.69) on the free surface gives

$$\Phi_x^{\text{phys}} = \frac{\varphi_\alpha \xi_\alpha + \psi_\alpha \eta_\alpha}{J}, \qquad \Phi_y^{\text{phys}} = \frac{\varphi_\alpha \eta_\alpha - \psi_\alpha \xi_\alpha}{J}, \qquad J = \xi_\alpha^2 + \eta_\alpha^2. \tag{2.70}$$

Using (2.60) and (2.70) in (2.17) and multiplying by ξ_α, we obtain

$$\eta_t \xi_\alpha - \xi_t \eta_\alpha = -\psi_\alpha. \tag{2.71}$$

This states that the normal velocity of the free surface is equal to the normal velocity of the fluid, $(\xi_t, \eta_t)^T \cdot \boldsymbol{n} = \nabla\Phi^{\text{phys}} \cdot \boldsymbol{n}$, where $\boldsymbol{n} = (-\eta_\alpha, \xi_\alpha)^T/\sqrt{J}$. This can also be obtained by tracking a fluid particle $x_p(t) + iy_p(t) = \zeta(\alpha_p(t), t)$ on the free surface. We have $\dot{x}_p = \xi_\alpha \dot{\alpha}_p + \xi_t = \Phi_x^{\text{phys}}$ and $\dot{y}_p = \eta_\alpha \dot{\alpha}_p + \eta_t = \Phi_y^{\text{phys}}$, which leads to (2.71) after eliminating $\dot{\alpha}_p$. This argument does not assume the free surface is a graph, i.e. (2.71) is also valid for overturning waves.

Next we consider z_t/z_w, which is a holomorphic function on $\mathbb{C}^-$ as long as z_w is bounded away from zero. The real and imaginary part of z_t/z_w at the top boundary $\beta = 0$ are

$$\text{Re}\left(\frac{z_t}{z_w}\right)\Big|_{\beta=0} = \frac{\xi_\alpha \xi_t + \eta_\alpha \eta_t}{J}, \qquad \text{Im}\left(\frac{z_t}{z_w}\right)\Big|_{\beta=0} = \frac{\xi_\alpha \eta_t - \eta_\alpha \xi_t}{J} = -\frac{\psi_\alpha}{J}, \tag{2.72}$$

where the last equality comes from (2.71). According to Section 2.2.1, $\text{Re}\,(z_t/z_w)|_{\beta=0}$ is determined by $\text{Im}\,(z_t/z_w)|_{\beta=0}$ up to a constant

$$\frac{\xi_t \xi_\alpha + \eta_t \eta_\alpha}{J} = -H\left[\frac{\psi_\alpha}{J}\right] + C_1, \tag{2.73}$$

where C_1 is an arbitrary integration constant that may depend on time but not space. Let $\boldsymbol{s} = (\xi_\alpha, \eta_\alpha)^T/\sqrt{J}$ denote the unit tangent vector to the curve. Equation (2.73) prescribes the tangential velocity $(\xi_t, \eta_t)^T \cdot \boldsymbol{s}$ of points on the curve in terms of the normal velocity in order to maintain a conformal parametrization. Note that the tangent velocity of the curve differs from that of the underlying fluid particles. This is similar in spirit to a method of Hou, Lowengrub and Shelley [47,48], who proposed a tangential velocity that maintains a uniform parametrization of the curve (rather than a conformal one); see also [7,26,74,83]. Combining (2.71) and (2.73), we obtain the kinematic boundary conditions in conformal space,

$$\begin{pmatrix}\xi_t\\ \eta_t\end{pmatrix} = \begin{pmatrix}\xi_\alpha & -\eta_\alpha\\ \eta_\alpha & \xi_\alpha\end{pmatrix}\begin{pmatrix}-H\left[\frac{\psi_\alpha}{J}\right] + C_1\\ -\frac{\psi_\alpha}{J}\end{pmatrix}. \tag{2.74}$$

Since ξ_t is related to η_t via the forward Hilbert transform (up to a constant). The constant is determined by comparing (2.62) with (2.74), which gives

$$\frac{dx_0}{dt} = P_0\left[\xi_\alpha\left(-H\left[\frac{\psi_\alpha}{J}\right] + C_1\right) + \frac{\eta_\alpha\psi_\alpha}{J}\right]. \tag{2.75}$$

The three most natural choices of C_1 are

$$\begin{aligned}
&(a)\ \ C_1 = 0: && \text{evolve } x_0(t) \text{ via (2.75)},\\
&(b)\ \ C_1 = P_0\big[\xi_\alpha H[\psi_\alpha/J] - \eta_\alpha\psi_\alpha/J\big]: && x_0(t) = 0,\\
&(c)\ \ C_1 = \big[H[\psi_\alpha/J] - \eta_\alpha\psi_\alpha/(\xi_\alpha J)\big]_{\alpha=0}: && \xi(0,t) = 0.
\end{aligned} \tag{2.76}$$

In options (b) and (c), the evolution equation ensures that $dx_0/dt = 0$ and $\xi_t(0,t) = 0$, respectively; we have assumed the initial conditions satisfy $x_0(0) = 0$ or $\xi(0,0) = 0$, respectively. Option (c) amounts to setting $x_0(t) = -H[\eta](0,t)$ in (2.62). This arguably leads to the most natural parametrization, but would have a problem if the vertical part of an overturning wave crosses $\alpha = 0$. Indeed, such a crossing would lead to $\xi_\alpha(0,t) = 0$ at some time t in the denominator of (2.76c). We recommend option (b) in this scenario. Using Remark 2.2.4, we can further simplify (2.76b) to $C_1 = 0$ and (2.75) to $dx_0/dt = C_1$, i.e. cases (a) and (b) in (2.76) coincide in the infinite depth case.

Next we evaluate the Bernoulli equation $\Phi^{\text{phys}}_t + \frac{1}{2}\left|\nabla\Phi^{\text{phys}}\right|^2 + \frac{P}{\rho} + gy = C_2$ at the free surface to obtain an evolution equation for $\varphi(\alpha,t)$. Here C_2 is an arbitrary integration constant that may depend on time but not space. The pressure at the free surface is determined by the Laplace-Young condition, $P = P_0 - \rho\tau\kappa$, where κ is the curvature, $\rho\tau$ is the surface tension, and P_0 is a constant that can be absorbed into C_2 and set to zero. From (2.68) or (2.70), we know $\left|\nabla\Phi^{\text{phys}}\right|^2 = (\varphi_\alpha^2 + \psi_\alpha^2)/J$ on the free surface. Finally, differentiating $\varphi(\alpha,t) = \Phi^{\text{phys}}(\xi(\alpha,t), \eta(\alpha,t), t)$ and using (2.70) and (2.74), we obtain

$$\varphi_t = \underbrace{\left(\Phi^{\text{phys}}_x, \Phi^{\text{phys}}_y\right)\begin{pmatrix}\xi_\alpha & -\eta_\alpha\\ \eta_\alpha & \xi_\alpha\end{pmatrix}}_{(\varphi_\alpha, -\psi_\alpha)}\begin{pmatrix}-H\left[\psi_\alpha/J\right] + C_1\\ -\psi_\alpha/J\end{pmatrix} - \frac{\varphi_\alpha^2 + \psi_\alpha^2}{2J} - g\eta + \tau\kappa + C_2, \tag{2.77}$$

where the mean curvature $\kappa = \left(\xi_\alpha \eta_{\alpha\alpha} - \eta_\alpha \xi_{\alpha\alpha}\right)/J^{3/2}$. We choose C_2 so that $P_0[\varphi_t] = 0$. In conclusion, we obtain the following governing equations for spatially quasi-periodic gravity-capillary waves in conformal space

$$\begin{gathered}
\xi_\alpha = 1 + H[\eta_\alpha], \qquad \psi = -H[\varphi], \qquad J = \xi_\alpha^2 + \eta_\alpha^2, \qquad \chi = \frac{\psi_\alpha}{J}, \\
\text{choose } C_1, \text{ e.g. as in (2.76)}, \qquad \text{compute } \frac{dx_0}{dt} \text{ in (2.75) if necessary}, \\
\eta_t = -\eta_\alpha H[\chi] - \xi_\alpha \chi + C_1 \eta_\alpha, \qquad \kappa = \frac{\xi_\alpha \eta_{\alpha\alpha} - \eta_\alpha \xi_{\alpha\alpha}}{J^{3/2}}, \\
\varphi_t = P\left[\frac{\psi_\alpha^2 - \varphi_\alpha^2}{2J} - \varphi_\alpha H[\chi] + C_1 \varphi_\alpha - g\eta + \tau\kappa\right].
\end{gathered} \tag{2.78}$$

Note that these equations govern the evolution of x_0, η and φ, which determine the state of the system. We emphasize that C_1 can be chosen arbitrarily as long as dx_0/dt satisfies (2.75). The special cases (2.76b) and (2.76c) lead to nice formulas for $x_0(t)$ without having to evolve (2.75) numerically. An alternative approach was proposed by Li *et al.* [56], who set $C_1 = 0$ (by not introducing it) and avoid writing down a differential equation for $x_0(t)$ by instead solving both the ξ_t and η_t equations in (2.74). The governing equations break down if J becomes zero somewhere on the curve. Such a singularity would arise, for example, if the wave profile were to form a corner in finite time. To our knowledge, it remains an open question whether the free-surface Euler equations can form such a corner.

In practice, instead of solving (2.78) directly, we compute the time evolution of $\tilde{\eta}$ and $\tilde{\varphi}$ on $\mathbb{T}^d$ and reconstruct η, φ from $\tilde{\eta}$, $\tilde{\varphi}$ using (2.61) and (2.66), respectively. The evolution equations of $\tilde{\eta}$ and $\tilde{\varphi}$ can be derived from (2.78) by replacing ∂_α with $\tilde{\partial}_\alpha := \boldsymbol{k} \cdot \nabla_{\boldsymbol{\alpha}}$

$$\begin{gathered}
\tilde{\eta}_t = -\left(\tilde{\partial}_\alpha \tilde{\eta}\right) H[\tilde{\chi}] - \left(1 + \tilde{\partial}_\alpha \tilde{\xi}\right) \tilde{\chi} + C_1 \left(\tilde{\partial}_\alpha \tilde{\eta}\right), \\
\tilde{\varphi}_t = P\left[\frac{\left(\tilde{\partial}_\alpha \tilde{\psi}\right)^2 - \left(\tilde{\partial}_\alpha \tilde{\varphi}\right)^2}{2\tilde{J}} - \left(\tilde{\partial}_\alpha \tilde{\varphi}\right) H[\tilde{\chi}] + C_1 \tilde{\partial}_\alpha \tilde{\varphi} - g\tilde{\eta} + \tau\tilde{\kappa}\right], \\
\tilde{\partial}_\alpha \tilde{\xi} = H\left[\tilde{\partial}_\alpha \tilde{\eta}\right], \qquad \tilde{J} = \left(1 + \tilde{\partial}_\alpha \tilde{\xi}\right)^2 + \left(\tilde{\partial}_\alpha \tilde{\eta}\right)^2, \qquad \tilde{\psi} = -H[\tilde{\varphi}], \\
\tilde{\chi} = \frac{\tilde{\partial}_\alpha \tilde{\psi}}{\tilde{J}}, \qquad \tilde{\kappa} = \frac{(1 + \tilde{\partial}_\alpha \tilde{\xi})\tilde{\partial}_\alpha^2 \tilde{\eta} - (\tilde{\partial}_\alpha \tilde{\eta})\tilde{\partial}_\alpha^2 \tilde{\xi}}{\tilde{J}^{3/2}},
\end{gathered} \tag{2.79}$$

For waves that are graphs, we usually choose C_1 such that $\tilde{\xi}(\mathbf{0}, t) = 0$

$$C_1 = \left[H[\tilde{\partial}_\alpha \tilde{\psi}/\tilde{J}] - \tilde{\partial}_\alpha \tilde{\eta} \tilde{\partial}_\alpha \tilde{\psi}/((1 + \tilde{\partial}_\alpha \tilde{\xi})\tilde{J})\right]_{\boldsymbol{\alpha}=\mathbf{0}}. \tag{2.80}$$

For waves that are not graphs, such as overturning waves, we choose $C_1 = 0$. The function $\tilde{\xi}(\boldsymbol{\alpha}, t)$ in (2.79) is related to $\tilde{\eta}(\boldsymbol{\alpha}, t)$ by

$$\tilde{\xi}(\boldsymbol{\alpha}, t) = x_0(t) + H[\tilde{\eta}](\boldsymbol{\alpha}, t), \tag{2.81}$$

where one can compute $x_0(t)$ using (2.75) with a replacement of ∂_α by $\tilde{\partial}_\alpha$. The function ξ can be reconstructed from $\tilde{\xi}$ through

$$\xi(\alpha, t) = \alpha + \tilde{\xi}(\boldsymbol{k}\alpha, t). \tag{2.82}$$

2.2.5 The Non-Canonical Hamiltonian Structure

Following the derivations in [35,87], we use a change of coordinates

$$\boldsymbol{x} = \boldsymbol{\alpha} + \boldsymbol{k}\tilde{\xi}(\boldsymbol{\alpha}, t). \tag{2.83}$$

to obtain the the formulas for $\tilde{E}$, $\tilde{M}$ and $\tilde{P}$ in conformal variables from their expressions (2.36, 2.38) in physical space

$$\begin{aligned} \tilde{E} &= \int_{\mathbb{T}^d} \left[\frac{1}{2}\tilde{\psi}\tilde{\partial}_\alpha\tilde{\varphi} + \frac{1}{2}g\tilde{\eta}^2(\tilde{\partial}_\alpha\tilde{\xi}) + \tau\left(\sqrt{(1+\tilde{\partial}_\alpha\tilde{\xi})^2 + (\tilde{\partial}_\alpha\tilde{\eta})^2} - 1\right)\right] d\boldsymbol{\alpha}, \\ \tilde{M} &= \int_{\mathbb{T}^d} \tilde{\eta}(1+\tilde{\partial}_\alpha\tilde{\xi})\, d\boldsymbol{\alpha}, \qquad \tilde{P} = \int_{\mathbb{T}^d} -\tilde{\varphi}\tilde{\partial}_\alpha\tilde{\eta}\, d\boldsymbol{\alpha}. \end{aligned} \tag{2.84}$$

Since we are able to compute overturning waves using the conformal mapping formulation, which is beyond the reach of the graph-based formulation in physical space, it is necessary to show that the above three quantities are conserved using the evolution equations (2.79) in conformal space for the self-consistency of the theory. Computing the time derivative of $\tilde{M}$, we have

$$\frac{d\tilde{M}}{dt} = \int_{\mathbb{T}^d} \tilde{\eta}_t(1+\tilde{\partial}_\alpha\tilde{\xi}) - \tilde{\xi}_t(\tilde{\partial}_\alpha\tilde{\eta})\, d\boldsymbol{\alpha} = -\int_{\mathbb{T}^d} \tilde{\partial}_\alpha\tilde{\psi}\, d\boldsymbol{\alpha} = 0, \tag{2.85}$$

where we use the torus version of the kinematic boundary condition (2.71) in the second equality. The time derivative of $\tilde{P}$ is give by

$$\begin{aligned} \frac{d\tilde{P}}{dt} &= \int_{\mathbb{T}^d} -\tilde{\varphi}_t(\tilde{\partial}_\alpha\tilde{\eta}) + \tilde{\eta}_t(\tilde{\partial}_\alpha\tilde{\varphi})\, d\boldsymbol{\alpha} \\ &= \int_{\mathbb{T}^d} \underbrace{-(\tilde{\partial}_\alpha\tilde{\varphi})(1+\tilde{\partial}_\alpha\tilde{\xi})\frac{\tilde{\partial}_\alpha\tilde{\psi}}{\tilde{J}} - (\tilde{\partial}_\alpha\tilde{\eta})\frac{(\tilde{\partial}_\alpha\tilde{\psi})^2}{2\tilde{J}} + (\tilde{\partial}_\alpha\tilde{\eta})\frac{(\tilde{\partial}_\alpha\tilde{\phi})^2}{2\tilde{J}}}_{I_2} \\ &\quad + g\tilde{\eta}(\tilde{\partial}_\alpha\tilde{\eta}) - \tau\tilde{\kappa}(\tilde{\partial}_\alpha\tilde{\eta})\, d\boldsymbol{\alpha}. \end{aligned} \tag{2.86}$$

In the second equality, we plug in the evolution equations of $\tilde{\eta}$ and $\tilde{\varphi}$. The integral of the last two terms in (2.86) is zero because

$$\begin{aligned} \int_{\mathbb{T}^d} g\tilde{\eta}(\tilde{\partial}_\alpha\tilde{\eta})\, d\boldsymbol{\alpha} &= \int_{\mathbb{T}^d} \frac{1}{2}g\tilde{\partial}_\alpha\tilde{\eta}^2\, d\boldsymbol{\alpha} = 0. \\ \int_{\mathbb{T}^d} \tau\tilde{\kappa}\tilde{\partial}_\alpha\tilde{\eta}\, d\boldsymbol{\alpha} &= -\int_{\mathbb{T}^d} \tau\tilde{\partial}_\alpha\left(\frac{1+\tilde{\partial}_\alpha\tilde{\xi}}{\tilde{J}^{1/2}}\right) d\boldsymbol{\alpha} = 0. \end{aligned} \tag{2.87}$$

To show that $\tilde{P}$ is a conserved quantity, we just need to verify that the integral of I_2 vanishes. We rearrange the terms in I_2 to obtain

$$\begin{aligned}\int_{\mathbb{T}^d} I_2\, d\boldsymbol{\alpha} = -\frac{1}{2}\int_{\mathbb{T}^d} (\tilde{\partial}_\alpha\tilde{\varphi})\underbrace{\left(\frac{(1+\tilde{\partial}_\alpha\tilde{\xi})(\tilde{\partial}_\alpha\tilde{\psi}) - (\tilde{\partial}_\alpha\tilde{\eta})(\tilde{\partial}_\alpha\tilde{\varphi})}{\tilde{J}}\right)}_{B} \\ + (\tilde{\partial}_\alpha\tilde{\psi})\left(\frac{(1+\tilde{\partial}_\alpha\tilde{\xi})(\tilde{\partial}_\alpha\tilde{\varphi}) + (\tilde{\partial}_\alpha\tilde{\eta})(\tilde{\partial}_\alpha\tilde{\psi})}{\tilde{J}}\right) d\boldsymbol{\alpha},\end{aligned} \tag{2.88}$$

Computing the value of the following holomorphic function on the real line

$$\left.\frac{W_w}{z_w}\right|_{\beta=0} = \left.\frac{\Phi_\alpha + i\Psi_\alpha}{x_\alpha + iy_\alpha}\right|_{\beta=0} = \frac{\xi_\alpha\varphi_\alpha + \eta_\alpha\psi_\alpha}{J} + i\frac{-\eta_\alpha\varphi_\alpha + \xi_\alpha\psi_\alpha}{J}, \tag{2.89}$$

we have

$$\frac{\xi_\alpha\varphi_\alpha + \eta_\alpha\psi_\alpha}{J} = H\left[\frac{-\eta_\alpha\varphi_\alpha + \xi_\alpha\psi_\alpha}{J}\right] + C. \tag{2.90}$$

Therefore the corresponding tilde functions in (2.88) can also be related by the Hilbert transform, which yields

$$\int_{\mathbb{T}^d} I_2\, d\boldsymbol{\alpha} = -\frac{1}{2}\int_{\mathbb{T}^d} \tilde{\partial}_\alpha\varphi B + \tilde{\partial}_\alpha\tilde{\psi}H[B]\, d\boldsymbol{\alpha} = 0, \tag{2.91}$$

where we use Lemma 2.2.5 in the last equality. Hence we conclude that $\tilde{P}$ is conserved in the motion.

To demonstrate that $\tilde{E}$ is a constant of motion, we are going to exhibit that (2.79) can be written as a non-canonical Hamiltonian system and $\tilde{E}$ is the corresponding Hamiltonian, thus a conserved quantity for the system. According to (2.79), we can express $\tilde{\psi}$ and $\tilde{\partial}_\alpha\tilde{\xi}$ in terms of $\tilde{\varphi}$ and $\tilde{\partial}_\alpha\tilde{\eta}$ as follows

$$\tilde{\psi} = -H[\tilde{\varphi}], \qquad \tilde{\partial}_\alpha\tilde{\xi} = H[\tilde{\partial}_\alpha\tilde{\eta}], \tag{2.92}$$

hence we can rewrite $\tilde{E}$ as a functional of only $\tilde{\eta}$ and $\tilde{\varphi}$ as follows

$$\tilde{E} = \int_{\mathbb{T}^d}\left[-\frac{1}{2}H[\tilde{\varphi}]\tilde{\partial}_\alpha\tilde{\varphi} + \frac{1}{2}g\tilde{\eta}^2H[\tilde{\partial}_\alpha\tilde{\eta}] + \tau\left(\sqrt{\left(1+H[\tilde{\partial}_\alpha\tilde{\eta}]\right)^2 + \left(\tilde{\partial}_\alpha\tilde{\eta}\right)^2} - 1\right)\right] d\boldsymbol{\alpha}. \tag{2.93}$$

In [35], Dyachenko, Lushnikov and Zakharov proposed that the equations of motion for gravity-capillary waves in conformal variables can be formulated as a non-canonical Hamiltonian system with η and ξ being the conjugate variables. We next show that their results can be extended to the problem of spatially quasi-periodic waves.

In physical space, the Hamiltonian equations (2.37) can be obtained by minimizing the following action functional

$$\tilde{S} = \int \tilde{L}\, dt, \tag{2.94}$$

where the Lagrangian $\tilde{L}$ is given by

$$\tilde{L} = \int_{\mathbb{T}^d} \tilde{\varphi}^{\text{phys}} \tilde{\eta}_t^{\text{phys}}\, d\boldsymbol{x} - \tilde{E}. \tag{2.95}$$

Using the coordinate transform (2.83), we can express $\tilde{L}$ in terms of conformal variables

$$\tilde{L} = \int_{\mathbb{T}^d} \tilde{\varphi} \left(\tilde{\eta}_t (1 + \tilde{\partial}_\alpha \tilde{\xi}) - \tilde{\xi}_t \tilde{\partial}_\alpha \tilde{\eta} \right) d\boldsymbol{\alpha} - \tilde{E}, \tag{2.96}$$

As shown in (2.82), $\tilde{\xi}$ is determined by $\tilde{\eta}$ up to an additive constant x_0, which is introduced by the conformal mapping. To fix the mapping, we set $x_0 = 0$, which also leads to $C_1 = 0$ in (2.73). We introduce a Lagrangian multiplier $\tilde{f}$ to impose the relation between $\tilde{\xi}$ and $\tilde{\eta}$, and modify the definition of $\tilde{L}$, $\tilde{S}$ accordingly

$$\tilde{L}^{\text{conf}} = \tilde{L} + \int_{\mathbb{T}^d} \tilde{f}(\tilde{\xi} - H[\tilde{\eta}])\, d\boldsymbol{\alpha} - \tilde{E}, \qquad \tilde{S}^{\text{conf}} = \int \tilde{L}^{\text{conf}}\, dt. \tag{2.97}$$

The vanishing of the variation $\delta \tilde{S}^{\text{conf}} = 0$ with respect to $\tilde{\varphi}$ yields

$$\tilde{\eta}_t (1 + \tilde{\partial}_\alpha \tilde{\xi}) - \tilde{\xi}_t \tilde{\partial}_\alpha \tilde{\eta} = \frac{\delta \tilde{E}}{\delta \tilde{\varphi}} = H[\tilde{\partial}_\alpha \tilde{\varphi}], \tag{2.98}$$

which is the dynamic boundary condition (2.71). We use $\delta \tilde{S} = 0$ with respect to $\tilde{\xi}$ and $\tilde{\eta}$ to obtain

$$\begin{aligned} &(a) \qquad -\tilde{\eta}_t \tilde{\partial}_\alpha \tilde{\varphi} + \tilde{\varphi}_t \tilde{\partial}_\alpha \tilde{\eta} = -\tilde{f}, \\ &(b) \qquad \tilde{\xi}_t \tilde{\partial}_\alpha \tilde{\varphi} - \tilde{\varphi}_t (1 + \tilde{\partial}_\alpha \tilde{\xi}) - \frac{\delta \tilde{E}}{\delta \tilde{\eta}} = -H[\tilde{f}]. \end{aligned} \tag{2.99}$$

One can notice that the left hand side of (a) and (b) can be related by the Hilbert transform

$$\tilde{\xi}_t \tilde{\partial}_\alpha \tilde{\varphi} - \tilde{\varphi}_t (1 + \tilde{\partial}_\alpha \tilde{\xi}) - \frac{\delta \tilde{E}}{\delta \tilde{\eta}} = H\left[-\tilde{\eta}_t \tilde{\partial}_\alpha \tilde{\varphi} + \tilde{\varphi}_t \tilde{\partial}_\alpha \tilde{\eta} \right]. \tag{2.100}$$

Substituting $\tilde{\xi}_t = H[\tilde{\eta}_t]$ into (2.98) and (2.100), we obtain

$$\begin{pmatrix} \tilde{\Omega}_{11} & \tilde{\Omega}_{12} \\ \tilde{\Omega}_{21} & 0 \end{pmatrix} \begin{pmatrix} \tilde{\eta}_t \\ \tilde{\varphi}_t \end{pmatrix} = \begin{pmatrix} \frac{\delta \tilde{E}}{\delta \tilde{\eta}} \\ \frac{\delta \tilde{E}}{\delta \tilde{\varphi}} \end{pmatrix}. \tag{2.101}$$

We denote the matrix on the left hand side of the equation by $\tilde{\Omega}$; for a function $\tilde{p}$ in $L^2(\mathbb{T}^d)$, the entries of Ω are given by

$$\begin{aligned}
\tilde{\Omega}_{11}\tilde{p} &= H[\tilde{p}\tilde{\partial}_\alpha\tilde{\varphi}] + \tilde{\partial}_\alpha\tilde{\varphi}H[\tilde{p}],\\
\tilde{\Omega}_{12}\tilde{p} &= -H[\tilde{p}\tilde{\partial}_\alpha\tilde{\eta}] - (1+\tilde{\partial}_\alpha\tilde{\xi})\tilde{p} = -H[\tilde{p}\tilde{\partial}_\alpha\tilde{\eta}] - (1+H[\tilde{\partial}_\alpha\tilde{\eta}])\tilde{p},\\
\tilde{\Omega}_{21}\tilde{p} &= (1+\tilde{\partial}_\alpha\tilde{\xi})\tilde{p} - \tilde{\partial}_\alpha\tilde{\eta}H[\tilde{p}] = (1+H[\tilde{\partial}_\alpha\tilde{\eta}])\tilde{p} - \tilde{\partial}_\alpha\tilde{\eta}H[\tilde{p}].
\end{aligned} \tag{2.102}$$

For any $\tilde{p}, \tilde{q} \in L^2(\mathbb{T}^d)$, one can use Lemma 2.2.5 to obtain

$$\begin{aligned}
\int_{\mathbb{T}^d} \left(\tilde{\Omega}_{11}\tilde{p}\right)\tilde{q}\, d\boldsymbol{\alpha} &= \int_{\mathbb{T}^d} H[\tilde{p}\tilde{\partial}_\alpha\tilde{\varphi}]\tilde{q} + \tilde{\partial}_\alpha\tilde{\varphi}H[\tilde{p}]\tilde{q}\, d\boldsymbol{\alpha}\\
&= \int_{\mathbb{T}^d} -\tilde{p}\tilde{\partial}_\alpha\tilde{\varphi}H[\tilde{q}] - \tilde{p}H[\tilde{q}\tilde{\partial}_\alpha\tilde{\varphi}]\, d\boldsymbol{\alpha}\\
&= -\int_{\mathbb{T}^d} \tilde{p}\tilde{\Omega}_{11}\tilde{q}\, d\boldsymbol{\alpha}.
\end{aligned} \tag{2.103}$$

$$\begin{aligned}
\int_{\mathbb{T}^d} \left(\tilde{\Omega}_{12}\tilde{p}\right)\tilde{q}\, d\boldsymbol{\alpha} &= \int_{\mathbb{T}^d} -H[\tilde{p}\tilde{\partial}_\alpha\tilde{\eta}]\tilde{q} - (1+H[\tilde{\partial}_\alpha\tilde{\eta}])\tilde{p}\tilde{q}\, d\boldsymbol{\alpha}\\
&= \int_{\mathbb{T}^d} \tilde{p}\tilde{\partial}_\alpha\tilde{\eta}H[\tilde{q}] - (1+H[\tilde{\partial}_\alpha\tilde{\eta}])\tilde{p}\tilde{q}\, d\boldsymbol{\alpha}\\
&= -\int_{\mathbb{T}^d} \tilde{p}\tilde{\Omega}_{21}\tilde{q}\, d\boldsymbol{\alpha}.
\end{aligned} \tag{2.104}$$

Therefore $\tilde{\Omega}$ is skew-symmetric with respect to the L^2 inner product. We can find the inverse of $\tilde{\Omega}$ explicitly and write the evolution equations of $\tilde{\eta}$ and $\tilde{\varphi}$ into the form of a non-canonical Hamiltonian system. To do so, we first cancel the term $\tilde{\varphi}_t$ in (2.99) by computing $(a)\cdot(1+\tilde{\partial}_\alpha\tilde{\xi}) + (b)\cdot\tilde{\partial}_\alpha\tilde{\eta}$

$$\tilde{\partial}_\alpha\tilde{\varphi}\left(\tilde{\eta}_t(1+\tilde{\partial}_\alpha\tilde{\xi}) - \tilde{\xi}_t\tilde{\partial}_\alpha\tilde{\eta}\right) + \tilde{\partial}_\alpha\tilde{\eta}\frac{\delta\tilde{E}}{\delta\tilde{\eta}} = \tilde{\partial}_\alpha\tilde{\eta}H[\tilde{f}] + (1+\tilde{\partial}_\alpha\tilde{\xi})\tilde{f}. \tag{2.105}$$

Substituting (2.98) into the above equation, we obtain

$$\tilde{\partial}_\alpha\tilde{\varphi}\frac{\delta\tilde{E}}{\delta\tilde{\varphi}} + \tilde{\partial}_\alpha\tilde{\eta}\frac{\delta\tilde{E}}{\delta\tilde{\eta}} = \tilde{\partial}_\alpha\tilde{\eta}H[\tilde{f}] + (1+\tilde{\partial}_\alpha\tilde{\xi})\tilde{f}. \tag{2.106}$$

Next we compute $(a)\cdot\tilde{\partial}_\alpha\tilde{\eta} - (b)\cdot(1+\tilde{\partial}_\alpha\tilde{\xi})$ and replace $(\tilde{\partial}_\alpha\tilde{\eta})^2 + (1+\tilde{\partial}_\alpha\tilde{\xi})^2$ by $\tilde{J}$

$$\tilde{J}\tilde{\varphi}_t - \left(\tilde{\eta}_t\tilde{\partial}_\alpha\eta + \tilde{\xi}_t(1+\tilde{\partial}_\alpha\tilde{\xi})\right)\tilde{\partial}_\alpha\tilde{\varphi} + (1+\tilde{\partial}_\alpha\tilde{\xi})\frac{\delta\tilde{E}}{\delta\tilde{\eta}} = -\tilde{f}\tilde{\partial}_\alpha\tilde{\eta} + (1+\tilde{\partial}_\alpha\tilde{\xi})H[\tilde{f}]. \tag{2.107}$$

According to Lemma 2.2.5, we know that the right hand side of (2.106) and (2.107) can be related by the Hilbert transform, therefore we have

$$\tilde{J}\tilde{\varphi}_t - \left(\tilde{\eta}_t\tilde{\partial}_\alpha\eta + \tilde{\xi}_t(1+\tilde{\partial}_\alpha\tilde{\xi})\right)\tilde{\partial}_\alpha\tilde{\varphi} + (1+\tilde{\partial}_\alpha\tilde{\xi})\frac{\delta\tilde{E}}{\delta\tilde{\eta}} = H\left[\tilde{\partial}_\alpha\tilde{\varphi}\frac{\delta\tilde{E}}{\delta\tilde{\varphi}} + \tilde{\partial}_\alpha\tilde{\eta}\frac{\delta\tilde{E}}{\delta\tilde{\eta}}\right]. \tag{2.108}$$

The substitution of (2.73) into the above equation gives

$$\tilde{\varphi}_t = \tilde{\partial}_\alpha \tilde{\varphi} H\left[\frac{1}{\tilde{J}}\tilde{\partial}_\alpha \tilde{\psi}\right] - \frac{1}{\tilde{J}}(1+\tilde{\partial}_\alpha \tilde{\xi})\frac{\delta \tilde{E}}{\delta \tilde{\eta}} + \frac{1}{\tilde{J}} H\left[\tilde{\partial}_\alpha \tilde{\varphi}\frac{\delta \tilde{E}}{\delta \tilde{\varphi}} + \tilde{\partial}_\alpha \tilde{\eta}\frac{\delta \tilde{E}}{\delta \tilde{\eta}}\right]. \tag{2.109}$$

We replace $\tilde{\partial}_\alpha \tilde{\psi}$ by $\frac{\delta \tilde{E}}{\delta \tilde{\varphi}}$ using (2.98) in the above equation and rewrite the equation as

$$\tilde{\varphi}_t = \tilde{\partial}_\alpha \tilde{\varphi} H\left[\frac{1}{\tilde{J}}\frac{\delta \tilde{E}}{\delta \tilde{\varphi}}\right] - \frac{1}{\tilde{J}}(1+\tilde{\partial}_\alpha \tilde{\xi})\frac{\delta \tilde{E}}{\delta \tilde{\eta}} + \frac{1}{\tilde{J}} H\left[\tilde{\partial}_\alpha \tilde{\varphi}\frac{\delta \tilde{E}}{\delta \tilde{\varphi}} + \tilde{\partial}_\alpha \tilde{\eta}\frac{\delta \tilde{E}}{\delta \tilde{\eta}}\right]. \tag{2.110}$$

In summary, we can rewrite the evolution equation of $\tilde{\eta}$ and $\tilde{\varphi}$, given in (2.79) and (2.110) by

$$\begin{pmatrix} \tilde{\eta}_t \\ \tilde{\varphi}_t \end{pmatrix} = \begin{pmatrix} 0 & \tilde{R}_{12} \\ \tilde{R}_{21} & \tilde{R}_{22} \end{pmatrix} \begin{pmatrix} \frac{\delta \tilde{E}}{\delta \tilde{\eta}} \\ \frac{\delta \tilde{E}}{\delta \tilde{\varphi}} \end{pmatrix}, \tag{2.111}$$

which is a non-canonical Hamiltonian system. We denote the matrix on the right hand side by $\tilde{R}$; for $\tilde{p} \in L^2(\mathbb{T}^d)$, the entries of $\tilde{R}$ are given by

$$\begin{aligned} \tilde{R}_{12}\tilde{p} &= \frac{1+\tilde{\partial}_\alpha \tilde{\xi}}{\tilde{J}}\tilde{p} + \tilde{\partial}_\alpha \tilde{\eta} H\left[\frac{\tilde{p}}{\tilde{J}}\right], \\ \tilde{R}_{21}\tilde{p} &= -\frac{1+\tilde{\partial}_\alpha \tilde{\xi}}{\tilde{J}}\tilde{p} + \frac{1}{\tilde{J}} H[\tilde{p}\tilde{\partial}_\alpha \tilde{\eta}], \\ \tilde{R}_{22}\tilde{p} &= \tilde{\partial}_\alpha \tilde{\varphi} H\left[\frac{\tilde{p}}{\tilde{J}}\right] + \frac{1}{\tilde{J}} H[\tilde{p}\tilde{\partial}_\alpha \tilde{\varphi}]. \end{aligned} \tag{2.112}$$

Similar to (2.103) and (2.104), one can verify that $\tilde{R}$ is a skew-symmetric matrix: for $\tilde{p}, \tilde{q} \in L^2(\mathbb{T}^d)$, we have

$$\langle \tilde{R}_{12}\tilde{p}, \tilde{q}\rangle = -\langle \tilde{p}, \tilde{R}_{21}\tilde{q}\rangle, \qquad \langle \tilde{R}_{22}\tilde{p}, \tilde{q}\rangle = -\langle \tilde{p}, \tilde{R}_{22}\tilde{q}\rangle, \tag{2.113}$$

where $\langle \cdot, \cdot \rangle$ denotes the usual L^2 inner product on $\mathbb{T}^d$. We compare (2.111) and (2.112) to conclude that

$$\tilde{\Omega}\tilde{R} = \tilde{R}\tilde{\Omega} = I, \tag{2.114}$$

which can also be verified through direct computation.

We define the following Poisson bracket for functionals $\tilde{F}, \tilde{G}$ of $\tilde{\eta}, \tilde{\varphi}$ using (2.112)

$$\{\tilde{F}, \tilde{G}\} = \int_{\mathbb{T}^d} \frac{\delta \tilde{F}}{\delta \tilde{\eta}}\tilde{R}_{12}\frac{\delta \tilde{G}}{\delta \tilde{\varphi}} + \frac{\delta \tilde{F}}{\delta \tilde{\varphi}}\tilde{R}_{21}\frac{\delta \tilde{G}}{\delta \tilde{\eta}} + \frac{\delta \tilde{F}}{\delta \tilde{\varphi}}\tilde{R}_{22}\frac{\delta \tilde{G}}{\delta \tilde{\varphi}}\, d\boldsymbol{\alpha}. \tag{2.115}$$

One can check that the Poisson bracket satisfies the Jacobi identity

$$\{\tilde{F}, \{\tilde{G}, \tilde{L}\}\} + \{\tilde{G}, \{\tilde{L}, \tilde{F}\}\} + \{\tilde{L}, \{\tilde{F}, \tilde{G}\}\} = 0, \tag{2.116}$$

where $\tilde{F}$, $\tilde{G}$ and $\tilde{L}$ are functionals of $\tilde{\eta}$ and $\tilde{\varphi}$.

Using the Poisson bracket, the time evolution of a functional $\tilde{F}$ of $\tilde{\eta}$ and $\tilde{\varphi}$ can be written as

$$\tilde{F}_t = \{\tilde{F}, \tilde{E}\}. \tag{2.117}$$

Therefore $\tilde{F}$ is a constant of motion if $\{\tilde{F}, \tilde{E}\} = 0$. As a result of the skew-symmetry of $\tilde{R}$, we know that $\tilde{E}_t = \{\tilde{E}, \tilde{E}\} = 0$, hence $\tilde{E}$ is conserved in the motion.

Chapter 3

Quasi-Periodic Traveling Waves

3.1 Governing Equations of Quasi-Periodic Traveling Waves in Conformal Space

We specialize to the case of quasi-periodic traveling waves and derive the equations of motion in a conformal mapping framework. One approach (see e.g. [59] for the periodic case) is to write down the equations of motion in a graph-based representation of the surface variables $\eta^{\text{phys}}(x,t)$ and $\varphi^{\text{phys}}(x,t) = \Phi^{\text{phys}}(x,\eta(x,t),t)$ and substitute $\eta_t^{\text{phys}} = -c\eta_x^{\text{phys}}$, $\varphi_t^{\text{phys}} = -c\varphi_x^{\text{phys}}$ to solve for the initial condition of a solution of the form

$$\eta^{\text{phys}}(x,t) = \eta_0^{\text{phys}}(x-ct), \qquad \varphi^{\text{phys}}(x,t) = \varphi_0^{\text{phys}}(x-ct). \tag{3.1}$$

We present below an alternative derivation of the equations in [59] that is more direct and does not assume the wave profile is single-valued. Other systems of equations have also been derived to describe traveling water waves, e.g. by Nekrasov [61,63] and Dyachenko *et. al.* [38].

Recall the kinematic condition (2.71) that the normal velocity of the curve is given by $\zeta_t \cdot \boldsymbol{n} = -\psi_\alpha/\sqrt{J}$, where $J = \xi_\alpha^2 + \eta_\alpha^2$. Since the wave travels at constant speed c in physical space, there is a reparametrization $\beta(\alpha,t)$ such that $\zeta(\alpha,t) = \zeta(\beta(\alpha,t),0) + ct$. Since ζ_α is tangent to the curve, the normal velocity is simply $\zeta_t \cdot \boldsymbol{n} = (c,0)^T \cdot \boldsymbol{n} = -c\eta_\alpha/\sqrt{J}$, where we used $\boldsymbol{n} = (-\eta_\alpha, \xi_\alpha)^T/\sqrt{J}$. We conclude that

$$\psi_\alpha = c\eta_\alpha, \qquad \varphi_\alpha = H[\psi_\alpha] = cH[\eta_\alpha] = c(\xi_\alpha - 1). \tag{3.2}$$

This expresses ψ and φ (up to additive constants) in terms of η and $\xi = \alpha + x_0 + H[\eta]$, leaving only η to be determined. As in the graph-based approach of (3.1) above, it suffices to compute the initial wave profile at $t = 0$ to know the full evolution of the traveling wave under (2.78); however, the wave generally travels at a non-uniform speed in conformal space in order to travel at constant speed in physical space.

The two-dimensional velocity potential $\Phi^{\text{phys}}(x, y, t)$ may be assumed to exist even if the traveling wave possesses overhanging regions that cause the graph-based representation via $\eta^{\text{phys}}(x, t)$ and $\varphi^{\text{phys}}(x, t)$ to break down. In a moving frame traveling at constant speed c along with the wave, the free surface will be a streamline. Let $\check{z} = z - ct$ denote position in the moving frame and note that the complex velocity potential picks up a background flow term, $\check{W}^{\text{phys}}(\check{z}, t) = W^{\text{phys}}(\check{z} + ct, t) - c\check{z}$, and becomes time-independent. We drop t in the notation and define $\check{W}(w) = \check{W}^{\text{phys}}(\check{z}(w))$, where $\check{z}(w) = z(w, 0)$ conformally maps the lower half-plane onto the fluid region of this stationary problem. We assume $W^{\text{phys}}(\check{z}(\alpha), 0)$ is quasi-periodic with exponentially decaying mode amplitudes, so

$$|\check{W}(w) + cw| \leq |W^{\text{phys}}(\check{z}(w), 0)| + c|\check{z}(w) - w| \tag{3.3}$$

is bounded in the lower half-plane. Since the stream function $\text{Im}\{\check{W}^{\text{phys}}(\check{z})\}$ is constant on the free surface, we may assume $\text{Im}\{\check{W}(\alpha)\} = 0$ for $\alpha \in \mathbb{R}$. The function $\text{Im}\{\check{W}(w) + cw\}$ is then bounded and harmonic in the lower half-plane and satisfies homogeneous Dirichlet boundary conditions on the real line, so it is zero [12]. Up to an additive real constant,

$$\check{W}(w) = -cw. \tag{3.4}$$

Thus, $|\check{\nabla}\check{\Phi}^{\text{phys}}|^2 = |\check{W}'(w)/\check{z}'(w)|^2 = c^2/J$. Since the free surface is a streamline in the moving frame, the steady Bernoulli equation $(1/2)|\check{\nabla}\check{\Phi}^{\text{phys}}|^2 + g\eta + P/\rho = C$ together with the Laplace-Young condition $P = P_0 - \rho\tau\kappa$ on the pressure gives

$$\begin{gathered} P\left[\frac{c^2}{2J} + g\eta - \tau\kappa\right] = 0, \\ \xi_\alpha = 1 + H[\eta_\alpha], \qquad J = \xi_\alpha^2 + \eta_\alpha^2, \qquad \kappa = \frac{\xi_\alpha \eta_{\alpha\alpha} - \eta_\alpha \xi_{\alpha\alpha}}{J^{3/2}}, \end{gathered} \tag{3.5}$$

which is the desired system of equations for η. The solution of the above equations can be considered as the initial condition for a traveling wave. Due to the projection operator, modifying η by a constant will not influence the governing equation, hence we always assume that $P_0[\eta] = 0$. Furthermore, by the symmetry of the above governing equation, if $\eta(\alpha)$ is a traveling solution, then $\eta(-\alpha)$ is also a traveling solution, therefore we focus our study on solutions with even symmetry

$$\eta(\alpha) = \eta(-\alpha). \tag{3.6}$$

We reconstruct ξ from η by

$$\xi = \alpha + H[\eta], \tag{3.7}$$

where we choose $x_0 = 0$ in (2.82), therefore ξ is an odd function.

3.2 Governing Equations of Quasi-Periodic Traveling Waves on the Torus

Using (3.5), we derive the governing equations of quasi-periodic traveling waves on the torus

$$\mathcal{R}[\tau, b, \tilde{\eta}] = P\left[\frac{b}{2\tilde{J}} + g\tilde{\eta} - \tau\tilde{\kappa}\right] = 0, \tag{3.8}$$

where $b = c^2$ and $\tilde{J}$, $\tilde{\kappa}$ are defined in (2.79). Linearizing (3.8) around the zero solution $\tilde{\eta} = 0$, we obtain

$$bH[\tilde{\partial}_\alpha \delta\tilde{\eta}] - g\delta\tilde{\eta} + \tau\tilde{\partial}_\alpha^2 \delta\tilde{\eta} = 0, \tag{3.9}$$

where $\delta\tilde{\eta}$ denotes the variation of $\tilde{\eta}$. Substituting (2.61) into the linearized equation, we obtain the dispersion relation for the linearized problem

$$b\left|\langle \boldsymbol{j}, \boldsymbol{k}\rangle\right| - g - \tau(\langle \boldsymbol{j}, \boldsymbol{k}\rangle)^2 = 0. \tag{3.10}$$

Since the entries of $\boldsymbol{k}$ are linearly independent over $\mathbb{Z}$, given b and τ, there exist at most four different vectors $\pm\boldsymbol{j}_1, \pm\boldsymbol{j}_2 \in \mathbb{Z}^d$ that satisfy the dispersion relation [19]. For simplicity, we restrict our discussion to the case where $d = 2$ and assume that η is a quasi-periodic function with two quasi-periods, thus $\tilde{\eta}$ is defined on $\mathbb{T}^2$. Without loss of generality, we also assume that $\boldsymbol{j}_1 = (1, 0)^T$, $\boldsymbol{j}_2 = (0, 1)^T$ and $\boldsymbol{k} = (1, k)^T$, where k is a positive irrational number. Therefore the quasi-periodic function η is of the following form

$$\eta(\alpha) = \tilde{\eta}(\alpha, k\alpha), \qquad \tilde{\eta}(\alpha_1, \alpha_2) = \sum_{j_1, j_2 \in \mathbb{Z}} \hat{\eta}_{j_1, j_2} e^{i(j_1\alpha_1 + j_2\alpha_2)}. \tag{3.11}$$

Since we assume that $P_0[\eta] = 0$ and η is even, here $\tilde{\eta}$ is an even function with zero mean on $\mathbb{T}^2$, thus the Fourier coefficients of $\tilde{\eta}$ satisfy

$$\hat{\eta}_{0,0} = 0, \qquad \hat{\eta}_{j_1, j_2} = \hat{\eta}_{-j_1, -j_2} \in \mathbb{R}. \tag{3.12}$$

According to (3.7), $\tilde{\xi} = H[\tilde{\eta}]$ is an odd function. Under the above assumptions, one can study the problem of quasi-periodic traveling waves in the setting of a bifurcation problem with a two-dimensional kernel, where the solutions can be considered as bifurcations of the zero-amplitude solution. In our study, we choose the two Fourier coefficients $\hat{\eta}_{1,0}$ and $\hat{\eta}_{0,1}$ as bifurcation parameters and fix them at nonzero values to ensure that the solutions we obtain are quasi-periodic. We say that these two Fourier coefficients are base Fourier coefficients and the corresponding Fourier modes $e^{\pm i\alpha_1}$, $e^{\pm i\alpha_2}$ are base Fourier modes.

Remark 3.2.1 *One can check that if* $\tilde{\eta}(\alpha_1, \alpha_2) = \sum_{j_1, j_2 \in \mathbb{Z}} \hat{\eta}_{j_1, j_2} e^{i(j_1\alpha_1 + j_2\alpha_2)}$ *is a solution of (3.8), then the following three functions are also solutions*

$$\begin{aligned}
&\tilde{\eta}(\alpha_1 + \pi, \alpha_2) \sum_{j_1, j_2 \in \mathbb{Z}} (-1)^{j_1} \hat{\eta}_{j_1, j_2} e^{i(j_1\alpha_1 + j_2\alpha_2)}, \\
&\tilde{\eta}(\alpha_1, \alpha_2 + \pi) = \sum_{j_1, j_2 \in \mathbb{Z}} (-1)^{j_2} \hat{\eta}_{j_1, j_2} e^{i(j_1\alpha_1 + j_2\alpha_2)}, \\
&\tilde{\eta}(\alpha_1 + \pi, \alpha_2 + \pi) = \sum_{j_1, j_2 \in \mathbb{Z}} (-1)^{j_1 + j_2} \hat{\eta}_{j_1, j_2} e^{i(j_1\alpha_1 + j_2\alpha_2)}.
\end{aligned} \tag{3.13}$$

Remark 3.2.2 *Even though we derive the governing equations (3.5) in the spatially quasi-periodic setting, it is still true in the periodic setting, where we have*

$$\eta(\alpha) = \sum_{j \in \mathbb{Z}} \hat{\eta}_j e^{ij\alpha}, \qquad H[\eta](\alpha) = \sum_{j \in \mathbb{Z}} (-i)\,\mathrm{sgn}(j) \hat{\eta}_j e^{ij\alpha}. \tag{3.14}$$

In correspondence, the equation (3.8) can also extend to the periodic setting if we let

$$\tilde{\eta}(\alpha_1, \alpha_2) = \tilde{\eta}(\alpha_1). \tag{3.15}$$

3.3 Weakly Nonlinear Approximation of Quasi-Periodic Traveling Waves

In this section, we will construct weakly nonlinear approximations of the quasi-periodic traveling solutions of the form (3.11). As discussed in Section 3.2, the traveling solutions are inditified by two bifurcation parameters $\hat{\eta}_{1,0}$ and $\hat{\eta}_{0,1}$, which are fixed at nonzero values. In correspondence, these two Fourier coefficients are fixed parameters for the asymptotic solution and our goal is to express b, τ and the other Fourier coefficients of $\tilde{\eta}$ in terms of these two Fourier coefficients. We consider the following asymptotic expansions of b, τ and $\tilde{\eta}$

$$\begin{aligned}
b =& b^{(0)} + \epsilon b^{(1)} + \epsilon^2 b^{(2)} + \epsilon^3 b^{(3)} + O(\epsilon^4), \\
\tau =& \tau^{(0)} + \epsilon \tau^{(1)} + \epsilon^2 \tau^{(2)} + \epsilon^3 \tau^{(3)} + O(\epsilon^4), \\
\tilde{\eta} =& \epsilon \tilde{\eta}^{(1)} + \epsilon^2 \tilde{\eta}^{(2)} + \epsilon^3 \tilde{\eta}^{(3)} + O(\epsilon^4),
\end{aligned} \tag{3.16}$$

where ϵ is a sufficiently small number. Substituting the above expressions into (3.8) and eliminating the coefficients of ϵ^n for $n = 0, 1, 2$, we establish

$$\begin{aligned}
O(1): \quad & P\left[\frac{1}{2}b^{(0)}\right] = 0, \\
O(\epsilon): \quad & P\left[\frac{1}{2}b^{(1)} + g\tilde{\eta}^{(1)} - b^{(0)}H[\tilde{\partial}_\alpha\tilde{\eta}^{(1)}] - \tau^{(0)}\tilde{\partial}_\alpha^2\tilde{\eta}^{(1)}\right] = 0, \\
O(\epsilon^2): \quad & P\Big[\frac{1}{2}b^{(2)} + g\tilde{\eta}^{(2)} - b^{(0)}H[\tilde{\partial}_\alpha\tilde{\eta}^{(2)}] - \tau^{(0)}\tilde{\partial}_\alpha^2\tilde{\eta}^{(2)} \\
& \quad - b^{(1)}H[\tilde{\partial}_\alpha\tilde{\eta}^{(1)}] - \tau^{(1)}\tilde{\partial}_\alpha^2\tilde{\eta}^{(1)} \\
& \quad + b^{(0)}\left(\frac{3}{2}\left(H[\tilde{\partial}_\alpha\tilde{\eta}^{(1)}]\right)^2 - \frac{1}{2}(\tilde{\partial}_\alpha\tilde{\eta}^{(1)})^2\right) \\
& \quad + \tau^{(0)}\left(2H[\tilde{\partial}_\alpha\tilde{\eta}^{(1)}]\tilde{\partial}_\alpha^2\tilde{\eta}^{(1)} + H[\tilde{\partial}_\alpha^2\tilde{\eta}^{(1)}]\tilde{\partial}_\alpha\tilde{\eta}^{(1)}\right)\Big] = 0.
\end{aligned} \tag{3.17}$$

Since the constant term will vanish under the projection, we rewrite the equation at order ϵ as

$$P\left[b^{(0)}H[\tilde{\partial}_\alpha\tilde{\eta}^{(1)}] - g\tilde{\eta}^{(1)} + \tau^{(0)}\tilde{\partial}_\alpha^2\tilde{\eta}^{(1)}\right] = 0. \tag{3.18}$$

As discussed in Section 3.11, $\tilde{\eta}^{(1)}$ takes the form

$$\tilde{\eta}^{(1)} = \hat{\eta}_{1,0}e^{i\alpha_1} + \hat{\eta}_{0,1}e^{i\alpha_2} + c.c., \qquad \hat{\eta}_{1,0},\ \hat{\eta}_{0,1} \neq 0. \tag{3.19}$$

where $c.c$ means the complex conjugate of the preceding terms.

Substituting the expression of $\tilde{\eta}^{(1)}$ back into (3.18), we obtain

$$b^{(0)} = g + \frac{g}{k}, \qquad \tau^{(0)} = \frac{g}{k}. \tag{3.20}$$

Using the property of the projection operator and the assumption that $P_0[\tilde{\eta}] = 0$, we rewrite the equation at order ϵ^2 as

$$\begin{aligned}
&\underbrace{g\tilde{\eta}^{(2)} - b^{(0)}H[\tilde{\partial}_\alpha\tilde{\eta}^{(2)}] - \tau^{(0)}\tilde{\partial}_\alpha^2\tilde{\eta}^{(2)}}_{A^{(2)}}\underbrace{-b^{(1)}H[\tilde{\partial}_\alpha\tilde{\eta}^{(1)}] - \tau^{(1)}\tilde{\partial}_\alpha^2\tilde{\eta}^{(1)}}_{B^{(2)}} \\
&= \underbrace{P\left[b^{(0)}\left(-\frac{3}{2}\left(H[\tilde{\partial}_\alpha\tilde{\eta}^{(1)}]\right)^2 + \frac{1}{2}(\tilde{\partial}_\alpha\tilde{\eta}^{(1)})^2\right) - \tau^{(0)}\left(2H[\tilde{\partial}_\alpha\tilde{\eta}^{(1)}]\tilde{\partial}_\alpha^2\tilde{\eta}^{(1)} + H[\tilde{\partial}_\alpha^2\tilde{\eta}^{(1)}]\tilde{\partial}_\alpha\tilde{\eta}^{(1)}\right)\right]}_{C^{(2)}}.
\end{aligned} \tag{3.21}$$

Substituting (3.19) and (3.20) into $C^{(2)}$, we have

$$C^{(2)} = \hat{C}^{(2)}_{2,0}e^{i(2\alpha_1)} + \hat{C}^{(2)}_{0,2}e^{i(2\alpha_2)} + \hat{C}^{(2)}_{1,1}e^{i(\alpha_1+\alpha_2)} + \hat{C}^{(2)}_{1,-1}e^{i(\alpha_1-\alpha_2)} + c.c., \tag{3.22}$$

where the Fourier coefficients are given by

$$\begin{aligned} \hat{C}^{(2)}_{2,0} &= -\hat{\eta}^2_{1,0} g \frac{2k-1}{k}, & \hat{C}^{(2)}_{0,2} &= \hat{\eta}^2_{0,1} g k(k-2), \\ \hat{C}^{(2)}_{1,1} &= -\hat{\eta}_{1,0}\hat{\eta}_{0,1} g(k+1), & \hat{C}^{(2)}_{1,-1} &= -\hat{\eta}_{1,0}\hat{\eta}_{0,1} g(k+1). \end{aligned} \tag{3.23}$$

One can see that $A^{(2)}$ is linear with respect to $\tilde{\eta}^{(2)}$ and the Fourier coefficients of $A^{(2)}$ are

$$\hat{A}^{(2)}_{j_1,j_2} = \hat{S}_{j_1,j_2}\hat{\eta}^{(2)}_{j_1,j_2}, \tag{3.24}$$

where the symbol $\hat{S}_{j_1,j_2}$ is defined as

$$\hat{S}_{j_1,j_2} = g - b^{(0)}|j_1 + kj_2| + \tau^{(0)}(j_1 + kj_2)^2 = \frac{g}{k}(|j_1 + kj_2| - k)(|j_1 + kj_2| - 1). \tag{3.25}$$

Since $\hat{S}_{\pm1,0}$ and $\hat{S}_{0,\pm1}$ are both zero according to the definition, we know that $\hat{A}^{(2)}_{\pm1,0} = \hat{A}^{(2)}_{0,\pm1} = 0$.

The term $B^{(2)}$ in (3.21) is linear with respect to $\tilde{\eta}^{(1)}$

$$\hat{B}^{(2)}_{j_1,j_2} = \hat{Q}^{(1)}_{j_1,j_2}\hat{\eta}^{(1)}_{j_1,j_2}, \qquad \hat{Q}^{(1)}_{j_1,j_2} = -b^{(1)}|j_1 + kj_2| + \tau^{(1)}(j_1 + kj_2)^2, \tag{3.26}$$

where $(j_1, j_2) = (\pm1, 0), (0, \pm1)$ according to (3.19). Combining (3.22, 3.24 – 3.26), we obtain that

$$b^{(1)} = \tau^{(1)} = 0, \qquad \hat{\eta}^{(2)}_{j_1,j_2} = \begin{cases} \frac{C^{(2)}_{j_1,j_2}}{\hat{S}_{j_1,j_2}}, & |j_1| + |j_2| = 2, \\ 0, & |j_1| + |j_2| \neq 2. \end{cases} \tag{3.27}$$

By induction, at order ϵ^n, the equation of asymptotic expansions reads

$$\begin{aligned} & g\tilde{\eta}^{(n)} - b^{(0)}H[\tilde{\partial}_\alpha\tilde{\eta}^{(n)}] - \tau^{(0)}\tilde{\partial}^2_\alpha\tilde{\eta}^{(n)} - b^{(n-1)}H[\tilde{\partial}_\alpha\tilde{\eta}^{(1)}] - \tau^{(n-1)}\tilde{\partial}^2_\alpha\tilde{\eta}^{(1)} \\ &= \underbrace{f\left(\left(b^{(j)}\right)_{0\le j\le n-1}, \left(\tau^{(j)}\right)_{0\le j\le n-1}, \left(\tilde{\eta}^{(j)}\right)_{0\le j\le n-1}\right)}_{C^{(n)}}. \end{aligned} \tag{3.28}$$

By comparing the Fourier coefficients of both sides of the above equation, we obtain

$$\hat{S}_{j_1,j_2}\hat{\eta}^{(n)}_{j_1,j_2} + \hat{Q}^{(n-1)}_{J_1,j_2}\hat{\eta}^{(1)}_{j_1,j_2} = \hat{C}^{(n)}_{j_1,j_2}. \tag{3.29}$$

Hence we have

$$\begin{aligned} \hat{\eta}^{(n)}_{j_1,j_2} &= \frac{\hat{C}^{(n)}_{j_1,j_2}}{\hat{S}_{j_1,j_2}}, & (j_1, j_2) &\neq (\pm1, 0), (0, \pm1), \\ b^{(n-1)} &= \frac{\frac{\hat{C}^{(n)}_{0,1}}{\hat{\eta}_{0,1}} - k^2\frac{\hat{C}^{(n)}_{1,0}}{\hat{\eta}_{1,0}}}{k^2 - k}, & \tau^{(n-1)} &= \frac{\frac{\hat{C}^{(n)}_{0,1}}{\hat{\eta}_{0,1}} - k\frac{\hat{C}^{(n)}_{1,0}}{\hat{\eta}_{1,0}}}{k^2 - k}. \end{aligned} \tag{3.30}$$

As is shown above, the Fourier coefficients of $\tilde{\eta}^{(n)}$ are obtained through a division of $\hat{S}_{j_1,j_2}$ for $(j_1, j_2) \neq (\pm 1, 0), (0, \pm 1)$. Recalling that

$$\hat{S}_{j_1,j_2} = \frac{g}{k}(|j_1 + kj_2| - k)(|j_1 + kj_2| - 1), \tag{3.31}$$

one can notice that $\hat{S}_{j_1,j_2}$ may get arbitrarily close to zero as $|j_1|, |j_2|$ approach infinity; this will lead to the unboundedness of $\hat{\eta}^{(n)}_{j_1,j_2}$, which is also known as the small divisor problem. As a consequence, to ensure the existence of quasi-periodic traveling solutions, one generally assume that k is irrational enough; in other words, k should satisfy the following diophantine condition [62]

$$|k - j_1/j_2| > C|j_2|^{-\nu}, \qquad j_1 \in \mathbb{Z},\ j_2 \in \mathbb{Z}\backslash\{0\}, \tag{3.32}$$

where C is a positive constant and $\nu > 2$. The appearance of small divisors also indicates that the amplitudes of these solutions are rather small [62].

Remark 3.3.1 *If the asymptotic expansion of the surface elevation in physical space reads*

$$\tilde{\eta}^{phys} = \epsilon\tilde{\eta}^{phys^{(1)}} + \epsilon^2\tilde{\eta}^{phys^{(2)}} + \epsilon^3\tilde{\eta}^{phys^{(3)}} + O(\epsilon^4), \tag{3.33}$$

the quasi-periodic surface elevations in physical space and conformal space are given by

$$\tilde{\eta}^{phys}(\boldsymbol{\alpha} + \boldsymbol{k}\tilde{\xi}(\boldsymbol{\alpha})) = \tilde{\eta}(\boldsymbol{\alpha}) \tag{3.34}$$

and

$$\tilde{\eta}^{phys} = \epsilon\tilde{\eta}^{phys^{(1)}} + \epsilon^2\left(\tilde{\partial}_\alpha\tilde{\eta}^{phys^{(1)}}H[\tilde{\eta}^{(1)}] + \tilde{\eta}^{phys^{(2)}}\right) + O(\epsilon^3), \tag{3.35}$$

comparing (3.33) and (3.35) , we conclude that

$$\begin{aligned}
\tilde{\eta}^{phys^{(1)}}(x_1, x_2) &= \hat{\eta}_{1,0}e^{ix_1} + \hat{\eta}_{0,1}e^{ix_2} + c.c., \\
\tilde{\eta}^{phys^{(2)}}(x_1, x_2) &= \frac{k+1}{k-2}\hat{\eta}^2_{1,0}e^{i(2x_1)} + \frac{(k+1)k}{1-2k}\hat{\eta}^2_{0,1}e^{i(2x_2)} \\
&\quad - 2(k+1)\hat{\eta}_{1,0}\hat{\eta}_{0,1}e^{i(x_1+x_2)} + \frac{2(k^2-1)}{k-2}\hat{\eta}_{1,0}\hat{\eta}_{0,1}e^{i(x_1-x_2)} + c.c.,
\end{aligned} \tag{3.36}$$

which are the same as the results in [19].

3.4 Quasi-Periodic Traveling Waves That Bifurcate From Periodic Traveling Waves

In the preceding section, we discuss traveling solutions that bifurcate from the zero-amplitude solution, which are identified by two bifurcation parameters $\hat{\eta}_{1,0}$ and $\hat{\eta}_{0,1}$. In

this section, we are going to study a different family of quasi-periodic traveling solutions - solutions that bifurcate from finite-amplitude periodic traveling solutions. As discussed in Remark 3.2.2, the governing equation (3.8) still holds in the periodic case, where we have $\tilde{\eta}(\alpha_1, \alpha_2) = \tilde{\eta}(\alpha_1)$ and the periodic function η can be reconstructed from $\tilde{\eta}$ using (3.11). To tell apart periodic solutions and quasi-periodic solutions, we introduce the following definition.

Definition 3.4.1 *Let $\tilde{f} \in L^2(\mathbb{T})$ be a real function. The function $\tilde{f}$ is said to be periodic if $\tilde{f}(\alpha_1, \alpha_2) = \tilde{f}(\alpha_1)$, for $\alpha_1, \alpha_2 \in \mathbb{T}$, which is equivalent to $\hat{f}_{j_1, j_2} = 0$ for $j_2 \neq 0$. When $\tilde{f}$ is periodic, we drop the dependence of $\tilde{f}$ on α_2 and represent it as $\tilde{f}^{per}(\alpha_1)$. The function $\tilde{f}$ is said to be quasi-periodic if it is not periodic, denoted $\tilde{f}^{qua}$. If $\tilde{f}^{qua}$ further satisfies $\hat{f}_{j_1,0} = 0$ for $j_1 \in \mathbb{Z}$, we call it purely quasi-periodic and denote it as $\tilde{f}^{p\text{-}qua}$.*

To avoid the confusion of different definitions of "periodic", we refer periodic functions defined on $\mathbb{T}^2$ as tilde functions.

We introduce a new variable q and write the governing equation (3.8) as

$$\mathcal{R}[q] = P\left[\frac{b}{2\tilde{J}} + g\tilde{\eta} - \tau\tilde{\kappa}\right] = 0, \qquad q = (\tau, b, \tilde{\eta}). \tag{3.37}$$

One can compute the Frechet derivative of $\mathcal{R}$, denoted $D_q\mathcal{R} = (D_\tau\mathcal{R}, D_b\mathcal{R}, D_{\tilde{\eta}}\mathcal{R})$ through the linearization of (3.37)

$$\begin{aligned}
\delta\mathcal{R} &= P\left[\frac{1}{2\tilde{J}}\delta b - \frac{1}{2\tilde{J}^2}b\delta\tilde{J} + g\delta\tilde{\eta} - \tau\delta\tilde{\kappa} - \tilde{\kappa}\delta\tau\right], \\
\delta\tilde{\xi} = H[\delta\tilde{\eta}], &\qquad \delta\tilde{J} = 2\left\{(1+\tilde{\partial}_\alpha\tilde{\xi})(\tilde{\partial}_\alpha\tilde{\xi}) + (\tilde{\partial}_\alpha\tilde{\eta})(\tilde{\partial}_\alpha\delta\tilde{\eta})\right\}, \\
\delta\tilde{\kappa} &= -\frac{3}{2\tilde{J}}\tilde{\kappa}\delta\tilde{J} + \frac{1}{\tilde{J}^{3/2}}\left\{(\tilde{\partial}_\alpha^2\tilde{\eta})(\tilde{\partial}_\alpha\delta\tilde{\xi}) + (1+\tilde{\partial}_\alpha\tilde{\xi})(\tilde{\partial}_\alpha^2\delta\tilde{\eta})\right. \\
&\qquad \left. -(\tilde{\partial}_\alpha^2\tilde{\xi})(\tilde{\partial}_\alpha\delta\tilde{\eta}) - (\tilde{\partial}_\alpha\tilde{\eta})(\tilde{\partial}_\alpha^2\delta\tilde{\xi})\right\}.
\end{aligned} \tag{3.38}$$

We denote the point q where $\tilde{\eta}$ is periodic by q^{per}, the point of form $q = (0, 0, \tilde{\eta}^{\text{qua}})$ by q^{qua} and the point of form $q = (0, 0, \tilde{\eta}^{\text{p-qua}})$ by $q^{\text{p-qua}}$. One can check that at q^{per}, the Frechet derivative $D_q\mathcal{R}$ satisfies the following properties.

(1) For $\delta q = \left(\delta\tau, \delta b, e^{i(l_1\alpha_1)}\right)$, where $l_1 \in \mathbb{Z}$, $\delta b, \delta\tau \in \mathbb{R}$, we have

$$D_q\mathcal{R}\left[q^{\text{per}}\right]\delta q = \sum_{j\in\mathbb{Z}} \hat{g}_j^{(l_1)} e^{ij\alpha_1}. \tag{3.39}$$

(2) For $\delta q = \left(0, 0, e^{i(l_1\alpha_1 + l_2\alpha_2)}\right)$, where $l_1 \in \mathbb{Z}$, $l_2 \in \mathbb{Z}\backslash\{0\}$, we have

$$D_q\mathcal{R}\left[q^{\text{per}}\right]\delta q = e^{il_2\alpha_2}\sum_{j\in\mathbb{Z}} \hat{g}_j^{(l_1)} e^{ij\alpha_1}. \tag{3.40}$$

In computation, we always represent $\tilde{\eta}$ and $\mathcal{R}$ by their truncated Fourier series thus (3.37) is a finite-dimensional problem and our following discussion will be based on this context. Due to the symmetry of (3.8), we restrict our discussion to tilde functions that satisfy the assumption (3.12). We also assume that the functions involved in (3.37) are smooth enough. Following [6, 23, 24], we parametrize the solution curve of $\mathcal{R} = 0$ by an arc-length parameter s, denoted $\mathfrak{q}(s)$. A solution curve is said to be periodic if it only passes through points with periodic $\tilde{\eta}$, denoted $\mathfrak{q}^{\text{per}}(s)$; otherwise we call it quasi-periodic, denoted $\mathfrak{q}^{\text{qua}}(s)$. In the scope of this paper, we only study simple quasi-periodic bifurcation points on $\mathfrak{q}^{\text{per}}(s)$; a point is said to be a simple quasi-periodic bifurcation point if a quasi-periodic solution curve intersects $\mathfrak{q}^{\text{per}}(s)$ non-tangentially at this point.

We introduce the definition of a simple quasi-periodic bifurcation point as follows, which is analogous to the definition of a simple bifurcation point in [6].

Definition 3.4.2 *Supposing that $q^{bif} = (\tau^{bif}, b^{bif}, \tilde{\eta}^{bif})$ with $\tilde{\eta}^{bif}$ periodic satisfies $\mathcal{R}[q^{bif}] = 0$. We say that q^{bif} is a simple quasi-periodic bifurcation point if the following conditions hold:*

(1) $\ker D_q\mathcal{R}[q^{bif}] = \text{span}\{\delta q^{per}, \delta q^{p\text{-}qua}\}$, *where* $\delta q^{per} = (\delta\tau^{per}, \delta b^{per}, \delta\tilde{\eta}^{per})$ *and* $\delta q^{p\text{-}qua} = (0, 0, \delta\tilde{\eta}^{p\text{-}qua})$.

(2) $\text{coker}\, D_q\mathcal{R}[q^{bif}] = \text{span}\{\tilde{w}^{p\text{-}qua}\}$.

(3) $\rho := \langle \tilde{w}^{p\text{-}qua}, D_q^2\mathcal{R}[q^{bif}](\delta q^{per}, \delta q^{p\text{-}qua})\rangle \neq 0$, *where $\langle\cdot,\cdot\rangle$ denotes the usual L^2 inner product.*

Remark 3.4.3 *In [6], the solution q_0 is called a simple bifurcation point if*

(1) $\dim\ker D_q\mathcal{R}[q_0] = 2$,

(2) $\dim\text{coker}\, D_q\mathcal{R}[q_0] = 1$,

(3) $\det H < 0$, *where H is a two-by-two matrix with entries*

$$H_{j_1,j_2} = \langle w, D_q^2\mathcal{R}[q_0](\delta q^{(j_1)}, \delta q^{(j_2)})\rangle, \qquad j_1, j_2 = 1, 2, \tag{3.41}$$

where $\ker D_q\mathcal{R}[q_0] = \text{span}\{\delta q^{(1)}, \delta q^{(2)}\}$, $\text{coker}\, D_q\mathcal{R}[q_0] = \text{span}\{w\}$.

Due to the structure of $D_q\mathcal{R}[q_0]$, we are able to further assume that $\delta q^{(1)} = \delta q^{per}$, $\delta q^{(2)} = \delta q^{p\text{-}qua}$ and $w = \tilde{w}^{p\text{-}qua}$ in Definition 3.4.2. Since we know that $\langle w^{p\text{-}qua}, D_q^2\mathcal{R}[q^{bif}](\delta q^{per}, \delta q^{per})\rangle = 0$ from (3.39), the condition (3) in Definition 3.4.2 is equivalent to the condition that $\det H < 0$.

As shown in [6], one can use Lyapunov-Schmidt decomposition and the implicit function theorem to prove that if q^{bif} is bifurcation point for the quasi-periodic branch, then there exists $\mathfrak{q}^{\text{per}}(s)$, $\mathfrak{q}^{\text{qua}}(s)$ such that $q^{\text{bif}} = \mathfrak{q}^{\text{per}}(0) = \mathfrak{q}^{\text{qua}}(0)$ and

$$\dot{\mathfrak{q}}^{\text{per}}(0) = a_1\delta q^{\text{per}}, \qquad \dot{\mathfrak{q}}^{\text{qua}}(0) = a_2\delta q^{\text{per}} + a_3\delta q^{\text{p-qua}}, \qquad a_1 \neq 0, \quad a_3 \neq 0. \tag{3.42}$$

We consider $\mathfrak{q}^{\mathrm{per}}(s)$ as the primary branch and $\mathfrak{q}^{\mathrm{qua}}(s)$ as a secondary quasi-periodic bifurcation branch from $\mathfrak{q}^{\mathrm{per}}(s)$. We obtain $\mathfrak{q}^{\mathrm{per}}(s)$ by fixing either τ or $\hat{\eta}_{1,0}$ and choosing the other one as the continuation parameter. In order to compute the curve $\mathfrak{q}^{\mathrm{qua}}(s)$, we first detect the bifurcation point q^{bif} on $\mathfrak{q}^{\mathrm{per}}(s)$, then compute the bifurcation direction $\dot{\mathfrak{q}}^{\mathrm{qua}}(0)$ and eventually use $q^{\mathrm{bif}} + \epsilon\dot{\mathfrak{q}}^{\mathrm{qua}}(0)$ as an initial guess to switch from $\mathfrak{q}^{\mathrm{per}}(s)$ to $\mathfrak{q}^{\mathrm{qua}}(s)$.

We detect the bifurcation point q^{bif} on the primary branch by examining the behavior of $D_q\mathcal{R}$ along this branch. Let $\{\delta\tilde{\eta}^{(l)}\}_{1\le l\le n}$ denote a basis of purely quasi-periodic functions and denote

$$\delta q^{(j)} = (0, 0, \delta\tilde{\eta}^{(j)}), \qquad j = 1, 2, \ldots, n. \tag{3.43}$$

We assume that $\delta q^{(1)} \in \ker D_q\mathcal{R}[q^{\mathrm{bif}}]$ without loss of generality. Let $\{\tilde{w}^{(l)}\}_{1\le l\le n}$ denote a basis for purely quasi-periodic functions and assume that

$$\tilde{w}^{(1)} \in \operatorname{coker} D_q\mathcal{R}[q^{\mathrm{bif}}]. \tag{3.44}$$

We consider the n-by-n matrix M along $\mathfrak{q}^{\mathrm{per}}(s)$ where the entries of M are given by

$$M_{j_1,j_2}[\mathfrak{q}^{\mathrm{per}}(s)] = \langle \tilde{w}^{(j_1)}, D_x\mathcal{R}[\mathfrak{q}^{\mathrm{per}}(s)]\delta q^{(j_2)}\rangle, \qquad j_1, j_2 = 1, 2, \ldots n. \tag{3.45}$$

Since $\mathfrak{q}^{\mathrm{per}}(0) = q^{\mathrm{bif}}$, near $s = 0$, we have

$$M_{j_1,j_2}[\mathfrak{q}^{\mathrm{per}}(s)] = \langle \tilde{w}^{(j_1)}, D_q\mathcal{R}[q^{\mathrm{bif}}]\delta q^{(j_2)}\rangle + \langle \tilde{w}^{(j_1)}, D_q^2\mathcal{R}[q^{\mathrm{bif}}](\dot{\mathfrak{q}}^{\mathrm{per}}(0), \delta q^{(j_2)})\rangle s + O(s^2). \tag{3.46}$$

Hence we obtain

$$M[\mathfrak{q}^{\mathrm{per}}(s)] = \begin{pmatrix} \rho s + O(s^2) & O(s) \\ O(s) & M_{\mathrm{sub}}[\mathfrak{q}^{\mathrm{per}}(s)] \end{pmatrix}, \tag{3.47}$$

where the $(n-1)$-by-$(n-1)$ matrix $M_{\mathrm{sub}}[\mathfrak{q}^{\mathrm{per}}(s)]$ is invertible at $s = 0$ because of Definition 3.4.2. The Taylor expansion of the determinant of M around $s = 0$ reads

$$\det M[\mathfrak{q}^{\mathrm{per}}(s)] = \rho s \det M_{\mathrm{sub}}[q^{\mathrm{bif}}] + O(s^2). \tag{3.48}$$

One can observe that $\det M[\mathfrak{q}^{\mathrm{per}}(s)]$ changes sign at the bifurcation point $\mathfrak{q}^{\mathrm{per}}(0) = q^{\mathrm{bif}}$. The above equation also demonstrates that $s = 0$ is a simple zero of $M[\mathfrak{q}^{\mathrm{per}}(s)]$. In practice, we locate the bifurcation points by tracking the sign of $\det M[\mathfrak{q}^{\mathrm{per}}(s)]$ [23, 24, 76].

Suppose that we have found the bifurcation point q^{bif} on $\mathfrak{q}^{\mathrm{per}}(s)$, we now are going to compute the bifurcation direction $\dot{\mathfrak{q}}^{\mathrm{qua}}(0)$ at q^{bif}, which is equivalent to finding the relation between a_2 and a_3 in (3.42). Computing the second derivative of $\mathcal{R}[\mathfrak{q}^{\mathrm{qua}}(s)]$ with respect to s at $s = 0$, we have

$$D_q^2\mathcal{R}[q^{\mathrm{bif}}](\dot{\mathfrak{q}}^{\mathrm{qua}}(0), \dot{\mathfrak{q}}^{\mathrm{qua}}(0)) + D_q\mathcal{R}[q^{\mathrm{bif}}]\ddot{\mathfrak{q}}^{\mathrm{qua}}(0) = 0. \tag{3.49}$$

Substituting (3.42) into the above equation and taking the inner product with $\tilde{w}^{\text{p-qua}} \in \operatorname{coker} D_q\mathcal{R}[q^{\mathrm{bif}}]$ both sides, we obtain

$$2a_2\rho + a_3\langle \tilde{w}^{\text{p-qua}}, D_q^2\mathcal{R}[q^{\mathrm{bif}}](\delta q^{\text{p-qua}}, \delta q^{\text{p-qua}})\rangle = 0. \tag{3.50}$$

Since $\rho \neq 0$ by Definition 3.4.2, we have

$$a_2 = -\frac{1}{2\rho} a_3 \langle \tilde{w}^{\text{p-qua}}, D_q^2 \mathcal{R}[q^{\text{bif}}](\delta q^{\text{p-qua}}, \delta q^{\text{p-qua}}) \rangle, \tag{3.51}$$

thus we obtain the quasi-periodic bifurcation direction $\dot{q}^{\text{qua}}(0)$. Once we obtain $\dot{q}^{\text{qua}}(0)$, we use $q^{\text{bif}} + \epsilon \dot{q}^{\text{qua}}(0)$ as an initial guess to compute the quasi-periodic traveling solution to jump from the periodic branch to the quasi-periodic branch. The details of computing the quasi-periodic branch will be discussed in Section 4.1.2.

Remark 3.4.4 *According to the property (3.40), it is reasonable to assume that $\delta\tilde{\eta}^{p\text{-}qua}$ and $\tilde{w}^{p\text{-}qua}$ in Definition 3.4.2 take the form*

$$\delta\tilde{\eta}^{p\text{-}qua} = e^{il_2\alpha_2} \sum_{j\in\mathbb{Z}} \delta\hat{\eta}_j e^{ij\alpha_1} + c.c., \quad \tilde{w}^{p\text{-}qua} = e^{il_2\alpha_2} \sum_{j\in\mathbb{Z}} \hat{w}_j e^{ij\alpha_1} + c.c., \quad l_2 \in \mathbb{N}\backslash\{0\}, \tag{3.52}$$

where the Fourier coefficients of $\delta\tilde{\eta}^{p\text{-}qua}$, $\tilde{w}^{p\text{-}qua}$ are real. In general, we are interested in quasi-periodic solutions of which the Fourier modes $e^{i(j_1\alpha_1 + j_2\alpha_2)}$ with $|j_2| \leq 1$ are dominant, hence we usually let $l_2 = 1$ in the formulas above. In this case, one can check that

$$\langle \tilde{w}^{p\text{-}qua}, D_q^2 \mathcal{R}[q^{bif}](\delta q^{p\text{-}qua}, \delta q^{p\text{-}qua}) \rangle = 0, \tag{3.53}$$

thus

$$\dot{q}^{qua}(0) = a_2 \delta q^{p\text{-}qua} = a_2(0, 0, \delta\tilde{\eta}^{p\text{-}qua}). \tag{3.54}$$

Chapter 4

Numerical Methods and Results

4.1 Traveling Quasi-Periodic Waves

4.1.1 Solutions That Bifurcate From the Zero Solution

4.1.1.1 Numerical Methods

Let $f(\alpha)$ denote a quasi-periodic function with two quasi-periods, and let $\tilde{f}$ denote the corresponding periodic function on the torus,

$$f(\alpha) = \tilde{f}(\alpha, k\alpha), \qquad \tilde{f}(\alpha_1, \alpha_2) = \sum_{j_1, j_2 \in \mathbb{Z}} \hat{f}_{j_1, j_2} e^{i(j_1\alpha_1 + j_2\alpha_2)}, \qquad (\alpha_1, \alpha_2) \in \mathbb{T}^2. \tag{4.1}$$

Each $\tilde{f}$ that arises is represented by its values on a uniform $M_1 \times M_2$ grid on the torus $\mathbb{T}^2$,

$$\tilde{f}_{m_1, m_2} = \tilde{f}(2\pi m_1/M_1\ ,\ 2\pi m_2/M_2), \qquad 0 \le m_1 < M_1\ ,\ 0 \le m_2 < M_2. \tag{4.2}$$

Products, powers and quotients in (3.5) are evaluated pointwise on the grid while derivatives and the Hilbert transform are computed in Fourier space via

$$\begin{aligned} \tilde{\partial}_\alpha \tilde{f}(\alpha_1, \alpha_2) &= \sum_{j_1, j_2 \in \mathbb{Z}} i(j_1 + j_2 k) \hat{f}_{j_1, j_2} e^{i(j_1\alpha_1 + j_2\alpha_2)}, \\ H[\tilde{f}](\alpha_1, \alpha_2) &= \sum_{j_1, j_2 \in \mathbb{Z}} (-i)\mathrm{sgn}(j_1 + j_2 k) \hat{f}_{j_1, j_2} e^{i(j_1\alpha_1 + j_2\alpha_2)}. \end{aligned} \tag{4.3}$$

We use the 'r2c' version of the 2d FFTW library to rapidly compute the forward and inverse transform given by

$$\hat{f}_{j_1, j_2} = \frac{1}{M_2} \sum_{m_2=0}^{M_2-1} \left(\frac{1}{M_1} \sum_{m_1=0}^{M_1-1} \tilde{f}_{m_1, m_2} e^{-2\pi i j_1 m_1/M_1} \right) e^{-2\pi i j_2 m_2/M_2}, \quad \begin{pmatrix} 0 \le j_1 \le M_1/2 \\ -M_2/2 < j_2 \le M_2/2 \end{pmatrix}. \tag{4.4}$$

The FFTW library actually returns the index range $0 \le j_2 < M_2$, but we use $\hat{f}_{j_1,j_2-M_2} = \hat{f}_{j_1,j_2}$ to de-alias the Fourier modes and map the indices $j_2 > M_2/2$ to their correct negative values. The missing entries with $-M_1/2 < j_1 < 0$ are determined implicitly by

$$\hat{f}_{-j_1,-j_2} = \overline{\hat{f}_{j_1,j_2}}. \tag{4.5}$$

When computing $\tilde{\partial}_\alpha f$ and $H[f]$ via (4.3), the Nyquist modes with $j_1 = M_1/2$ or $j_2 = M_2/2$ are set to zero, which ensures that the 'c2r' transform reconstructs real-valued functions $\tilde{\partial}_\alpha \tilde{f}$ and $H[\tilde{f}]$ from their Fourier modes. Further details on this pseudo-spectral representation are given in [84] in the context of timestepping the dynamic equations (2.78).

This pseudo-spectral representation of quasi-periodic functions can be generalized to functions with quasi-periods larger than two. In this case, one could still use the 'r2c' and 'c2r' routines in the FFTW library where the function is represented by a d-dimensional array of Fourier coefficients:

$$\tilde{f}_{m_1,m_2,\cdots,m_d} = \sum_{j_1=0}^{M_1-1} \cdots \sum_{j_d=0}^{M_d-1} \hat{f}_{j_1,j_2,\cdots,j_d} e^{2\pi i j_d m_d/M_d} \cdots e^{2\pi i j_1 m_1/M_1}, \tag{4.6}$$

where $\tilde{f}_{m_1,m_2,\cdots,m_d} = \tilde{f}(2\pi m_1/M_1, \ldots, 2\pi m_d/M_d)$ is the value of $\tilde{f}$ evaluated on a uniform $M_1 \times M_2 \times \cdots \times M_d$ grid on $\mathbb{T}^d$.

In [82], an overdetermined shooting algorithm based on the Levenberg-Marquardt method [65] was proposed for computing standing water waves accurately and efficiently. Here we adapt this method to compute quasi-periodic traveling waves instead of standing waves. We first formulate the problem in a nonlinear least-squares framework. Recall that we introduce the function $\mathcal{R}$ in (3.8), which depends on τ, c^2 (which we denote as b), $\tilde{\eta}$ and formulate the governing of quasi-periodic traveling waves as $\mathcal{R}[\tau, b, \tilde{\eta}] = 0$. In computation, we refer to $\mathcal{R}$ as the residue function and consider τ, b and the Fourier modes of $\tilde{\eta}$ as unknowns. We also define the objective function in terms of $\mathcal{R}$

$$\mathcal{F}[\tau, b, \hat{\eta}] := \frac{1}{8\pi^2} \int_{\mathbb{T}^2} \mathcal{R}^2[\tau, b, \hat{\eta}] \, d\alpha_1 \, d\alpha_2. \tag{4.7}$$

Note that solving (3.5) is equivalent to finding a zero of the objective function $\mathcal{F}[\tau, b, \hat{\eta}]$. The parameter k in (4.1) is taken to be a fixed, irrational number when searching for zeros of $\mathcal{F}$.

In the numerical computation, we truncate the problem to finite dimensions by varying only the leading Fourier modes $\hat{\eta}_{j_1,j_2}$ with $|j_1| \le N_1$ and $|j_2| \le N_2$. We evaluate the residual $\mathcal{R}$ (and compute the Fourier transforms) on an $M_1 \times M_2$ grid, where $M_i \ge 2N_i + 2$. The resulting nonlinear least squares problem is overdetermined because we zero-pad the Fourier modes $\hat{\eta}_{j_1,j_2}$ when $|j_1|$ or $|j_2|$ is larger than N_1 or N_2, respectively. Assuming the $\hat{\eta}_{j_1,j_2}$ are real (i.e. that η is even) also reduces the number of unknowns relative to the

number of equations, which are enumerated by the $M_1 M_2$ gridpoints without exploiting symmetry. Guided by the linear theory of Section 3.3, we fix the two base Fourier modes $\hat{\eta}_{1,0}$ and $\hat{\eta}_{0,1}$ at nonzero amplitudes, chosen independently, and minimize $\mathcal{F}$ over the remaining unknowns via the Levenberg-Marquardt algorithm.

It might seem more natural to prescribe τ and $\hat{\eta}_{1,0}$ and solve for $\hat{\eta}_{0,1}$ along with $b = c^2$ and the other unknown Fourier modes of η. However, since $\tau = \tau_{\text{lin}} = g/k$ is a constant within the linear approximation, deviation of τ from τ_{lin} is a higher-order nonlinear effect. This will be confirmed in Figure 4.4 of Section 4.1.1.2 below. As a result, τ is a poor choice for a continuation parameter near the trivial solution in the same way that solving $x^2 - y^2 = (\tau - \tau_{\text{lin}})$ for $x(\tau, y)$ or $y(\tau, x)$ leads to problems of existence, uniqueness, and sensitive dependence on τ near τ_{lin}. Beyond the linear regime, one can choose any two parameters among τ, b and the Fourier modes $\hat{\eta}_{j_1,j_2}$ to use as continuation parameters. How well they work will depend on the invertibility and condition number of the Fréchet derivative of $\mathcal{R}$ with respect to the remaining variables, using the implicit function theorem. We also note that the existence of time quasi-periodic water waves has only been established rigorously when τ belongs to a Cantor-like set [13, 16, 17]. It is possible that small divisors [17, 51, 68] and "near resonances" in the quasi-periodic traveling wave problem will prevent these solutions from existing in smooth families.

The Levenberg-Marquardt solver requires a linear ordering of the unknowns. We enumerate the $\hat{\eta}_{j_1,j_2}$ so that lower-frequency modes appear first. As the "shell index" s ranges from 1 to $\max(N_1, N_2)$, we enumerate all the index pairs (j_1, j_2) with $\max(|j_1|, |j_2|) = s$ before increasing s. Within shell s, we proceed clockwise, along straight lines through the lattice, from $(0, s)$ to (s, s) to $(s, -s)$ to $(1, -s)$. The other Fourier modes are known from (3.12). If $N_1 \neq N_2$, we omit (j_1, j_2) in the enumeration if $j_1 > N_1$ or $j_2 > N_2$. The total number of modes $\hat{\eta}_{j_1,j_2}$ indexed in this way is

$$N_{\text{tot}} = N_1(2N_2 + 1) + N_2. \tag{4.8}$$

We replace $\hat{\eta}_{1,0}$ by τ and $\hat{\eta}_{0,1}$ by b in the list of unknowns to avoid additional shuffling of the variables when the prescribed base modes are removed from the list. Eventually there are N_{tot} parameters to compute, shown here for the case that $N_2 \geq N_1 \geq 2$:

$$p_1 = \tau, \quad p_2 = \hat{\eta}_{1,1}, \quad p_3 = b, \quad p_4 = \hat{\eta}_{1,-1}, \quad p_5 = \hat{\eta}_{0,2} \ , \ \dots \ , \ p_{N_{\text{tot}}} = \hat{\eta}_{1,-N_2}. \tag{4.9}$$

Re-ordering the arguments of $\mathcal{R}$ and $\mathcal{F}$, our goal is to find $\boldsymbol{p}$ given $\hat{\eta}_{1,0}$ and $\hat{\eta}_{0,1}$ such that $\mathcal{R}[\boldsymbol{p}; \hat{\eta}_{1,0}, \hat{\eta}_{0,1}] = 0$ and $\mathcal{F}[\boldsymbol{p}; \hat{\eta}_{1,0}, \hat{\eta}_{0,1}] = 0$. The objective function $\mathcal{F}$ is evaluated numerically by the trapezoidal rule approximation over $\mathbb{T}^2$, which is spectrally accurate:

$$f(\boldsymbol{p}) = \frac{1}{2} r(\boldsymbol{p})^T r(\boldsymbol{p}) \approx \mathcal{F}\left[\boldsymbol{p}; \hat{\eta}_{1,0}, \hat{\eta}_{0,1}\right],$$
$$r_m(\boldsymbol{p}) = \frac{\mathcal{R}\left[\boldsymbol{p}; \hat{\eta}_{1,0}, \hat{\eta}_{0,1}\right](\alpha_{m_1}, \alpha_{m_2})}{\sqrt{M_1 M_2}}, \qquad \begin{pmatrix} m = 1 + m_1 + M_1 m_2 \\ \alpha_{m_i} = 2\pi m_i / M_i \end{pmatrix}, \quad 0 \leq m_i < M_i. \tag{4.10}$$

The parameters p_j are chosen to minimize $f(\boldsymbol{p})$ using the Levenberg-Marquardt method [65, 82]. The method requires a Jacobian matrix $\partial r_m/\partial p_j$, which we compute by solving the variational equations given in (3.38). We then have $\frac{\partial r_m}{\partial p_j} = \delta\mathcal{R}(\alpha_{m_1}, \alpha_{m_2})/\sqrt{M_1 M_2}$, where $m = 1 + m_1 + M_1 m_2$ and the jth column of the Jacobian corresponds to setting the perturbation $\delta\tau$, δb or $\delta\hat{\eta}_{j_1,j_2}$ corresponding to p_j in (4.32) to 1 and the others to 0.

Like Newton's method, the Levenberg-Marquardt method generates a sequence of approximate solutions $\boldsymbol{p}^{(0)}$, $\boldsymbol{p}^{(1)}$, etc., which terminate when the residual drops below the desired tolerance or fails to decrease sufficiently. If $\max(|\hat{\eta}_{1,0}|, |\hat{\eta}_{0,1}|) \le 0.01$, we find that the solution of the linearized problem serves as a good initial guess:

$$\begin{aligned} \tilde{\eta}^{(0)}(\alpha_1, \alpha_2) &= \hat{\eta}_{1,0}(e^{i\alpha_1} + e^{-i\alpha_1}) + \hat{\eta}_{0,1}(e^{i\alpha_2} + e^{-i\alpha_2}), \\ \tau^{(0)} = \tau_{\text{lin}} &= g/k, \qquad b^{(0)} = c_{\text{lin}}^2 = g + g/k. \end{aligned} \tag{4.11}$$

We compute larger-amplitude solutions beyond the applicability of linear theory using numerical continuation to explore one-dimensional slices (or paths) through the two-dimensional family of quasi-periodic traveling waves holding either the ratio $\gamma = \hat{\eta}_{1,0}/\hat{\eta}_{0,1}$ fixed or one of the modes $\hat{\eta}_{1,0}$, $\hat{\eta}_{0,1}$ fixed. We find that linear extrapolation from the previous two solutions on a path works well as the starting guess for the next Levenberg-Marquardt solve. Details of our Levenberg-Marquardt implementation, including stopping criteria and a strategy for delaying the re-computation of the Jacobian, are given in [82].

4.1.1.2 Numerical Results

We now present a detailed numerical study of solutions of (3.5) with $k = 1/\sqrt{2}$ and $g = 1$ on three continuation paths corresponding to $\gamma \in \{5, 1, 0.2\}$, where $\gamma = \hat{\eta}_{1,0}/\hat{\eta}_{0,1}$ is the amplitude ratio of the prescribed base modes. In each case, we vary the larger of $\hat{\eta}_{1,0}$ and $\hat{\eta}_{0,1}$ from 0.001 to 0.01 in increments of 0.001. The initial guess for the first two solutions on each path are obtained using the linear approximation (4.11), which by (4.32) corresponds to

$$p_1^{(0)} = \tau^{(0)} = \sqrt{2}, \qquad p_3^{(0)} = b^{(0)} = 1 + \sqrt{2}, \qquad p_j^{(0)} = 0, \quad j \notin \{1, 3\}. \tag{4.12}$$

As noted already, the amplitudes $\hat{\eta}_{1,0}$ and $\hat{\eta}_{0,1}$ are prescribed — they are not included among the unknowns. The initial guess for the remaining 8 solutions on each continuation path are obtained from linear extrapolation from the previous two computed solutions. In all cases, we use $M = 60$ for the grid size and $N = 24$ for the Fourier cutoff in each dimension, where we drop the subscripts when $M_1 = M_2$ and $N_1 = N_2$. The nonlinear least-squares problem involves $M^2 = 3600$ equations in $N_{\text{tot}} = 1200$ unknowns.

Figure 4.1 shows the initial conditions η and φ for the last solution on each continuation path (with $\max\{\hat{\eta}_{1,0}, \hat{\eta}_{0,1}\} = 0.01$). Panels (a), (b) and (c) correspond to $\gamma = 5$, 1, and 0.2, respectively. The solution in all three cases is quasi-periodic, i.e. η and φ never exactly

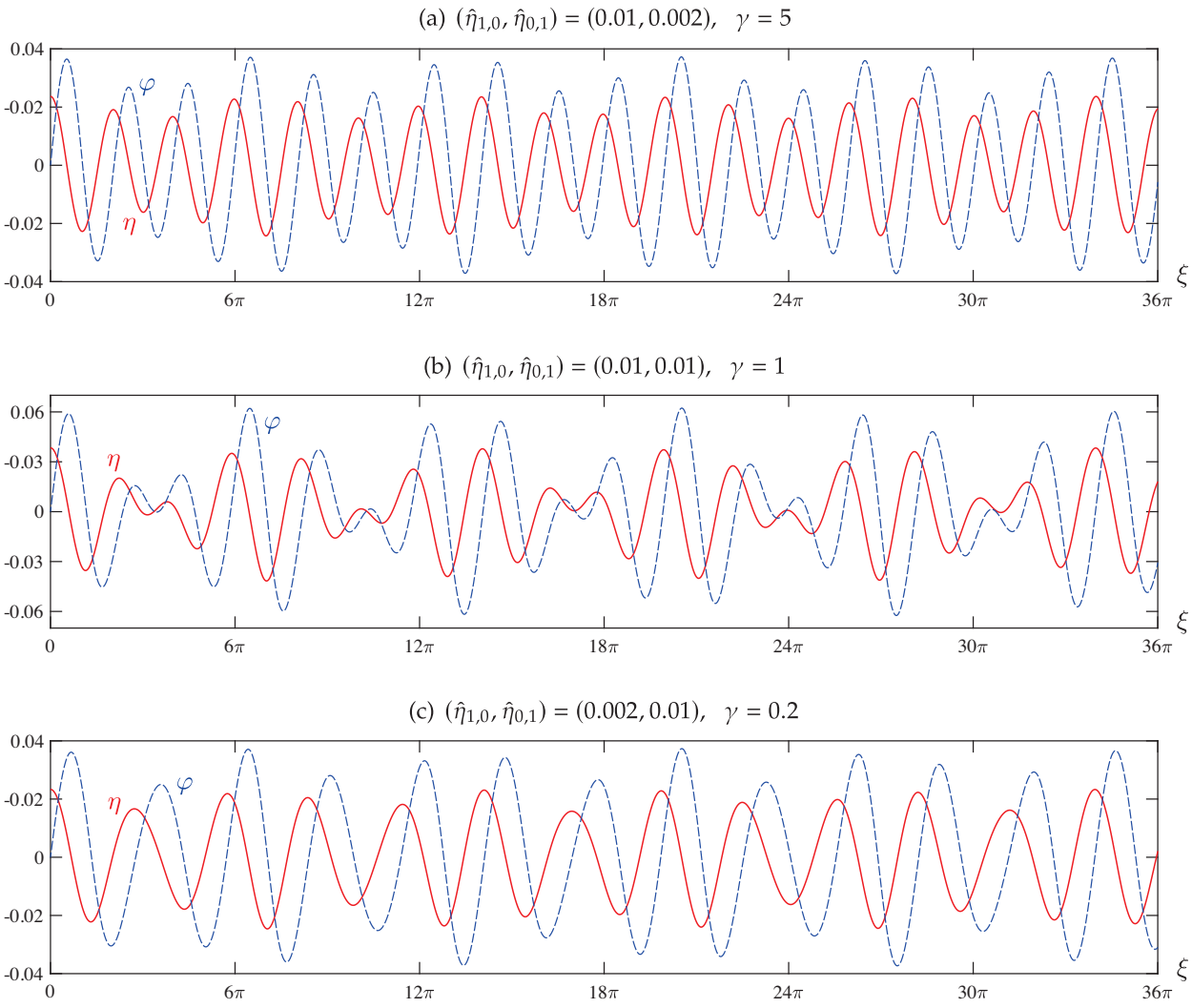

Figure 4.1: Spatially quasi-periodic traveling solutions in the lab frame at $t = 0$. The wave height $\eta(\alpha)$ (solid red line) and velocity potential $\varphi(\alpha)$ (dashed blue line) are plotted parametrically against $\xi(\alpha)$ to show the wave in physical space.

repeat themselves; we plot the solution from $x = 0$ to $x = 36\pi$ as a representative snapshot. For these three solutions, the objective function f in (4.10), which is a squared error, was minimized to 6.05×10^{-28}, 9.28×10^{-28} and 4.25×10^{-28}, respectively, with similar or smaller values for lower-amplitude solutions on each path. For each of the 30 solutions computed on these paths, only one Jacobian evaluation and 3–5 f evaluations were needed to achieve roundoff-error accuracy. In our computations, η and φ are represented by $\tilde{\eta}(\alpha_1, \alpha_2)$ and $\tilde{\varphi}(\alpha_1, \alpha_2)$, which are defined on the torus $\mathbb{T}^2$. In Figure 4.2, we show contour plots of $\tilde{\eta}(\alpha_1, \alpha_2)$ and $\tilde{\varphi}(\alpha_1, \alpha_2)$ corresponding to the final solution on each path. Following the dashed lines through $\mathbb{T}^2$ in Figure 4.2 leads to the plots in Figure 4.1. By construction in (3.12), $\tilde{\eta}(-\boldsymbol{\alpha}) = \tilde{\eta}(\boldsymbol{\alpha})$ while $\tilde{\varphi}(-\boldsymbol{\alpha}) = -\tilde{\varphi}(\boldsymbol{\alpha})$.

The amplitude ratio, $\gamma := \hat{\eta}_{1,0}/\hat{\eta}_{0,1}$, determines the bulk shape of the solution. If $\gamma \gg 1$, the component wave with wave number 1 will be dominant; if $\gamma \ll 1$, the component wave with wave number $k = 1/\sqrt{2}$ will be dominant; and if γ is close to 1, both waves together will be dominant over higher-frequency Fourier modes (at least in the regime we study here). This is demonstrated with $\gamma = 5$, 1 and 0.2 in panels (a), (b) and (c) of Figure 4.1. Panels (a) and (c) show a clear dominant mode with visible variations in the amplitude. The oscillations are faster in panel (a) than in (c) since $1 > k \approx 0.707$. By contrast, in panel (b), there is no single dominant wavelength.

This can also be understood from the contour plots of Figure 4.2. In case (a), $\gamma \gg 1$ and the contour lines of $\tilde{\eta}$ and $\tilde{\varphi}$ are perturbations of sinusoidal waves depending only on α_1. The unperturbed waves would have vertical contour lines. The α_2-dependence of the perturbation causes local extrema to form at the crest and trough. As a result, the contour lines join to form closed curves that are elongated vertically since the dominant variation is in the α_1 direction. Case (c) is similar, but the contour lines are elongated horizontally since the dominant variation is in the α_2 direction. Following the dashed lines in Figure 4.2, a cycle of α_1 is completed before a cycle of α_2 (since $k < 1$). In case (a), a cycle of α_1 traverses the dominant variation of $\tilde{\eta}$ and $\tilde{\varphi}$ on the torus, whereas in case (c), this is true of α_2. So the waves in Figure 4.1 appear to oscillate faster in case (a) than case (c). In the intermediate case (b) with $\gamma = 1$, the contour lines of the crests and troughs are nearly circular, but not perfectly round. The amplitude of the waves in Figure 4.1 are largest when the dashed lines in Figure 4.2 pass near the extrema of $\tilde{\eta}$ and $\tilde{\varphi}$, and are smallest when the dashed lines pass near the zero level sets of $\tilde{\eta}$ and $\tilde{\varphi}$.

Next we examine the behavior of the Fourier modes that make up these solutions. Figure 4.3 shows two-dimensional plots of the Fourier modes $\hat{\eta}_{j_1,j_2}$ for the 3 cases above, with $\gamma \in \{5, 1, 0.2\}$ and $\max\{\hat{\eta}_{1,0}, \hat{\eta}_{0,1}\} = 0.01$. Only the prescribed modes and the modes that were optimized by the solver (see (4.32)) are plotted, which have indices in the range $0 \le j_1 \le N$ and $-N \le j_2 \le N$, excluding $j_2 \le 0$ when $j_1 = 0$. The other modes are determined by the symmetry of (3.12) and by zero-padding $\hat{\eta}_{j_1,j_2} = 0$ if $N < j_1 \le M/2$ or $N < |j_2| \le M/2$. We used $N = 24$ and $M = 60$ in all 3 calculations. One can see that the fixed Fourier modes $\hat{\eta}_{1,0}$ and $\hat{\eta}_{0,1}$ are the two highest-amplitude modes in all three cases. In this sense, our solutions of the nonlinear problem (3.5) are small-amplitude perturbations

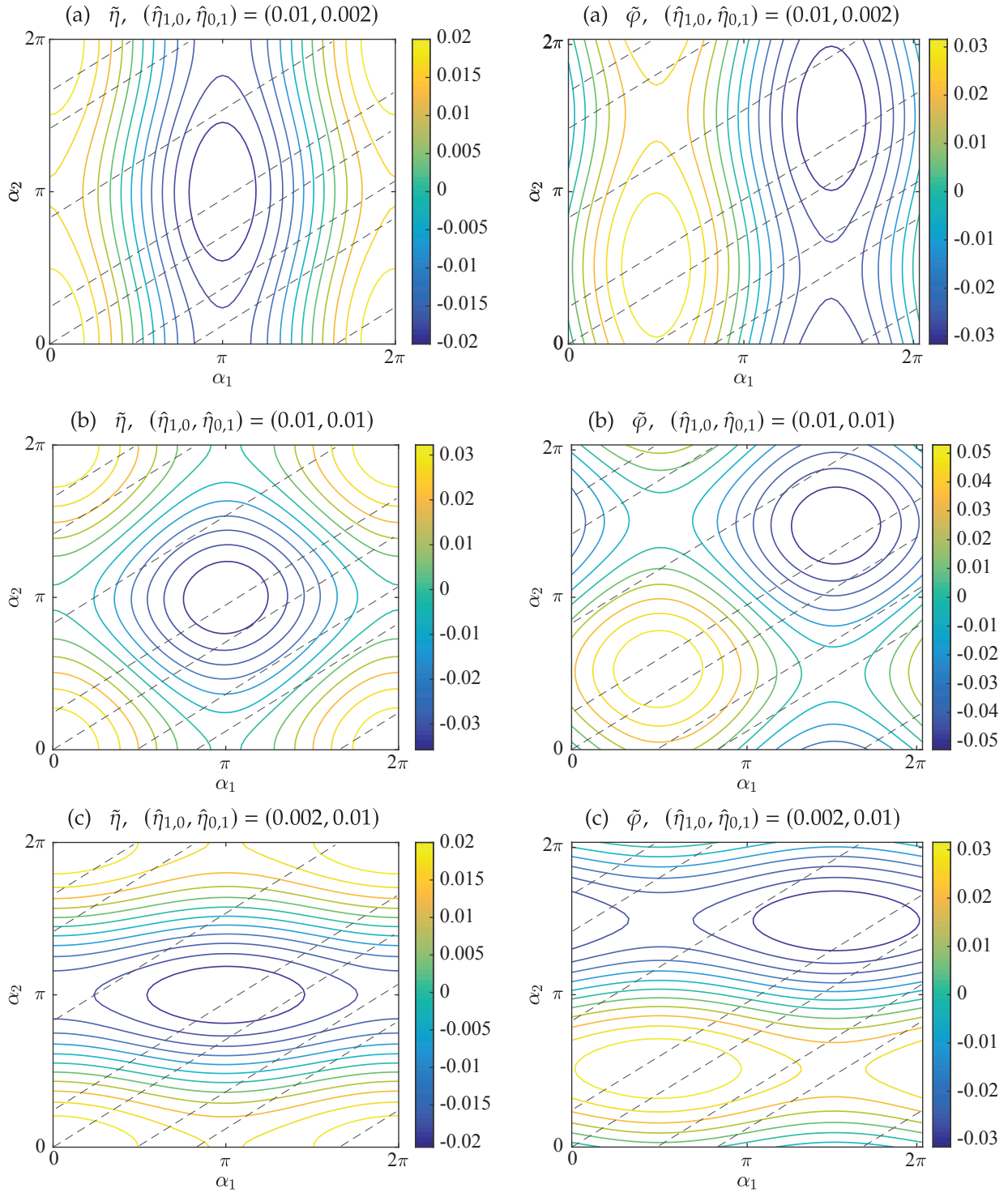

Figure 4.2: Contour plots of $\tilde{\eta}$ and $\tilde{\varphi}$ on $\mathbb{T}^2$. The dashed lines show $(\alpha, k\alpha)$ and its periodic images with $0 \leq \alpha \leq 10\pi$ and $k = 1/\sqrt{2}$. Evaluating $\tilde{\eta}$ and $\tilde{\varphi}$ at these points gives η and φ in (3.11) and (2.65), which were plotted in Figure 4.1.

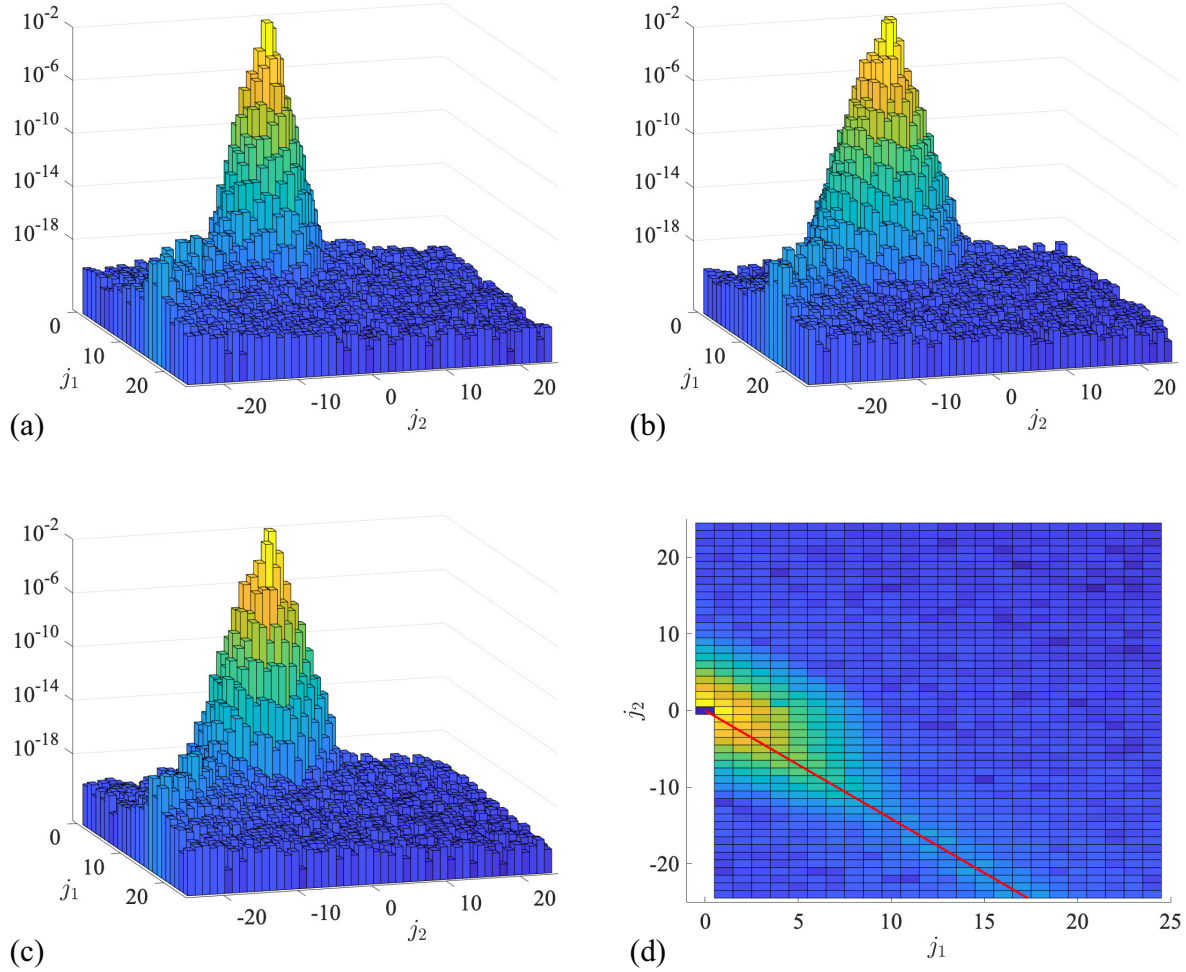

Figure 4.3: Two-dimensional Fourier modes of $\tilde{\eta}$ for the $k = 1/\sqrt{2}$ solutions plotted in Figures 4.1 and 4.2. (a) $\gamma = 5$. (b,d) $\gamma = 1$. (c) $\gamma = 0.2$. In all three cases, the modes decay visibly slower along the line $j_1 + j_2 k = 0$, indicating the presence of resonant mode interactions.

of the solutions (4.11) of the linearized problem. However, in the plots of Figure 4.3, there are many active Fourier modes other than the four modes $e^{\pm i\alpha_1}$, $e^{\pm i\alpha_2}$ from linear theory. In this sense, these solutions have left the linear regime. Carrying out a weakly nonlinear Stokes expansion to high enough order to accurately predict all these modes would be difficult due to the two-dimensional array of unknown Fourier modes, which would complicate the analysis of the periodic Wilton ripple problem [2, 5, 73, 75]. Overturning waves that are well outside of the linear regime will be computed in Section 4.1.2.

In panels (a), (b) and (c) of Figure 4.3, the modes appear to decay more slowly in

one direction than in other directions. This is seen more clearly when viewed from above, as shown in panel (d) for the case of $\gamma = 1$. (The other two cases are similar). The direction along which the modes decay less rapidly appears to coincide with the line $\{(j_1, j_2) \ : \ j_1 + j_2 k = 0\}$, which is plotted in red. A partial explanation is that when $j_1 + j_2 k$ is close to zero, the corresponding modes $e^{i(j_1+j_2 k)\alpha}$ in the expansion of $\eta(\alpha)$ in (3.11) have very long wavelengths. Slowly varying perturbations lead to small changes in the residual of the water wave equations, so these modes are not strongly controlled by the governing equations (3.5). We believe this would lead to a small divisor problem that would complicate a rigorous proof of existence of quasi-periodic traveling water waves. Similar small divisor problems arise in proving the existence of standing water waves [51,68], 3D traveling gravity waves [50], and 2D time quasi-periodic gravity-capillary waves [13,16,17], where small divisors are tackled using a Nash-Moser iterative scheme.

Next we show that τ and c depend nonlinearly on the amplitude of the Fourier modes $\hat{\eta}_{1,0}$ and $\hat{\eta}_{0,1}$. Panels (a) and (b) of Figure 4.4 show plots of τ and c versus $\hat{\eta}_{\max} := \max(\hat{\eta}_{1,0}, \hat{\eta}_{0,1})$ for 9 values of $\gamma = \hat{\eta}_{1,0}/\hat{\eta}_{0,1}$, namely $\gamma = 0.1, 0.2, 0.5, 0.8, 1, 1.25, 2, 5, 10$. On each curve, $\hat{\eta}_{\max}$ varies from 0 to 0.01 in increments of 0.001. At small amplitudes, linear theory predicts $\tau = g/k = 1.41421$ and $c = \sqrt{g(1 + 1/k)} = 1.55377$. This is represented by the black marker at $\hat{\eta}_{\max} = 0$ in each plot. For each value of γ, the curves τ and c are seen to have zero slope at $\hat{\eta}_{\max} = 0$, and can be concave up or concave down depending on γ. This can be understood from the contour plots of panels (e) and (f). Both τ and c appear to be even functions of $\hat{\eta}_{1,0}$ and $\hat{\eta}_{0,1}$ when the other is held constant. Both plots have a saddle point at the origin, are concave down in the $\hat{\eta}_{1,0}$ direction holding $\hat{\eta}_{0,1}$ fixed, and are concave up in the $\hat{\eta}_{0,1}$ direction holding $\hat{\eta}_{1,0}$ fixed. The solid lines in the first quadrant of these plots are the slices corresponding to the values of γ plotted in panels (a) and (b). The concavity of the 1d plots depends on how these lines intersect the saddle in the 2d plots.

The contour plots of panels (e) and (f) of Figure 4.4 were made by solving (3.5) with $(\hat{\eta}_{1,0}, \hat{\eta}_{0,1})$ ranging over a uniform 26×26 grid on the square $[-0.01, 0.01] \times [-0.01, 0.01]$. Using an even number of gridpoints avoids the degenerate case where $\hat{\eta}_{1,0}$ or $\hat{\eta}_{0,1}$ is zero. At those values, the two-dimensional family of quasi-periodic solutions meets a sheet of periodic solutions where τ or c becomes a free parameter. Alternative techniques would be needed in these degenerate cases to determine the value of τ or c from which a periodic traveling wave in the nonlinear regime bifurcates to a quasi-periodic wave. In panel (g), we plot the magnitude of the Chebyshev coefficients in the expansion

$$c(\hat{\eta}_{1,0}, \hat{\eta}_{0,1}) = \sum_{m=0}^{15} \sum_{n=0}^{15} \hat{c}_{mn} T_m(100\hat{\eta}_{1,0}) T_n(100\hat{\eta}_{0,1}), \qquad -0.01 \le \hat{\eta}_{1,0}, \hat{\eta}_{0,1} \le 0.01. \tag{4.13}$$

This was done by evaluating c on a cartesian product of two 16-point Chebyshev-Lobatto grids over $[-0.01, 0.01]$ and using the one-dimensional Fast Fourier Transform in each direction to compute the Chebyshev modes. We see that the modes decay to machine

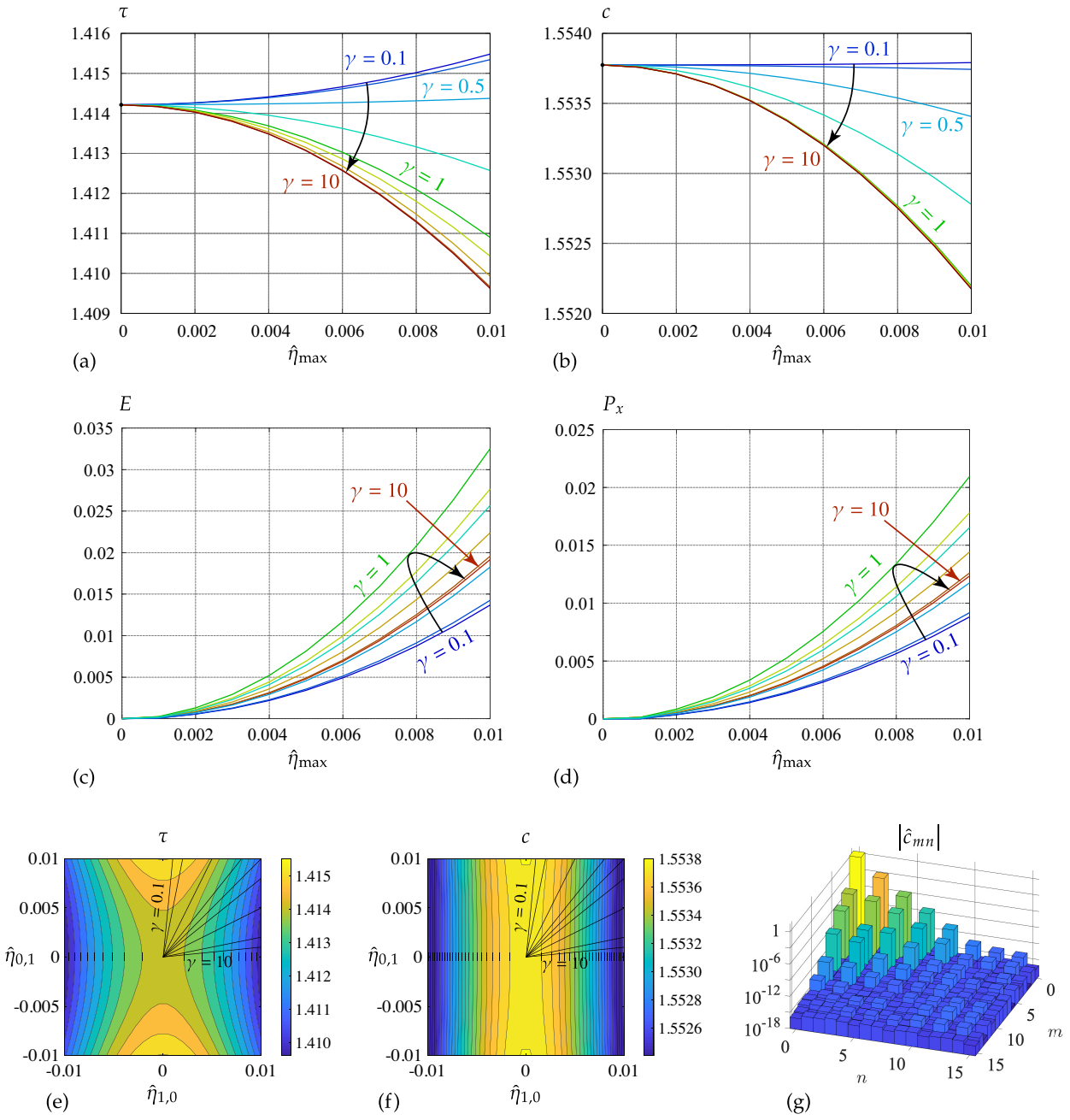

Figure 4.4: Surface tension, wave speed, energy and momentum of small-amplitude quasi-periodic water waves with $k = 1/\sqrt{2}$. (a,b,c,d) Plots of τ, c, E and P_x versus $\hat{\eta}_{\max} = \max\{\hat{\eta}_{1,0}, \hat{\eta}_{0,1}\}$ holding $\gamma = \hat{\eta}_{1,0}/\hat{\eta}_{0,1}$ fixed. The black arrow in each plot shows how the curves change as γ increases from 0.1 to 10. (e,f) Contour plots of τ and c and the rays of constant γ corresponding to (a,b). (g) Mode amplitudes of a 2d Chebyshev expansion of $c(\hat{\eta}_{1,0}, \hat{\eta}_{0,1})$ over the rectangle $-0.01 \le \hat{\eta}_{1,0}, \hat{\eta}_{0,1} \le 0.01$.

precision by the time $m + n \geq 10$ or so, and only even modes m and n are active. The plot for $|\hat{\tau}_{mn}|$ is very similar, so we omit it. These plots confirm the visual observation from the contour plots that τ and c are even functions of $\hat{\eta}_{1,0}$ and $\hat{\eta}_{0,1}$ when the other is held constant. These properties of τ and c make them unsuitable as continuation parameters near the trivial solution, as discussed in Section 4.1.1.1.

In panels (c) and (d) of Figure 4.4, we show the energy $\tilde{E}$ and momentum $\tilde{P}$ of waves in the above two-parameter family of quasi-periodic solutions. We see in Figure 4.4 that the energy and momentum of the quasi-periodic waves are positively correlated. In particular, the quasi-periodic wave family with $\gamma = 1$ possesses the largest energy and momentum when $\hat{\eta}_{\max}$ is fixed, even though it does not have the highest wave speed. Energy and momentum can both be regarded as measures of the amplitude of the wave. Unlike the wave speed, they are both zero at the flat rest state. We note that $\gamma = 1$ corresponds to maximizing both $|\hat{\eta}_{1,0}|$ and $|\hat{\eta}_{0,1}|$ to have the value $\hat{\eta}_{\max}$, and also leads to the largest amplitude oscillations in Figure 4.1. The Hamiltonian structure of the equations of motion could be useful e.g. in generalizing the time quasi-periodic results of Berti et. al. [16] to the spatially quasi-periodic setting.

4.1.2 Solutions That Bifurcate From Periodic Traveling Solutions

4.1.2.1 Numerical Methods

As a first step in computing bifurcated quasi-periodic traveling solutions, we discuss how to compute finite amplitude periodic traveling solutions. For periodic traveling solutions, since $\tilde{\eta}^{\text{per}}$ does not depend on α_2, it suffices to solve the governing equation (3.8) on $\mathbb{T}$ instead of $\mathbb{T}^2$. Similar to the numerical methods discussed in Section 4.1.1.1, we adopt a pseudo-spectrum method [83, 84] and represent a periodic function $\tilde{f}^{\text{per}}$ in the following two ways

(1) The values of $\tilde{f}^{\text{per}}$ on M equidistant points on $\mathbb{T}$

$$\tilde{f}_m = \tilde{f}^{\text{per}}(2\pi m/M), \qquad 0 \leq m \leq M, \quad M \text{ is even.} \tag{4.14}$$

(2) The truncated Fourier series of $\tilde{f}^{\text{per}}$

$$\tilde{f}^{\text{per}}(\alpha_1) = \sum_{j_1=-M/2+1}^{M/2} \hat{f}_{j_1,0} e^{ij_1\alpha_1}. \tag{4.15}$$

We apply one-dimensional real-to-complex, complex-to-real fast Fourier transforms to transform between the two representations. The derivation and the Hilbert transform of a function are performed in Fourier space; the corresponding Fourier multipliers are (ij_1) and $(-i)\,\text{sgn}(j_1)$ for $j_1 \neq M/2$. We formulate (3.8) as an overdetermined nonlinear

least-squares problem [83] and define the objective function in the periodic case as

$$\mathcal{F}[\tau, b, \tilde{\eta}^{\mathrm{per}}] = \frac{1}{4\pi^2}\int_{\mathbb{T}} \mathcal{R}^2[\tau, b, \tilde{\eta}^{\mathrm{per}}]\,\mathrm{d}\alpha_1. \tag{4.16}$$

Note that solving (3.8) is equivalent to finding solutions of $\mathcal{F} = 0$. In computation, we set $\hat{\eta}_{0,0} = 0$ and fix the values of τ and $\hat{\eta}_{1,0}$; the unknowns are b and the other Fourier coefficients of $\tilde{\eta}^{\mathrm{per}}$, which are represented by a vector $\boldsymbol{p}$

$$p_1 = b, \quad p_2 = \hat{\eta}_{2,0}, \ldots, \quad p_N = \hat{\eta}_{N,0}, \qquad N < M/2. \tag{4.17}$$

We also set the Fourier coefficients $\hat{\eta}_{j_1,0}$ to be zero for $|j_1| \geq N$ thus the problem is overdetermined. To demonstrate the dependence of the objective function on the unknowns, we express it as $\mathcal{F}[\boldsymbol{p}; \tau, \hat{\eta}_{1,0}]$. We evaluate $\mathcal{F}$ numerically by the trapezoidal rule approximation over $\mathbb{T}$, which is spectrally accurate

$$\begin{aligned} f(\boldsymbol{p}) &= \frac{1}{2}\boldsymbol{r}(\boldsymbol{p})^T\boldsymbol{r}(\boldsymbol{p}) \approx \mathcal{F}[\boldsymbol{p}; \tau, \hat{\eta}_{1,0}], \\ r_m(\boldsymbol{p}) &= \frac{1}{\sqrt{M}}\mathcal{R}[\boldsymbol{p}; \tau, \hat{\eta}_{1,0}](\alpha_m), \end{aligned} \qquad (0 \leq m \leq M-1)\,. \tag{4.18}$$

We apply the Levenberg-Marquardt method [65, 82] to search for the minimizer of $f(\boldsymbol{p})$. The method requires a Jacabian matrix $\partial r_m/\partial p_j$, which is computed by the variational equations (3.38). To obtain the branch of periodic traveling gravity-capillary waves, we fix τ or $\hat{\eta}_{1,0}$ alternatively and use the other one as the continuation parameter to compute the periodic branch, denoted $\mathfrak{q}^{\mathrm{per}}(s)$.

Next we are going to discuss how to detect quasi-periodic bifurcation points on $\mathfrak{q}^{\mathrm{per}}(s)$ and compute the corresponding bifurcation directions numerically. As discussed in Remark 3.4.4, we are interested in bifurcation points where the kernel of $D_{\tilde{\eta}}\mathcal{R}$ possesses functions of the following form

$$\delta\eta^{\mathrm{qua}}(\alpha_1, \alpha_2) = e^{i\alpha_2}\sum_{j\in\mathbb{Z}} \delta\hat{\eta}_j e^{ij\alpha_1} + c.c., \tag{4.19}$$

where the coefficient $\delta\hat{\eta}_j$ is real for $j \in \mathbb{Z}$. We introduce a Fourier basis

$$e^{i\alpha_2} + c.c., \quad e^{i(\alpha_2+j\alpha_1)} + c.c., \quad e^{i(\alpha_2-j\alpha_1)} + c.c., \qquad j = 1, 2, \ldots, N_{\mathrm{qua}}, \tag{4.20}$$

where $0 < N_{\mathrm{qua}} \leq N$. Let $q^{\mathrm{per}} = (\tau, b, \tilde{\eta}^{\mathrm{per}})$ be an arbitrary point on $\mathfrak{q}^{\mathrm{per}}(s)$, according to (3.40), we have

$$D_{\tilde{\eta}}\mathcal{R}[q^{\mathrm{per}}](e^{il(\alpha_1+\alpha_2)}) = e^{i\alpha_2}u^{(l)}(\alpha_1), \quad u^{(l)} = \sum_{j\in\mathbb{Z}} \hat{u}_j^{(l)} e^{ij\alpha_1}, \quad l = 0, \pm1, \pm2, \ldots, \pm N_{\mathrm{qua}}. \tag{4.21}$$

One can check that the Fourier coefficients of $u^{(l)}$ are real using equations (3.38), therefore

$$D_{\tilde{\eta}}\mathcal{R}[q^{\mathrm{per}}](e^{il(\alpha_1+\alpha_2)}+c.c.)=\sum_{j\in\mathbb{Z}}\hat{u}_j^{(l)}(e^{i(\alpha_2+j\alpha_1)}+c.c.),\qquad l=0,\pm1,\pm2,\ldots,\pm N_{\mathrm{qua}}. \tag{4.22}$$

We denote $D_{\tilde{\eta}}\mathcal{R}[q^{\mathrm{per}}]$ under the Fourier basis (4.20) by the matrix $\mathcal{J}^{\mathrm{qua}}[q^{\mathrm{per}}]$; according to (4.22), we have

$$\mathcal{J}^{\mathrm{qua}}[q^{\mathrm{per}}]=\begin{pmatrix}\hat{u}_0^{(0)} & \hat{u}_0^{(1)} & \hat{u}_0^{(-1)} & \cdots & \hat{u}_0^{(N_{\mathrm{qua}})} & \hat{u}_0^{(-N_{\mathrm{qua}})}\\ \hat{u}_1^{(0)} & \hat{u}_1^{(1)} & \hat{u}_1^{(-1)} & \cdots & \hat{u}_1^{(N_{\mathrm{qua}})} & \hat{u}_1^{(-N_{\mathrm{qua}})}\\ \hat{u}_{-1}^{(0)} & \hat{u}_{-1}^{(1)} & \hat{u}_{-1}^{(-1)} & \cdots & \hat{u}_{-1}^{(N_{\mathrm{qua}})} & \hat{u}_{-1}^{(-N_{\mathrm{qua}})}\\ \vdots & \vdots & \vdots & & \vdots & \vdots\\ \hat{u}_{N_{\mathrm{qua}}}^{(0)} & \hat{u}_{N_{\mathrm{qua}}}^{(1)} & \hat{u}_{N_{\mathrm{qua}}}^{(-1)} & \cdots & \hat{u}_{N_{\mathrm{qua}}}^{(N_{\mathrm{qua}})} & \hat{u}_{N_{\mathrm{qua}}}^{(-N_{\mathrm{qua}})}\\ \hat{u}_{-N_{\mathrm{qua}}}^{(0)} & \hat{u}_{-N_{\mathrm{qua}}}^{(1)} & \hat{u}_{-N_{\mathrm{qua}}}^{(-1)} & \cdots & \hat{u}_{-N_{\mathrm{qua}}}^{(N_{\mathrm{qua}})} & \hat{u}_{-N_{\mathrm{qua}}}^{(-N_{\mathrm{qua}})}\end{pmatrix}. \tag{4.23}$$

The computation of $\mathcal{J}^{\mathrm{qua}}$ involves computing $u^{(l)}$ by (4.21) . Since each term in (4.21) can be written in the form $e^{i\alpha_2}\tilde{f}^{\mathrm{per}}(\alpha_1)$, we employ the idea of Fourier-Bloch decomposition [31] and compute $u^{(l)}$ by

$$\begin{aligned}
u^{(l)}&=-\frac{1}{2(\tilde{J}^{\mathrm{per}})^2}bJ^{(l)}+g\eta^{(l)}-\tau\kappa^{(l)},\\
\eta^{(l)}&=e^{il\alpha_1},\qquad J^{(l)}=2\left\{\partial_{\alpha_1}\tilde{\xi}^{\mathrm{per}}(|1+l|\eta^{(l)})+\partial_{\alpha_1}\tilde{\eta}^{\mathrm{per}}(i(1+l)\eta^{(l)})\right\},\\
\kappa^{(l)}&=-\frac{3}{2\tilde{J}^{\mathrm{per}}}\tilde{\kappa}^{\mathrm{per}}J^{(l)}+\frac{1}{(\tilde{J}^{\mathrm{per}})^{3/2}}\left\{(\partial_{\alpha_1}^2\tilde{\eta}^{\mathrm{per}})(|1+l|\eta^{(l)})+\partial_{\alpha_1}\tilde{\xi}^{\mathrm{per}}(-(1+l)^2\eta^{(l)})\right.\\
&\quad\left.-(\partial_{\alpha_1}^2\tilde{\xi}^{\mathrm{per}})(i(1+l)\eta^{(l)})-(\partial_{\alpha_1}\tilde{\eta}^{\mathrm{per}})((i)\,\mathrm{sgn}(1+l)(1+l)^2\eta^{(l)})\right\}.
\end{aligned} \tag{4.24}$$

Different from (4.21), the above equations are posed on $\mathbb{T}$ instead of $\mathbb{T}^2$. To obtain the l-th column of $\mathcal{J}^{\mathrm{qua}}$, we compute the Fourier series of $u^{(l)}$ using a one-dimensional complex-to-complex fast Fourier transform since $u^{(l)}$ is a complex-valued function in general.

As discussed in Section 3.4, we detect the quasi-periodic bifurcation point on $\mathfrak{q}^{\mathrm{per}}(s)$ by tracking the sign of $\det\mathcal{J}^{\mathrm{qua}}[\mathfrak{q}^{\mathrm{per}}(s)]$; the determinant of $\mathcal{J}$ is computed through QR factorization with column pivoting in the LAPACK routine

$$\mathcal{J}^{\mathrm{qua}}=QRP^T, \tag{4.25}$$

where Q is an orthogonal matrix, R is an upper triangular matrix and P is a permutation matrix, which is chosen so that

$$|R_{11}|\geq|R_{22}|\geq\ldots\geq|R_{nn}|,\qquad n=2N_{\mathrm{qua}}+1. \tag{4.26}$$

The sign of $\det \mathcal{J}^{\text{qua}}$ is

$$\operatorname{sgn}(\det \mathcal{J}^{\text{qua}}) = \operatorname{sgn}(\det Q)\operatorname{sgn}(\det P)\Pi_{j=1}^{2N_{\text{qua}}+1}\operatorname{sgn}(R_{jj}). \tag{4.27}$$

In practice, instead of a point, we obtain an interval $[s_1, s_2]$ such that

$$\det \mathcal{J}^{\text{qua}}[\mathfrak{q}^{\text{per}}(s_1)] \det \mathcal{J}^{\text{qua}}[\mathfrak{q}^{\text{per}}(s_2)] \le 0. \tag{4.28}$$

The bifurcation point lies between $\mathfrak{q}^{\text{per}}(s_1)$ and $\mathfrak{q}^{\text{per}}(s_2)$ on the curve $\mathfrak{q}^{\text{per}}(s)$. We apply a bisection method to compute such intervals and terminate when the length of the interval is around 10^{-15}; any point inside of this interval can be chosen as a bifurcation point within round-off errors. To better demonstrate the rank deficiency of $\mathcal{J}^{\text{qua}}$ at the bifurcation point, we compute the following function simultaneously when we compute the sign of $\det \mathcal{J}^{\text{qua}}$ along $\mathfrak{q}^{\text{per}}(s)$

$$\chi[\mathfrak{q}^{\text{per}}(s)] = \operatorname{sgn}(\det \mathcal{J}^{\text{qua}}[\mathfrak{q}^{\text{per}}(s)])|R_{nn}[\mathfrak{q}^{\text{per}}(s)]|, \qquad n = 2N_{\text{qua}} + 1. \tag{4.29}$$

After we obtain the bifurcation point, we use the singular value decomposition to compute the null vector of $\mathcal{J}^{\text{qua}}$, which is the bifurcation direction. We denote the quasi-periodic bifurcation point as $q^{\text{bif}} = (\tau^{\text{bif}}, b^{\text{bif}}, \tilde{\eta}^{\text{bif}})$ and the bifurcation direction as $\delta q^{\text{bif}} = (0, 0, \delta\tilde{\eta}^{\text{bif}})$; according to (4.19), we have

$$\delta\tilde{\eta}^{\text{bif}} = \sum_{j_1=-N_{\text{qua}}}^{N_{\text{qua}}} \delta\hat{\eta}^{\text{bif}}_{j_1,1} e^{i(j_1\alpha_1+\alpha_2)} + c.c.. \tag{4.30}$$

We also define $\delta\hat{\eta}^{\text{bif}}_{j_{\max},1}$ by

$$|\delta\hat{\eta}^{\text{bif}}_{j_{\max},1}| = \max_{-N_{\text{qua}}\le j_1\le N_{\text{qua}}} |\delta\hat{\eta}^{\text{bif}}_{j_1,1}|. \tag{4.31}$$

We adopt the numerical methods discussed in Section 4.1.1.1 to compute quasi-periodic traveling solutions. To switch from the periodic branch to the quasi-periodic branch, we use $q^{\text{bif}} + \epsilon\delta q^{\text{bif}}$ (or $q^{\text{bif}} - \epsilon\delta q^{\text{bif}}$) as an initial guess to compute the first quasi-periodic solution on the branch, where ϵ is usually chosen to be 10^{-5} or 10^{-4}. In the minimization of the objective function $\mathcal{F}$, we fix $\tau = \tau^{\text{bif}}$ and $\hat{\eta}_{j_{\max},1} = \epsilon\delta\hat{\eta}^{\text{bif}}_{j_{\max},1}$. Hence the unknowns of the problem are b and the leading Fourier coefficients of $\tilde{\eta}$: $\hat{\eta}_{j_1,j_2}$ for $|j_1| \le N_1$, $|j_2| \le N_2$, except $\hat{\eta}_{0,0}$ and $\hat{\eta}_{j_{\max},1}$. The unknowns are stored in a vector $\boldsymbol{p}$; for example, if $j_{\max} = 0$, the entries of $\boldsymbol{p}$ are

$$p_1 = b, \quad p_2 = \hat{\eta}_{1,1}, \quad p_3 = \hat{\eta}_{1,0}, \quad p_4 = \hat{\eta}_{1,-1}, \quad p_5 = \hat{\eta}_{0,2} \ , \ \dots \ , \ p_{N_{\text{tot}}} = \hat{\eta}_{1,-N_2}, \tag{4.32}$$

where $N_{\text{tot}} = N_1(2N_2 + 1) + N_2$. We also require that $N_1 > N$ to ensure that we do not lose any accuracy in the α_1 direction when we switch from the periodic branch to the

quasi-periodic branch. In summary, our goal is to find $\boldsymbol{p}$ given τ^{bif} and $\hat{\eta}_{j_{\max},1}$ such that $\mathcal{F}[\boldsymbol{p}; \tau^{\text{bif}}, \hat{\eta}_{j_{\max},1}] = 0$. When computing the whole bifurcation branch, we fix $\tau = \tau^{\text{bif}}$ and use $\hat{\eta}_{j_{\max},1}$ as a continuation parameter, hence we obtain a one-parameter family of solutions. We remark that this is different from Section 4.1.1.1, where we use $\hat{\eta}_{1,0}$ and $\hat{\eta}_{0,1}$ as bifurcation parameters to compute quasi-periodic traveling solutions that bifurcate from the zero solution.

4.1.2.2 Numerical Results

In this section, we present numerical results of bifurcated quasi-periodic gravity-capillary waves corresponding to $k = 1/\sqrt{2}$. In particular, we find overturning quasi-periodic waves that bifurcate from periodic overturning waves. In computation, g is normalized to be 1.

For periodic gravity-capillary waves, we fix the Fourier coefficient $\hat{\eta}_{1,0}$ and use τ as the continuation parameter to compute the periodic branch $\mathfrak{q}^{\text{per}}(s)$; we choose $N = 50, M = 150, N_{\text{qua}} = 45$ in computation thus the size of the matrix $\mathcal{J}^{\text{qua}}$ is 91×91. We start by examining the periodic solutions of small amplitudes to search for bifurcation points. We first fix $\hat{\eta}_{1,0} = 0.001$ and increase the value of τ from 0.1 to 10 with an increment $\Delta\tau = 0.1$ to compute the periodic path; we detect the bifurcation point by tracking the sign change of $\det \mathcal{J}^{\text{qua}}$ along the path. The method produces a bifurcation point when τ belongs to intervals $[0.2, 0.3]$, $[0.5, 0.6]$, $[0.7, 0.8]$, $[1.4, 1.5]$ and $[3.4, 3.5]$. Note that the linearization of (3.8) around the zero solution possesses the solution

$$\begin{gathered} \tilde{\eta}_{\text{lin}}(\alpha_1, \alpha_2) = 2\hat{\eta}_{1,0}\cos(\alpha_1) + 2\hat{\eta}_{0,1}\cos(\alpha_2), \\ \tau_{\text{lin}} = g/k = \sqrt{2} \approx 1.414, \qquad b_{\text{lin}} = g + g/k = 1 + \sqrt{2} \approx 2.414, \end{gathered} \tag{4.33}$$

where $\tau_{\text{lin}} \in [1.4, 1.5]$. However, our goal is to find large-amplitude quasi-periodic overturning waves, which are far beyond small perturbations of the above linear solution, hence the interval $[1.4, 1.5]$ is not applicable for us. In [3], Akers, Ambrose and Wright proved the existence of gravity perturbed Crapper waves and computed large-amplitude self-intersecting overturning waves when $\tau \geq 5$; accordingly, a larger value of τ is of our interest. We apply the bisection method described in Section 4.1.2.1 to the interval $[3.4, 3.5]$ and find a bifurcation point with $\hat{\eta}_{1,0}^{\text{bif}} = 0.001$, $\tau^{\text{bif}} \approx 3.4142$; at this bifurcation point, the objective function f is minimized to 3.39×10^{-30} and the function χ is equal to 3.25×10^{-13}. To compute bifurcation points where the periodic solution $\bar{\eta}^{\text{bif}}$ is of higher amplitude, we increase $\hat{\eta}_{1,0}$ from 0.001 to 0.791 with an increment $\Delta\hat{\eta}_{1,0} = 0.001$; we stop at $\hat{\eta}_{1,0} = 0.791$ because the solution is self-intersecting when $\hat{\eta}_{1,0} = 0.792$. We search for bifurcation points by varying the value of τ at each step; the bifurcation point obtained at the previous step is used as an initial guess to compute the bifurcation point at the next step. The panel (a) of Figure 4.5 plots the bifurcation points we obtain; as is shown in the picture, the bifurcation point with a larger $\hat{\eta}_{1,0}^{\text{bif}}$ also has a larger τ.

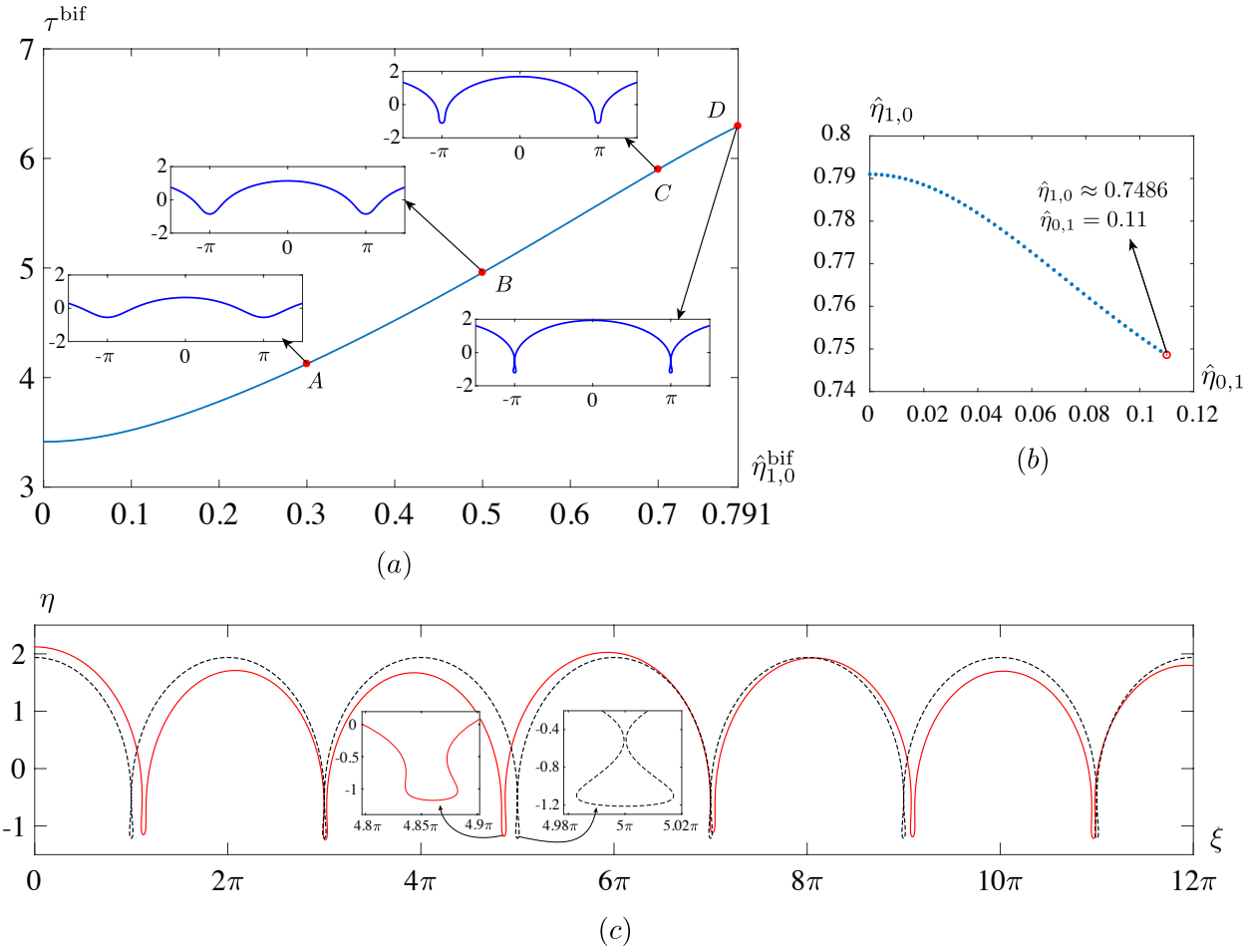

Figure 4.5: In panel (a), we plot the Fourier coefficient $\hat{\eta}_{1,0}^{\text{bif}}$ and τ^{bif} of the bifurcation point $q^{\text{bif}} = (\tau^{\text{bif}}, b^{\text{bif}}, \tilde{\eta}^{\text{bif}})$. For point A, $\hat{\eta}_{1,0}^{\text{bif}} = 0.3$, $\tau^{\text{bif}} \approx 4.1248$; For point B, $\hat{\eta}_{1,0}^{\text{bif}} = 0.5$, $\tau^{\text{bif}} \approx 4.9580$; For point C, $\hat{\eta}_{1,0}^{\text{bif}} = 0.7$, $\tau^{\text{bif}} \approx 5.9000$; For point D, $\hat{\eta}_{1,0}^{\text{bif}} = 0.791$, $\tau^{\text{bif}} \approx 6.2947$. In panel (b), we plot the Fourier coefficient $\hat{\eta}_{1,0}$ and $\hat{\eta}_{0,1}$ of the quasi-periodic solutions that bifurcate from the periodic solution at point D. In panel (c), we plot the surface elevation η of two traveling solutions: the black dashed line corresponds to the periodic solution at point D; the red line corresponds to the quasi-periodic solution that bifurcates from this periodic solution, which is represented by the red point in panel (b).

We obtain a quasi-periodic bifurcation point $q^{\text{bif}} = (\tau^{\text{bif}}, b^{\text{bif}}, \tilde{\eta}^{\text{bif}})$ with $\hat{\eta}_{1,0}^{\text{bif}} = 0.791$, $\tau \approx 6.2986$; as shown in the panel (a) of Figure 4.5, the corresponding periodic solution $\tilde{\eta}^{\text{bif}}$ is a large-amplitude overturning wave. At this bifurcation point, the objective function is minimized to 4.24×10^{-27} and χ is equal to 1.43×10^{-15}. We compute the singular value decomposition of $\mathcal{J}^{\text{qua}}$ at this point and obtain its zero eigenvector, which is also

the bifurcation direction, denoted $\delta\eta^{\text{bif}}$. In computation, we choose $N_1 = N_2 = 80$, $M_1 = M_2 = 180$ and use $q^{\text{bif}} + 10^{-5}(0, 0, \delta\tilde{\eta}^{\text{bif}})$ to jump from the periodic branch to the quasi-periodic branch. We find out that for $\delta\eta^{\text{bif}}$, the Fourier coefficient with the largest norm is $\delta\hat{\eta}^{\text{bif}}_{0,1}$. Hence we use $\hat{\eta}_{0,1}$ as a continuation parameter and compute the quasi-periodic branch by increasing its norm; τ is fixed to be τ^{bif} in computation. We are able to compute the quasi-periodic continuation path until $\hat{\eta}_{1,0}$ reaches 0.11. The corresponding solution is represented by the red point in the panel (b) of Figure 4.5; for this solution, $\hat{\eta}_{1,0} \approx 0.7486$ and the objective function f is minimized to 2.18×10^{-26}. In the panel (b) of Figure 4.5, we plot the Fourier coefficients $\hat{\eta}_{1,0}$ and $\hat{\eta}_{0,1}$ of the solutions on the quasi-periodic bifurcation branch. One can observe that $\hat{\eta}_{1,0}$ decreases as $\hat{\eta}_{0,1}$ increases. We remark that we only need to compute the quasi-periodic solutions for which $\hat{\eta}_{0,1}$ is positive because the solutions with negative $\hat{\eta}_{0,1}$ can be obtained by a spatial shift $(\alpha_1, \alpha_2) \mapsto (\alpha_1, \alpha_2 + \pi)$ as discussed in Remark 3.2.1.

In the panel (c) of Figure 4.5, we compare the surface elevation η of the periodic solution with $\hat{\eta}^{\text{bif}}_{1,0} = 0.791$ and the quasi-periodic solution that bifurcates from this periodic solution, of which $\hat{\eta}_{0,1} = 0.11$. As is shown in the picture, the peaks and troughs of the quasi-periodic solution appear in a non-periodic pattern: the peaks of the quasi-periodic solution are above the periodic solution's near $\xi = 0, 6\pi$ and are below near $\xi = 2\pi, 4\pi, 10\pi$; the troughs of the quasi-periodic solution are on the left of the periodic solutions' near $\xi = 5\pi, 11\pi$ and are on the right near $\xi = 3\pi, 7\pi, 9\pi$. We zoom into the troughs of the two solutions near $\xi = 5\pi$ and observe that the trough of the quasi-periodic solution is asymmetrical. The two zoomed in pictures show that both solutions are not self-intersecting. Moreover, the quasi-periodic solution is further from the self-intersecting wave than the periodic solution; this is because for the quasi-periodic solution, the Fourier coefficient $\hat{\eta}_{1,0}$ is approximately 0.7286, which is smaller than the one of the periodic solution.

4.2 Time Evolution of Spatially Quasi-Periodic Waves

4.2.1 Numerical Methods

We compute the time evolution of $\tilde{\eta}$ and $\tilde{\varphi}$ based on (2.79) and reconstruct the values of η and φ from corresponding tilde functions using (2.79). We adopt the same pseudo-spectral method described in Section 4.1.1.1 and represent a tilde function by its values at $M_1 \times M_2$ equidistant points on $\mathbb{T}^2$ as well as its two dimensional Fourier series. The nonlinear operations in (2.79) consist of production and division; they are computed pointwise on the grid points. The derivative and Hilbert transform are computed in Fourier space with symbols $i(j_1 + kj_2)$ and $(-i)\,\text{sgn}(j_1 + kj_2)$ for $(j_1, j_2) \in \mathbb{Z}^2$. To plot the solution, we also need to compute the antiderivative of $\tilde{f} = \tilde{\partial}_\alpha \tilde{\xi}$ to obtain $\tilde{\xi}$. This involves dividing $\hat{f}_{j_1,j_2}$ by $i(j_1 + j_2 k)$ for $(j_1, j_2) \neq (0, 0)$ and adjusting the $(0, 0)$ mode to enforce $\xi(0, t) = 0 = \tilde{\xi}(0, 0, t)$.

The evolution equations (2.78) are not stiff when the surface tension parameter is small or vanishes, but become moderately stiff for larger values of τ. We find that the 5th and 8th order explicit Runge-Kutta methods of Dormand and Prince [44] work well for smaller values of τ, and exponential time-differencing (ETD) methods [15, 25, 28, 53, 79] work well generally. This will be demonstrated in Sections 4.2.2 and 4.2.3 below. In the ETD framework, we follow the basic idea of the small-scale decomposition for removing stiffness from interfacial flows [47, 48] and write the evolution equations (2.78) in the form

$$\begin{pmatrix} \tilde{\eta}_t \\ \tilde{\varphi}_t \end{pmatrix} = L \begin{pmatrix} \tilde{\eta} \\ \tilde{\varphi} \end{pmatrix} + \mathcal{N}, \qquad L = \begin{pmatrix} 0 & H\tilde{\partial}_\alpha \\ -(gP - \tau(\tilde{\partial}_\alpha)^2) & 0 \end{pmatrix}, \tag{4.34}$$

where the projection P and the Hilbert transform H are defined in Definition 2.2.3, and

$$\mathcal{N} = \begin{pmatrix} -\tilde{\partial}_\alpha \eta H[\tilde{\chi}] - (\tilde{\partial}_\alpha \tilde{\xi} - \tilde{\partial}_\alpha \tilde{\psi}) + C_1 \tilde{\partial}_\alpha \tilde{\eta} \\ P\left[\frac{(\tilde{\partial}_\alpha)^2 \tilde{\psi} - (\tilde{\partial}_\alpha \tilde{\varphi})^2}{2\tilde{J}} - \tilde{\partial}_\alpha \tilde{\varphi} H[\tilde{\chi}] + C_1 \tilde{\partial}_\alpha \tilde{\varphi} + \tau(\kappa - (\tilde{\partial}_\alpha)^2 \eta) \right] \end{pmatrix}. \tag{4.35}$$

Note that $\mathcal{N}$ is obtained by subtracting the terms included in L from (2.78). In particular, $\tilde{\partial}_\alpha \tilde{\psi}$ in (4.35) is $-H\tilde{\partial}_\alpha \tilde{\varphi}$ from (4.34). The eigenvalues of L are $\pm i\sqrt{|j_1 + j_2 k|\big(g + \tau(j_1 + j_2 k)^2\big)}$, so the leading source of stiffness is dispersive. This 3/2 power growth rate of the eigenvalues of the leading dispersive term with respect to wave number is typical of interfacial fluid flows with surface tension [47, 48]. For stiffer problems such as the Benjamin-Ono and KdV equations, the growth rate is faster (quadratic and cubic, respectively) and it becomes essential to use a semi-implicit or exponential time-differencing scheme to avoid severe time-stepping restrictions. Here it is less critical, but still useful. Further details on how to implement (4.34) and (4.35) in the ETD framework are given in the appendix of [84].

In both the explicit Runge-Kutta and ETD methods, as explained above, the functions evolved in time are $\tilde{\eta}(\alpha_1, \alpha_2, t)$ and $\tilde{\varphi}(\alpha_1, \alpha_2, t)$, sampled on the uniform $M_1 \times M_2$ grid covering $\mathbb{T}^2$. At the end of each time step, we apply a 36th order filter [46, 47] with Fourier multiplier

$$\rho(j_1, j_2) = \begin{cases} 0, & j_1 = M_1/2 \text{ or } |j_2| = M_2/2, \\ \exp\big(-36\big[(2j_1/M_1)^{36} + (2j_2/M_2)^{36}\big]\big), & \text{otherwise.} \end{cases} \tag{4.36}$$

In all the computations reported below, we used the same number of gridpoints in the α_1 and α_2-directions, $M_1 = M_2 = M$. It is easy to check *a-posteriori* that the Fourier modes decay sufficiently (e.g. to machine precision) by the time the filter deviates appreciably from 1. If they do not, the calculation can be repeated with a larger value of M. This will be demonstrated in Section 4.2.3 below.

4.2.2 Traveling Waves

In this section, we confirm that the quasi-periodic solutions we obtain by minimizing the objective function (4.10) are indeed traveling waves under the evolution equations (2.78). This allows us to measure the accuracy of our independent codes for solving these two problems by comparing the numerical results. An interesting feature of the conformal mapping formulation arises in this comparison, namely that for most choices of C_1 in (2.78), traveling waves move at a non-uniform speed through conformal space in order to travel at constant speed in physical space. This is discussed in this section and proved in Appendix A.2.

In Figure 4.6, we plot the time evolution of $\zeta(\alpha, t) = \xi(\alpha, t) + i\eta(\alpha, t)$ in the lab frame from $t = 0$ to $t = 3$. The initial conditions, plotted with thick blue lines, are those of the traveling waves computed in Figures 4.1 and 4.2 above by minimizing the objective function (4.10). The grey curves give snapshots of the solution at uniformly sampled times with $\Delta t = 0.1$. They were computed using the 5th order explicit Runge-Kutta method described in Section 4.2.1 with a stepsize of $1/300$, so there are 30 Runge-Kutta steps between snapshots in the figure. The solutions are plotted over the representative interval $0 \le x \le 12\pi$, though they extend in both directions to $\pm\infty$ without exactly repeating. The initial condition and time evolution were computed on the torus and then sampled along the $(1, k)$ direction to extract the data for these 1D plots.

For quantitative comparison, let $\tilde{\eta}_0(\boldsymbol{\alpha})$ denote the initial condition on the torus, which is computed numerically by minimizing (4.10). We then compute $\tilde{\xi}_0 = H[\tilde{\eta}_0]$ and $\tilde{\varphi}_0 = c\tilde{\xi}_0$, which are odd functions of $\boldsymbol{\alpha} = (\alpha_1, \alpha_2) \in \mathbb{T}^2$ since $\tilde{\eta}$ is even. From Corollary A.2.5 of Appendix A.2, we define the "exact solution" of the time evolution of the traveling wave under (2.79) and (2.80) with these initial conditions as

$$\begin{aligned} \tilde{\eta}_{\text{exact}}(\boldsymbol{\alpha}, t) &= \tilde{\eta}_0\big(\boldsymbol{\alpha} - \boldsymbol{k}\alpha_0(t)\big), \\ \tilde{\varphi}_{\text{exact}}(\boldsymbol{\alpha}, t) &= \tilde{\varphi}_0\big(\boldsymbol{\alpha} - \boldsymbol{k}\alpha_0(t)\big), \end{aligned} \tag{4.37}$$

where $\boldsymbol{k} = (1, k)$, $\alpha_0(t) = ct - \mathcal{A}_0(-\boldsymbol{k}ct)$ and $\mathcal{A}_0(x_1, x_2)$ is a periodic function on $\mathbb{T}^2$ defined implicitly by (A.28) below. We see in (4.37) that the waves do not change shape as they move through the torus along the characteristic direction $\boldsymbol{k}$, but the traveling speed $\alpha_0'(t)$ in conformal space varies in time in order to maintain $\tilde{\xi}(0, 0, t) = 0$ via (2.80). By Corollary A.2.5, the exact reconstruction of $\tilde{\xi}_{\text{exact}}$ from $\tilde{\eta}_{\text{exact}}$ is

$$\tilde{\xi}_{\text{exact}}(\boldsymbol{\alpha}, t) = \tilde{\xi}_0\big(\boldsymbol{\alpha} - \boldsymbol{k}\alpha_0(t)\big) + \delta_0(t), \tag{4.38}$$

where $\delta_0(t) = ct - \alpha_0(t) = \mathcal{A}_0(-\boldsymbol{k}ct)$ measures the deviation in position from traveling at the constant speed ct in conformal space. The defining property (A.28) of $\mathcal{A}_0(x_1, x_2)$ ensures that $\tilde{\xi}_{\text{exact}}(0, 0, t) = 0$.

The significance of $\mathcal{A}_0$ is that the inverse of the mapping $\boldsymbol{x} = \boldsymbol{\alpha} + \boldsymbol{k}\tilde{\xi}_0(\boldsymbol{\alpha})$ on $\mathbb{T}^2$, assuming it is single-valued, is

$$\boldsymbol{\alpha} = \boldsymbol{x} + \boldsymbol{k}\mathcal{A}_0(\boldsymbol{x}). \tag{4.39}$$

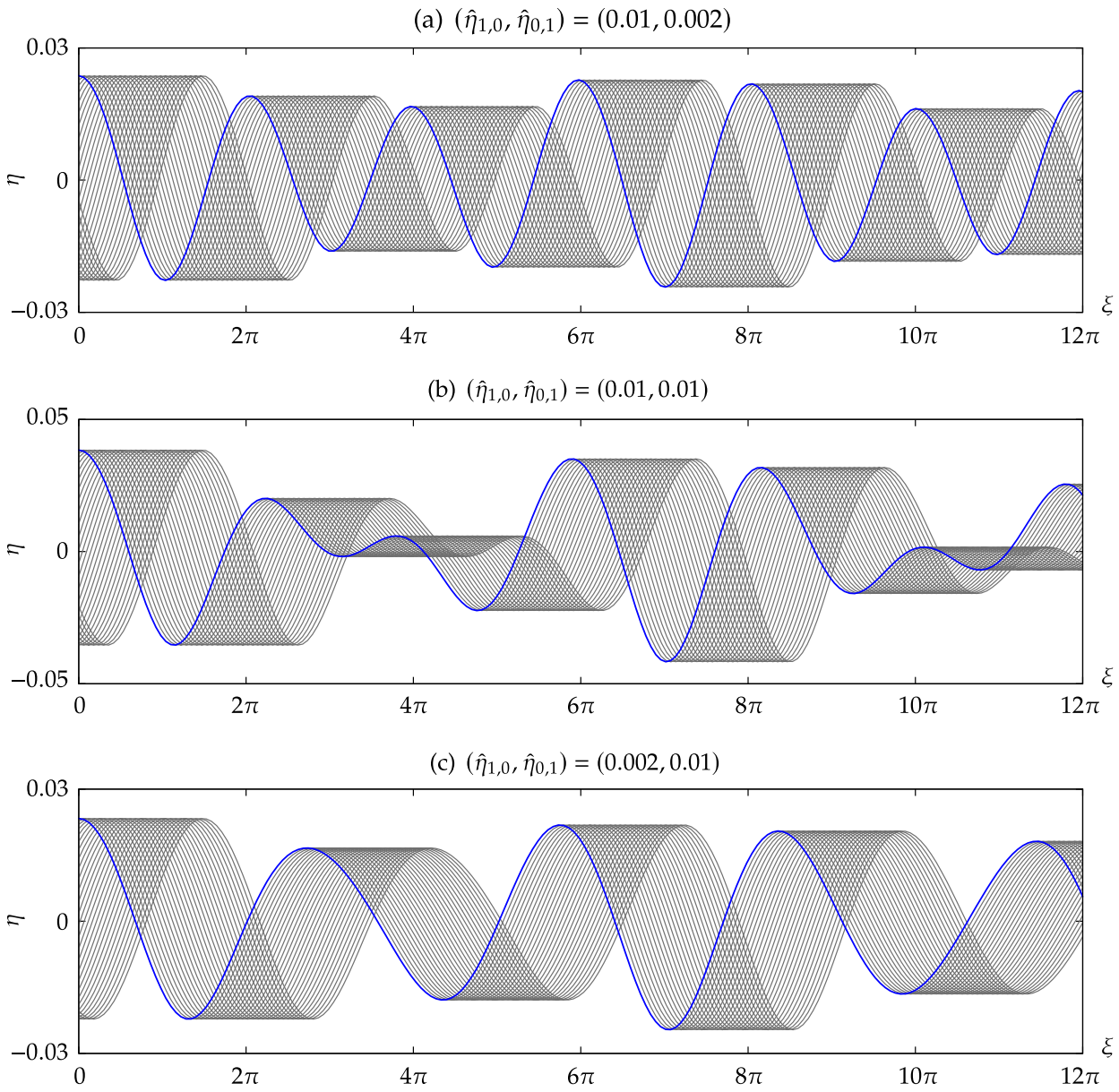

Figure 4.6: Time evolution of the traveling wave profiles, $\zeta(\alpha, t)$, from $t = 0$ to $t = 3$ in the lab frame. The thick blue lines correspond to the initial conditions.

As shown in Section 4.2.1, this allows us to express quasi-periodic solutions of the initial value problem in conformal space as quasi-periodic functions in physical space. In the traveling case considered here, the exact solutions on the torus in physical space are $\tilde{\eta}_0^{\text{phys}}(\boldsymbol{x} - \boldsymbol{k}ct)$ and $\tilde{\varphi}_0^{\text{phys}}(\boldsymbol{x} - \boldsymbol{k}ct)$, where e.g. $\tilde{\eta}_0^{\text{phys}}(\boldsymbol{x}) = \tilde{\eta}_0(\boldsymbol{x} + \boldsymbol{k}\mathcal{A}_0(\boldsymbol{x}))$. We know this already on physical grounds, but it also follows from (4.37) and (4.38) using

$$\tilde{\eta}_{\text{exact}}^{\text{phys}}(\boldsymbol{x}, t) = \tilde{\eta}_{\text{exact}}(\boldsymbol{x} + \boldsymbol{k}\mathcal{A}(\boldsymbol{x}, t)\,,\ t), \qquad \tilde{\varphi}_{\text{exact}}^{\text{phys}}(\boldsymbol{x}, t) = \tilde{\varphi}_{\text{exact}}(\boldsymbol{x} + \boldsymbol{k}\mathcal{A}(\boldsymbol{x}, t)\,,\ t), \tag{4.40}$$

where $\mathcal{A}(\boldsymbol{x}, t) = \mathcal{A}_0(\boldsymbol{x} - \boldsymbol{k}ct) - \mathcal{A}_0(-\boldsymbol{k}ct)$ satisfies the time-dependent analog of (A.28).

Figure 4.7 shows contour plots of the torus version of the $\gamma = 0.2, 1, 5$ solutions shown in Figure 4.6 at the final time computed, $T = 3$. The dashed lines show the trajectory from $t = 0$ to $t = T$ of the wave crest that begins at $(0, 0)$ and continues along the path $\alpha_1 = \alpha_0(t)$, $\alpha_2 = k\alpha_0(t)$ through the torus in (4.37). The following table gives the phase speed, c, surface tension, τ, translational shift in conformal space at the final time computed, $\alpha_0(T)$, and deviation from steady motion in conformal space, $\delta_0(T)$, for these three finite-amplitude solutions (recall that $\max\{\hat{\eta}_{1,0}, \hat{\eta}_{0,1}\} = 0.01$ and $\hat{\eta}_{1,0}/\hat{\eta}_{0,1} = \gamma$) as well as for the zero-amplitude limit:

	$\gamma = 5$	$\gamma = 1$	$\gamma = 0.2$	linear theory
c	1.552 175	1.552 197	1.553 743	$c_{\text{lin}} = 1.553\,774$
τ	1.409 665	1.410 902	1.415 342	$\tau_{\text{lin}} = 1.414\,214$
$\alpha_0(T)$	4.677 416	4.681 174	4.668 757	$c_{\text{lin}}T = 4.661\,322$
$\delta_0(T)$	−0.020 890	−0.024 583	−0.007 527	0

$(T = 3)$ (4.41)

In Figure 4.8, we plot $\delta_0(t)$ for $0 \le t \le T$ (solid lines) along with $(c - c_{\text{lin}})t$ (dashed and dotted lines) for the three finite-amplitude solutions in this table. Writing $\alpha_0(t) = c_{\text{lin}}t + [(c - c_{\text{lin}})t - \delta_0(t)]$, we see that the deviation of $\alpha_0(t)$ from linear theory over this time interval is due mostly to fluctuations in $\delta_0(t)$ rather than the steady drift $(c - c_{\text{lin}})t$ due to the change in phase speed c of the finite-amplitude wave.

Computing the exact solution (4.37) requires evaluating $\delta_0(t) = \mathcal{A}_0(-ct, -kct)$. We use Newton's method to solve the implicit equation (A.28) for $\mathcal{A}_0(x_1, x_2)$ at each point of a uniform $M \times M$ grid, with $M_1 = M_2 = M$ in the notation of Section 4.1.1.1. We then use FFTW to compute the 2d Fourier representation of $\mathcal{A}_0(x_1, x_2)$, which is used to quickly evaluate the function at any point. It would also have been easy to compute $\mathcal{A}_0(-ct, -kct)$ directly by Newton's method, but the Fourier approach is also very fast and gives more information about the function $\mathcal{A}_0(x_1, x_2)$. In particular, the modes decay to machine roundoff on the grid, corroborating the assertion in Theorem A.1.2 that $\mathcal{A}_0$ is real analytic. We use the exact solution to compute the error in timestepping (2.78) and (2.80) from $t = 0$ to $t = T$,

$$\text{err} = \sqrt{\|\tilde{\eta} - \tilde{\eta}_{\text{exact}}\|^2 + \|\tilde{\varphi} - \tilde{\varphi}_{\text{exact}}\|^2}, \quad \|\tilde{\eta}\|^2 = \frac{1}{M_1 M_2} \sum_{m_1, m_2} \tilde{\eta}\left(\frac{2\pi m_1}{M_1}, \frac{2\pi m_2}{M_2}, T\right)^2. \tag{4.42}$$

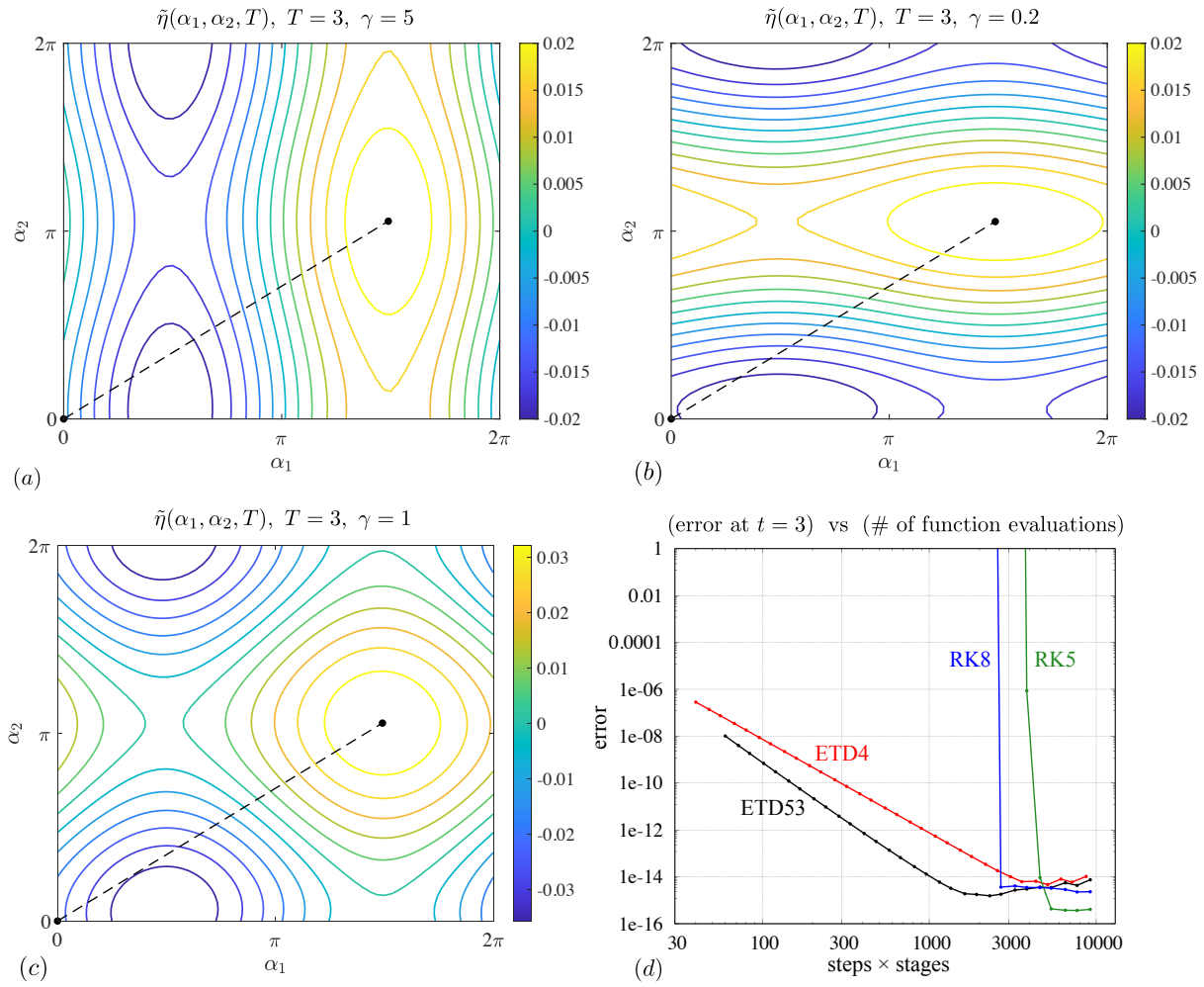

Figure 4.7: Panel (a)-(c) are contour plots of the numerical solution $\tilde{\eta}(\alpha_1, \alpha_2, T)$ on the torus corresponding to the quasi-periodic solutions $\eta(\alpha, t)$ in Figure 4.6 at the final time shown, $t = T = 3$. The dashed lines show the trajectory of the wave crest from $t = 0$ to $t = T$. Panel (d) compares the accuracy and efficiency of the proposed time-stepping schemes in computing the time evolution of the solution in panel (c).

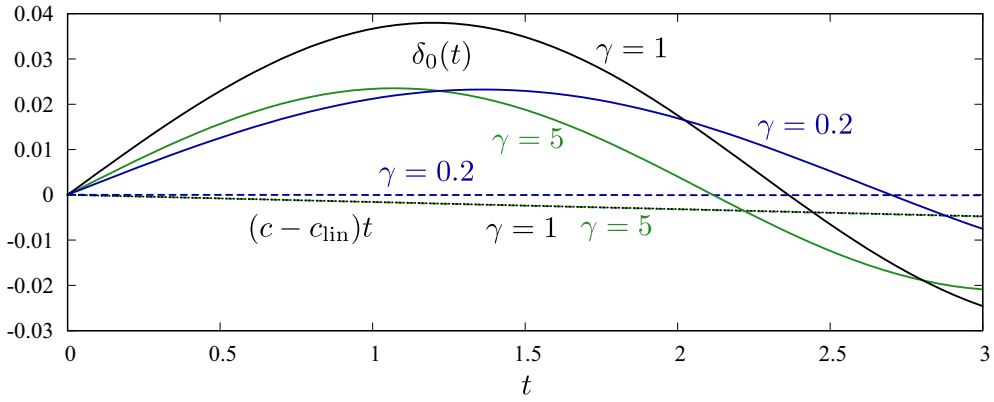

Figure 4.8: Plots of $\delta_0(t) = ct - \alpha_0(t)$ in (4.37) and $(c - c_{\text{lin}})t$ for the solutions of Figure 4.6.

We report the errors for all three waves plotted in Figure 4.6

	$\gamma = 5$	$\gamma = 1$	$\gamma = 0.2$
err	1.04×10^{-16}	1.16×10^{-16}	7.38×10^{-17}

(4.43)

using the simplest timestepping method proposed in [84] to solve (2.78), namely a 5th order explicit Runge-Kutta method using 900 uniform steps from $t = 0$ to $t = 3$. These errors appear to mostly be due to roundoff error in floating-point arithmetic, validating the accuracy of both the timestepping algorithm of [84] and the traveling wave solver of Section 4.1.1.1, which was taken as the exact solution. Evolving the solutions to compute these errors took less than a second on a laptop (with $M^2 = 3600$ gridpoints and 900 timesteps), while computing the traveling waves via the Levenberg-Marquardt method took 7 seconds on a laptop and only 0.9 seconds on a server (Intel Xeon Gold 6136, 3GHz) running on 12 threads (with $M^2 = 3600$ gridpoints and $N_{\text{tot}} = 1200$ unknowns).

We use the $\gamma = 1$ traveling solution above as a test case and compare the accuracy and efficiency of the Runge-Kutta and exponential time differencing schemes proposed in Section 4.2.1. In the panel (d) of Figure 4.7, we demonstrate the error in time-stepping this traveling wave solution from $t = 0$ to $t = 3$ using the 5th and 8th order explicit Runge-Kutta methods of Dormand and Prince [44], the 4th order ETD scheme of Cox and Matthews [28, 53], and the 5th order ETD scheme of Whalen, Brio and Moloney [79]. The surface tension in this example ($\tau = 1.410902$) is high enough that once the stepsize is sufficiently small for the Runge-Kutta methods to be stable, roundoff error dominates truncation error. So the errors suddenly drop from very large values (10^{20} or more) to machine precision. By contrast, the error in the ETD methods decreases steadily as the stepsize is reduced, indicating that the small-scale decomposition introduced in (4.34) is successful in removing stiffness from the equations of motion [47, 48].

4.2.3 Overturning Waves

Next we present a spatially quasi-periodic water wave computation in which some of the wave peaks overturn as they evolve while others do not. Conformal mapping methods have been used previously to compute overturning waves. For example, Dyachenko and Newell [39] use this approach to study whitecapping in the ocean and Wang *et al.* [60] use it to compute solitary and periodic overturning traveling flexural-gravity waves. The novelty of our work is the computation of a spatially quasi-periodic water wave in which every wave peak evolves differently, and only some of them overturn. Since torus functions are involved, the number of degrees of freedom is squared, leading to a large-scale computation. For simplicity, we set the surface tension parameter, τ, to zero.

We first seek spatially periodic dynamics in which the initial wave profile has a vertical tangent line that overturns when evolved forward in time and flattens out when evolved backward in time. Through trial and error, we selected the following parametric curves for the initial wave profile and velocity potential of this auxiliary periodic problem:

$$\xi_1(\sigma) = \sigma + \frac{3}{5}\sin\sigma - \frac{1}{5}\sin 2\sigma, \qquad \begin{aligned} \eta_1(\sigma) &= -(1/2)\cos(\sigma + \pi/2.5), \\ \varphi_1(\sigma) &= -(1/2)\cos(\sigma + \pi/4). \end{aligned} \tag{4.44}$$

Note that $\xi_1'(\sigma) = 0$ when $\sigma \in \pi + 2\pi\mathbb{Z}$, and otherwise $\xi_1'(\sigma) > 0$. Thus, vertical tangent lines occur where $\xi_1(\sigma) \in \pi + 2\pi\mathbb{Z}$ and $\eta_1(\sigma) = -0.5\cos(1.4\pi) = 0.154508$; see Figure 4.9.

To convert (4.44) to a conformal parametrization, we search for 2π-periodic functions $\eta_2(\alpha)$ and $B_2(\alpha)$ and a number x_2 such that

$$\alpha + x_2 + H\big[\eta_2\big](\alpha) = \xi_1(\alpha + B_2(\alpha)), \qquad \eta_2(\alpha) = \eta_1(\alpha + B_2(\alpha)), \qquad B_2(0) = 0. \tag{4.45}$$

First we solve a simpler variant in which x_2 is absent and $B_2(0)$ is unspecified. Specifically, we solve $\alpha + H\big[\eta_3\big](\alpha) = \xi_1(\alpha + B_3(\alpha))$, $\eta_3(\alpha) = \eta_1(\alpha + B_3(\alpha))$ for $\eta_3(\alpha)$ and $B_3(\alpha)$ on a uniform grid with $M = 4096$ gridpoints on $[0, 2\pi)$ using Newton's method. The Hilbert transform is computed with spectral accuracy in Fourier space. We then define x_2 as the solution of $x_2 + B_3(x_2) = 0$ that is smallest in magnitude. We solve this equation by a combination of root bracketing and Newton's method; the result is $x_2 = 0.393458$. Finally, we define $B_2(\alpha) = x_2 + B_3(\alpha + x_2)$ and $\eta_2(\alpha) = \eta_3(\alpha + x_2)$, which satisfy (4.45).

As shown in Figure 4.9, the initial conditions $\eta_2(\alpha)$ and

$$\varphi_2(\alpha) = \varphi_1(\alpha + B_2(\alpha)) \tag{4.46}$$

have the desired property that the wave overturns when evolved forward in time and flattens out when evolved backward in time. In other words, the wave becomes less steep in the neighborhood of the initial vertical tangent line when time is reversed. However, it does not evolve backward to a flat state. Instead, a secondary wave crest forms to the right of the initial wave crest and grows in amplitude as t decreases. This secondary wave crest resembles the early stages of the fluid jets that were observed by Aurther *et al.* [11] to

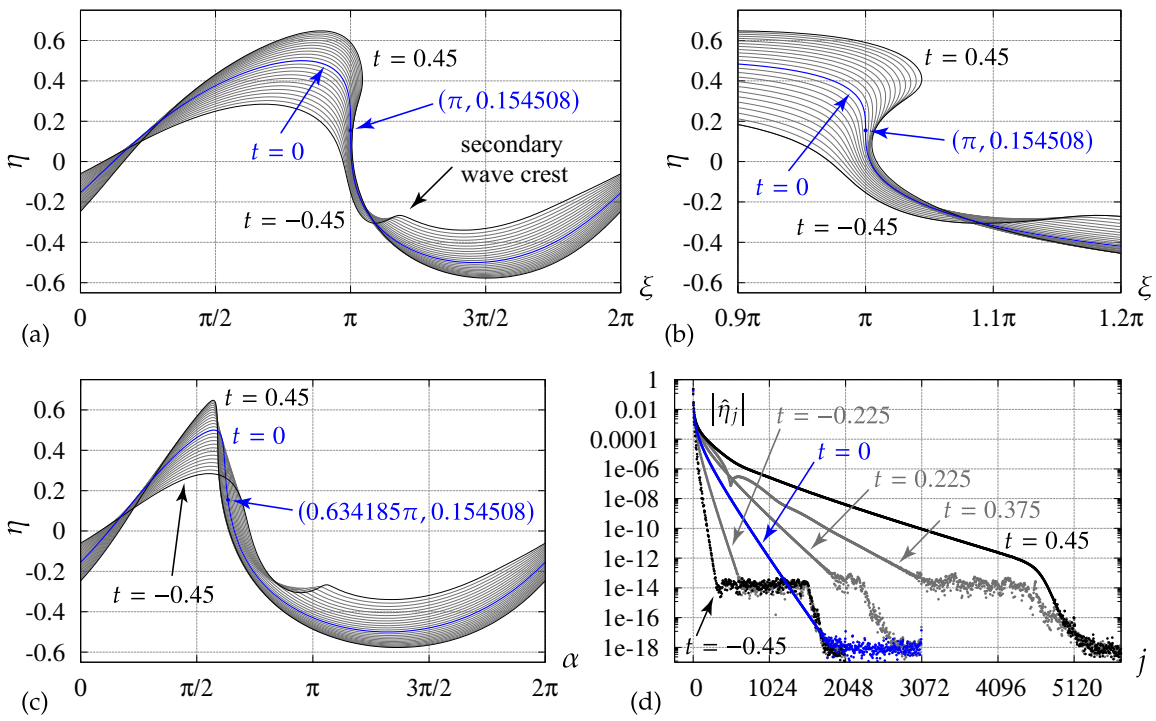

Figure 4.9: Time evolution of a spatially periodic water wave initialized via (4.44) and evolved forward and backward in time to $t = \pm 0.45$. Panels (a) and (b) show snapshots of the wave in physical space; panel (c) shows snapshots of $\eta(\alpha, t)$ in conformal space; and panel (d) shows snapshots of $|\hat{\eta}_j(t)|$ in Fourier space. The initial condition ($t = 0$) is shown in blue in each plot.

form in the wave troughs when the initial condition $\eta_0(x) = \left(\frac{1}{3}\sin x + \frac{1}{6}\sin 2x + \frac{1}{3}\sin 3x\right)$ is evolved from rest in the graph-based formulation (2.15).

The blue markers in panels (a) and (b) of Figure 4.9 show the location of the vertical tangent line in physical space at $t = 0$. The blue marker in panel (c) shows the corresponding point in conformal space. When the wave overturns for $t > 0$ in physical space, it is because $\alpha \mapsto \xi(\alpha, t)$ no longer increases monotonically. Indeed, we see in panel (c) that $\eta(\alpha, t)$ remains single-valued as a function of the conformal variable α but becomes very steep. This causes the Fourier mode amplitudes in panel (d) to decay more slowly as t increases. We used different mesh sizes and timesteps in the regions $0 \le t \le 0.3$, $0.3 \le t \le 0.45$ and $0 \ge t \ge -0.45$ to maintain spectral accuracy; details are given below when discussing the quasi-periodic calculation. The drop-off in $|\hat{\eta}_j|$ from 10^{-14} to 10^{-18} as j approaches the Nyquist frequency $M/2$ is due to the 1D version of the filter (4.36), which is applied after each timestep. Floating point errors of size 10^{-14} occur in the discretiza-

tion of the equations of motion while errors of size 10^{-18} are due to having computed the inverse FFT of the filtered data to get back to real space before taking the FFT again to plot the Fourier data.

We turn the solution of this auxiliary periodic problem into a spatially quasi-periodic solution by defining initial conditions on the torus of the form

$$\tilde{\eta}_0(\alpha_1, \alpha_2) = \eta_2(\alpha_1), \qquad \tilde{\varphi}_0(\alpha_1, \alpha_2) = \varphi_2(\alpha_1)\cos(\alpha_2 - q), \tag{4.47}$$

where q is a free parameter that we choose heuristically to be $q = 0.6k\pi = 1.3329$ in order to make the first wave crest to the right of the origin behave similarly to the periodic 1D solution of Figure 4.9. (This will be explained below).

The results of the quasi-periodic calculation are summarized in Figures 4.10 and 4.11. Panel (a) of Figure 4.10 shows snapshots of the solution at $t = (\ell/6)T$ for $0 \le \ell \le 6$ over the range $0 \le \xi(\alpha) \le 16\pi$, where $T = 0.225$. The initial wave profile, $\zeta_0(\alpha) = \xi_0(\alpha) + i\eta_0(\alpha)$ with $\eta_0(\alpha) = \tilde{\eta}_0(\alpha, k\alpha)$, is plotted with a thick blue line. The wave profile is plotted with a thick black line at $t = T$ and with thin grey lines at intermediate times. Panel (b) zooms in on the first wave in panel (a), which overturns as the wave crest moves up and right while the wave trough moves down and left, as indicated by the blue arrows. This is very similar (by design) to the forward evolution of the auxiliary periodic wave of Figure 4.9, with initial conditions $\eta_2(\alpha)$, $\varphi_2(\alpha)$. Panels (c) and (d) zoom in on two other wave crests from panel (a) that flatten out (rather than overturn) as t advances from 0 to T. Panel (e) shows another type of behavior in which the wave overturns due to the wave trough moving down and left faster than the wave crest moves down and left. Panel (f) shows the evolution of the velocity potential $\varphi(\alpha, t)$ over $0 \le t \le T$. Unlike $\eta_0(\alpha)$, the initial velocity potential $\varphi_0(\alpha) = \tilde{\varphi}_0(\alpha, k\alpha)$ is not 2π-periodic due to the factor of $\cos(\alpha_2 - q)$ in (4.47).

Panels (a) and (d) of Figure 4.11 show surface plots of $\tilde{\eta}(\alpha_1, \alpha_2, T)$ and $\tilde{\varphi}(\alpha_1, \alpha_2, T)$ at the final time computed, $T = 0.225$. The corresponding contour plots are shown in panels (b) and (c). Initially, $\tilde{\eta}(\alpha_1, \alpha_2, 0)$ depends only on α_1; however, by $t = T$, the dependence on α_2 is clearly visible. Although the waves overturn in some places when $\eta(\alpha, t) = \tilde{\eta}(\alpha, k\alpha, t)$ is plotted parametrically versus $\xi(\alpha, t)$ with $t > 0$ held fixed, both $\tilde{\eta}$ and $\tilde{\varphi}$ are single-valued functions of α_1 and α_2 at all times. Nevertheless, throughout the evolution, $\tilde{\eta}(\alpha_1, \alpha_2, t)$ has a steep dropoff over a narrow range of values of α_1. Initially, $\tilde{\eta}_0(\alpha_1, \alpha_2) = \eta_2(\alpha_1) = \eta_1(\alpha_1 + B_2(\alpha_1))$ and the rapid dropoff occurs for α_1 near the solution of $\alpha_1 + B_2(\alpha_1) = \pi$ (since the vertical tangent line occurs at $\xi_1(\sigma) + i\eta_1(\sigma)$ with $\sigma = \pi$). Using Newton's method, we find that this occurs at $\alpha_1 = 0.634185\pi$. The blue curve in panel (c) of Figure 4.9 gives $\eta_2(\alpha)$. If one zooms in on this plot, one finds that $\eta_2(\alpha)$ decreases rapidly by more than half its crest-to-trough height over the narrow range $0.6\pi \le \alpha \le 0.667\pi$. At later times, $\tilde{\eta}(\alpha_1, \alpha_2, t)$ continues to drop off rapidly when α_1 traverses this narrow range in spite of the dependence on α_2. This can be seen in panel (b) of Figure 4.11, where there is a high clustering of nearly vertical contour lines separating the yellow-orange region from the blue region. Over this narrow window, $\tilde{\varphi}(\alpha_1, \alpha_2, t)$ also varies rapidly with respect to α_1.

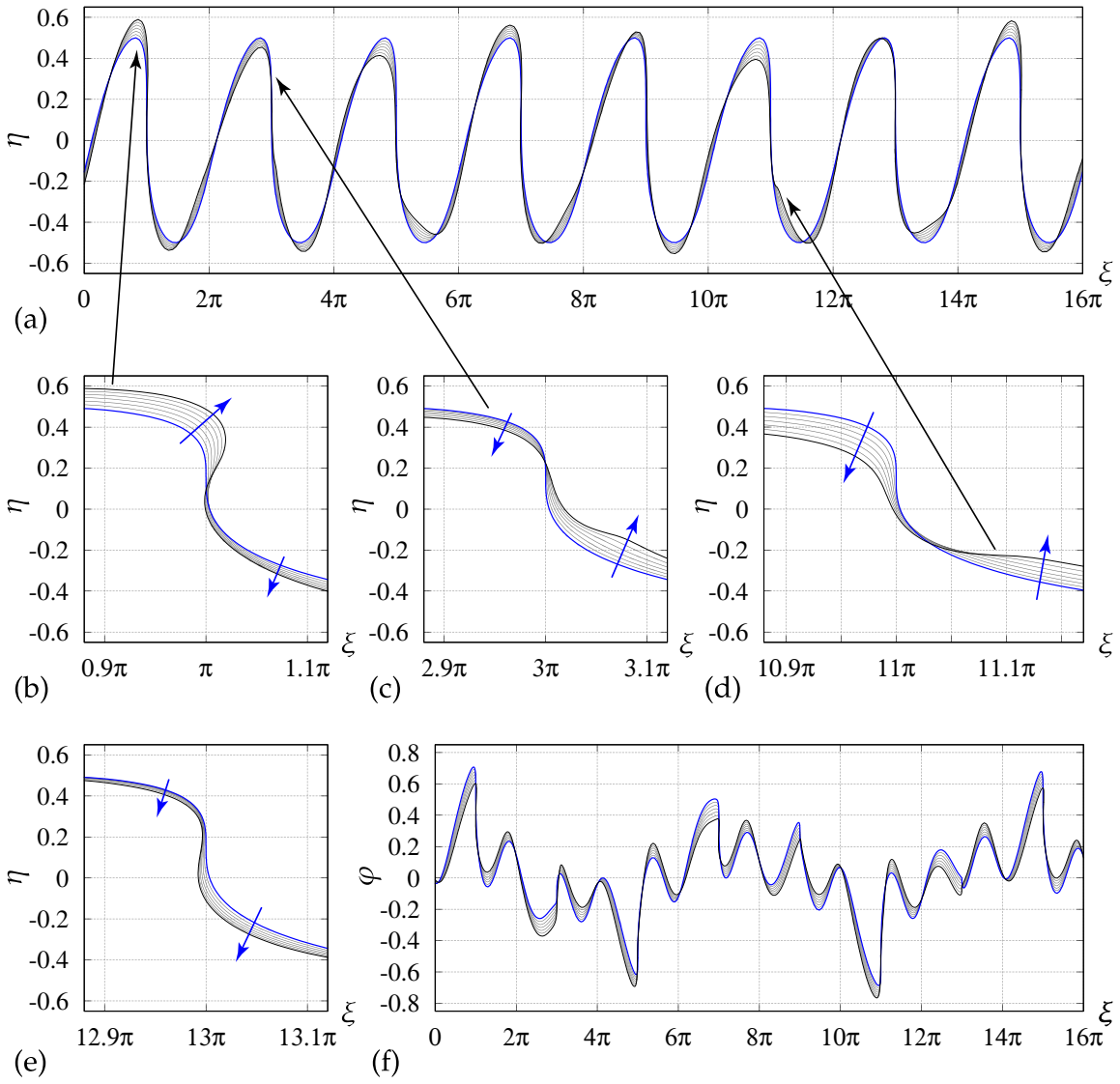

Figure 4.10: Snapshots in time of a spatially quasi-periodic water wave with a periodic initial wave profile with vertical tangent lines at $\xi = \pi + 2\pi n$, $n \in \mathbb{Z}$. A quasi-periodic initial velocity potential causes some of the peaks to overturn for $t > 0$ while others do not. Panels (a) and (f) show $\eta(\alpha, t)$ and $\varphi(\alpha, t)$ versus $\xi(\alpha, t)$ over $0 \leq x \leq 16\pi$ and $0 \leq t \leq T = 0.225$. Panels (b)–(e) show the results of panel (a) in more detail. The blue arrows show the direction of travel of the wave at various locations.

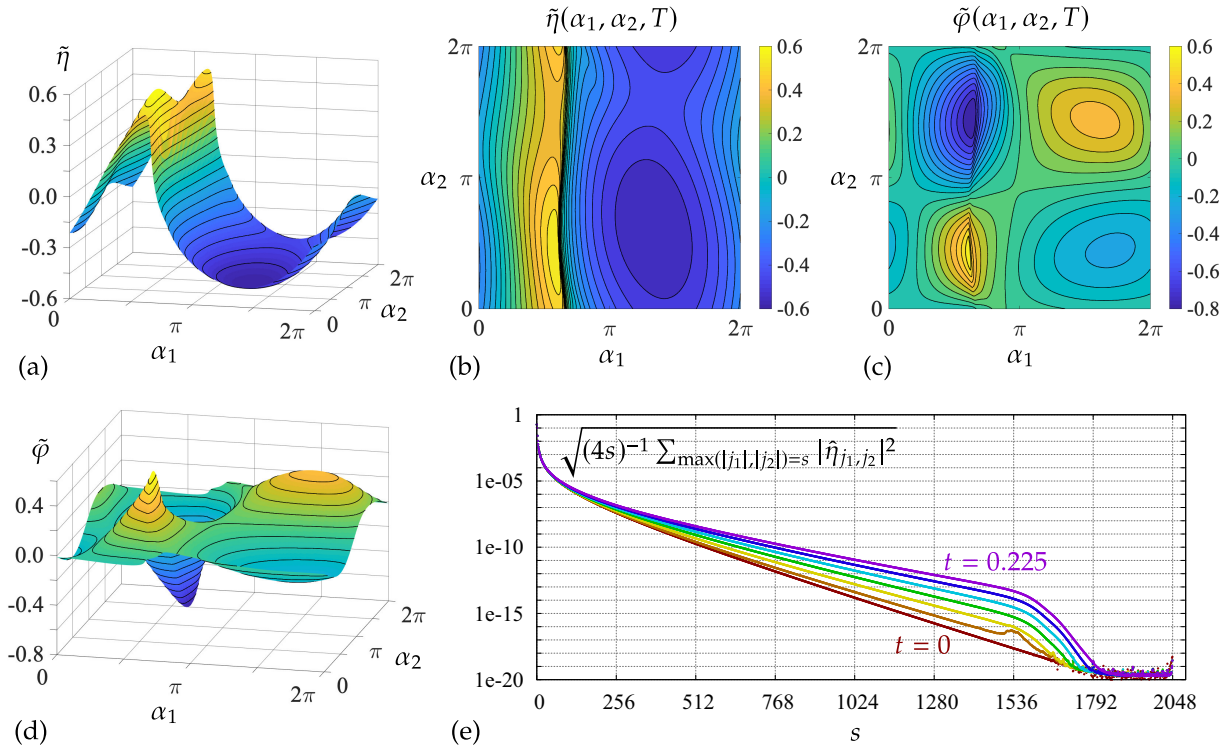

Figure 4.11: Surface and contour plots of the torus version of the solution plotted in Figure 4.10 at the final time $T = 0.225$. The rapid dropoff in $\tilde{\eta}(\alpha_1, \alpha_2, t)$ over the window $0.6\pi \le \alpha_1 \le 0.667\pi$ persists from the initial state in which $\tilde{\eta}_0(\alpha_1, \alpha_2)$ does not depend on α_2. Panel (e) shows the exponential decay of Fourier modes with respect to the shell index s at different times.

Many gridpoints are needed to resolve these rapid variations with spectral accuracy. Although $\xi_1(\sigma)$, $\eta_1(\sigma)$ and $\varphi_1(\sigma)$ involve only a few nonzero Fourier modes, conformal reparametrization via (4.45) vastly increases the Fourier content of the initial condition. We used $M = 6144$ gridpoints to evolve the periodic auxiliary problem of Figure 4.9 from $t = 0$ to $t = 0.3$ using the 8th order Runge-Kutta method of Dormand and Prince [44] with stepsize $\Delta t = 2.08333 \times 10^{-5}$. We then switched to $M = 12288$ gridpoints to evolve from $t = 0.3$ to $t = 0.45$ with $\Delta t = 7.5 \times 10^{-6}$. In the reverse direction, we used $M = 4096$ gridpoints to evolve from $t = 0$ to $t = -0.45$ with $\Delta t = -4.6875 \times 10^{-5}$. Studying the Fourier modes in panel (d) of Figure 4.9, it appears that 4096 gridpoints (2048 modes) are sufficient to maintain double-precision accuracy forward or backward in time to $t = \pm 0.225$. Using this as a guideline for the quasi-periodic calculation, we evolved (2.78) on a 4096×4096 spatial grid using the 8th order explicit Runge-Kutta method described in Section 4.1.1.1. The calculation involved 5400 time steps from $t = 0$ to $t = T = 0.225$, which took 2.5 days on 12 threads running on a server with two 3.0 GHz Intel Xeon Gold 6136 processors.

Additional threads had little effect on the running time as the FFT calculations require a lot of data movement relative to the number of floating point operations involved.

Panel (e) of Figure 4.11 shows the ℓ^2 average of the Fourier mode amplitudes $|\hat{\eta}_{j_1,j_2}|$ in each shell of indices satisfying $\max(|j_1|,|j_2|) = s$ for $1 \le s \le 2048$. Since $\hat{\eta}_{-j_1,-j_2} = \overline{\hat{\eta}_{j_1,j_2}}$, we can discard half the modes and sweep through the lattice along straight lines from $(0,s)$ to (s,s) to $(s,-s)$ to $(1,-s)$, which sweeps out $4s$ index pairs. (The same ordering is used to enumerate the unknowns in the nonlinear least squares method proposed in [83] to compute quasi-periodic traveling water waves.) We see in panel (e) that as time increases, the modes continue to decay at an exponential rate with respect to s, but the decay rate is slower at later times. The rapid dropoff in the mode amplitudes for $s \ge 1536$ is due to the Fourier filter. At the final time $t = T = 0.225$, the modes still decay by 12 orders of magnitude from $s = 1$ to $s = 1536$, so we believe the solution is correct to 10–12 digits. A finer grid would be required to maintain this accuracy over longer times. As in Figure 4.9, the additional drop-off in the amplitude of Fourier modes from $s = 1536$ to $s = 2048$ in panel (e) is due applying the filter (4.36) to the solution after every timestep.

Beyond monitoring the decay of Fourier modes, as an additional check of accuracy, we compute the average energy, mass and momentum of the solution of Figure 4.11 as a function of time. The results are shown in Table 4.1. The formulas for $\tilde{E}$, $\tilde{M}$ and $\tilde{P}$ are given in Section 2.2.5. In the table below, we report the values of the above three quantities divided by $(2\pi)^2$; this scaling has the advantage that $\tilde{E}$, $\tilde{M}$ and $\tilde{P}$ do not suddenly jump by a factor of 2π when periodic functions are viewed as quasi-periodic functions that depend on α_1 only.

The numerical results in Table 4.1 show that energy is conserved to a relative error of $1.5\times10^{-13}/0.0975 = 1.5\times10^{-12}$; mass is conserved to a relative error of $3.3\times10^{-13}/0.0464 = 7.1\times10^{-12}$; and momentum is conserved to an absolute error of 4.6×10^{-15} over the course of the numerical computation of Figure 4.11. This gives further evidence that $\tilde{\eta}$ and $\tilde{\varphi}$ are accurate to 10–12 digits. The mass being negative is an artifact of the choice of $\xi_1(\sigma)$ and $\eta_1(\sigma)$ in (4.44). While $\eta_1(\sigma)$ has zero mean as a function of σ, its average value with respect to x is $(2\pi)^{-1}\int_0^{2\pi}\eta_1(\sigma)\xi_1'(\sigma)\,d\sigma = -(3\pi/40)(\sqrt{5}-1) = -0.04635254915624$. If we had added a constant to $\tilde{\eta}$ to make M zero initially, it would have remained zero up numerical errors, similar to P_x, which is initially zero since $\tilde{\eta}$ and $\tilde{\varphi}$ in (4.47) are independent of α_2 except for the factor of $\cos(\alpha_2 - q)$. The constant value of the energy would also change if a constant were added to $\tilde{\eta}$.

The rationale for setting $q = 0.6k\pi$ in (4.47) is that $\cos(\alpha_2 - q) \approx 1$ where the characteristic line $(\alpha, k\alpha)$ crosses the dropoff in the torus near $\alpha_1 = 0.6\pi$ for the first time. Locally, $\varphi_0(\alpha) = \tilde{\varphi}_0(\alpha, k\alpha)$ is close to $\varphi_2(\alpha)$, the initial condition of the auxiliary periodic problem, so we expect the quasi-periodic wave to evolve similarly to the periodic wave near $x = \pi$ for a short time. (Here $z = x + iy$ describes physical space). This is indeed what happens, which may be seen by comparing panel (b) of Figure 4.9 to panel (b) of Figure 4.10, keeping in mind that $t \in [-0.45, 0.45]$ in the former plot and $t \in [0, 0.225]$ in the latter plot. Advancing α from 0.6π to 10.6π causes the characteristic line $(\alpha, k\alpha)$ to cross a

t	$\tilde{E}/(2\pi)^2$	$\tilde{M}/(2\pi)^2$	$\tilde{P}/(2\pi)^2$
0.000	0.09750133157054	−0.04635254915643	1.19×10^{-15}
0.025	0.09750133157057	−0.04635254915623	-2.98×10^{-15}
0.050	0.09750133157058	−0.04635254915621	-1.24×10^{-15}
0.075	0.09750133157057	−0.04635254915619	1.15×10^{-15}
0.100	0.09750133157059	−0.04635254915617	0.43×10^{-15}
0.125	0.09750133157060	−0.04635254915616	0.34×10^{-15}
0.150	0.09750133157062	−0.04635254915614	4.59×10^{-15}
0.175	0.09750133157063	−0.04635254915613	1.35×10^{-15}
0.200	0.09750133157064	−0.04635254915611	-2.18×10^{-15}
0.225	0.09750133157069	−0.04635254915610	-2.10×10^{-15}

Table 4.1: Average energy, mass and momentum of the overturning wave example of Figure 4.11 at the times indicated.

periodic image of the dropoff at $\alpha_2 = 10.6k\pi$, where $\cos(\alpha_2 - q) = -0.9752 \approx -1$. Locally, $\varphi_0(\alpha)$ is close to $-\varphi_2(\alpha)$, the initial condition of the time-reversed auxiliary periodic problem. Thus, we expect the quasi-periodic wave to evolve similarly to the time-reversed periodic wave near $x = 11\pi$. (Recall that $\xi_0(0.634185\pi) = \pi$, so $\xi_0(10.634185\pi) = 11\pi$). Comparing panel (b) of Figure 4.9 to panel (d) of Figure 4.10 confirms that this does indeed happen. At most wave peaks, the velocity potential of the quasi-periodic solution is not closely related to that of the periodic auxiliary problem since the cosine factor is not near a relative maximum or minimum, where it is flat. As a result, the wave peaks of the quasi-periodic solution evolve in many different ways as α varies over the real line.

Chapter 5

Conclusion

In this thesis, we have formulated the two-dimensional, infinite depth gravity-capillary wave problem in a spatially quasi-periodic, conformal mapping framework. We have developed numerical methods for solving the quasi-periodic initial value problem as well as the traveling wave problem and presented a numerical study of the solutions that are of two quasi-periods.

We developed two time-stepping strategies for solving the quasi-periodic initial value problem, an explicit Runge-Kutta method and an exponential time differencing scheme. We numerically verified a result in [83] that quasi-periodic traveling waves evolve in time on the torus $\mathbb{T}^2$ in the direction $(1, k)$ without changing form, though their speed is non-uniform in conformal space if the condition $\tilde{\xi}(0, 0, t) = 0$ is imposed via (2.80). We then performed a convergence study to demonstrate the effectiveness of the small-scale decomposition at removing stiffness from the evolution equations when the surface tension is large. Finally, we presented the results of a large-scale computation of a spatially quasi-periodic overturning water wave for which the wave peaks exhibit a wide array of dynamic behavior.

We have formulated the quasi-periodic traveling wave problem as a nonlinear least squares problem and adapted a variant of the Levenberg-Marquardt method introduced in [82] to compute the solutions. We have numerically demonstrated the existence of quasi-periodic traveling solutions of two types: solutions that bifurcate from the zero solution and solutions that bifurcate from finite-amplitude periodic traveling solutions. For the first type, the solutions are parametrized by two bifurcation parameters $\hat{\eta}_{1,0}$ and $\hat{\eta}_{0,1}$, which are fixed while τ, c and the other Fourier coefficients $\hat{\eta}_{j_1,j_2}$ are varied to search for solutions. We computed the asymptotic expansions of these solutions; the convergence of these expansions is still unknown. For the second type, we applied a Fourier-Bloch decomposition to study the linearization of (3.8) around periodic traveling solutions. We used the zero eigenvector of the linearization as the bifurcation direction to jump from the primary branch of periodic solutions to the quasi-periodic bifurcation branch. As an example, we computed large-amplitude overturning quasi-periodic traveling solutions that bifurcate from a overturning periodic solution.

Appendix A

Properties of Spatially Quasi-Periodic Solutions

A.1 Quasi-Periodic Families of Solutions

In this appendix we explore the effect of introducing phases in the reconstruction of one-dimensional quasi-periodic solutions of (2.78) from solutions of the torus version of these equations. This ultimately makes it possible to show that if all the solutions in the family are single-valued and have no vertical tangent lines, the corresponding solutions of the original graph-based formulation (2.15)–(2.18) of the Euler equations are quasi-periodic in physical space.

Theorem A.1.1 *The solution pair* $(\tilde{\zeta}, \tilde{\varphi})$ *on the torus represents an infinite family of quasi-periodic solutions on* $\mathbb{R}$ *given by*

$$\begin{aligned} \zeta(\alpha, t\,;\, \theta_1, \theta_2, \delta) &= \alpha + \delta + \tilde{\zeta}(\theta_1 + \alpha, \theta_2 + k\alpha, t), \\ \varphi(\alpha, t\,;\, \theta_1, \theta_2) &= \tilde{\varphi}(\theta_1 + \alpha, \theta_2 + k\alpha, t), \end{aligned} \qquad \begin{pmatrix} \alpha \in \mathbb{R},\ t \geq 0 \\ \theta_1, \theta_2, \delta \in \mathbb{R} \end{pmatrix}. \tag{A.1}$$

Proof: We claim that by solving (2.78) throughout $\mathbb{T}^2$, any one-dimensional (1D) slice of the form (A.1) will satisfy the kinematic condition (2.71) and the Bernoulli equation (2.77). Let us freeze θ_1, θ_2 and δ and drop them from the notation on the left-hand side of (A.1). Consider substituting $\eta = \operatorname{Im} \zeta$ and φ from (A.1) into (2.78), and let $u(\alpha) = \tilde{u}(\theta_1+\alpha, \theta_2+k\alpha)$ represent the input of any α-derivative or Hilbert transform in an intermediate calculation. Both η and φ are of this form. By Definition 2.2.3, $H[u](\alpha) = H[\tilde{u}](\theta_1 + \alpha, \theta_2 + k\alpha)$, and clearly $u'(\alpha) = [(\partial_{\alpha_1} + k\partial_{\alpha_2})\tilde{u}](\theta_1 + \alpha, \theta_2 + k\alpha)$, so the output retains this form. We conclude that computing (2.78) on the torus gives the same results for $\tilde{\eta}_t$ and $\tilde{\varphi}_t$ when evaluated at $(\theta_1 + \alpha, \theta_2 + k\alpha)$ as the 1D calculations of η_t and φ_t when evaluated at α. Since $\tilde{\xi}(\cdot, t) = x_0(t) + H[\tilde{\eta}(\cdot, t)]$ on $\mathbb{T}^2$,

$$\xi(\alpha, t) = \alpha + \delta + x_0(t) + H[\eta(\cdot, t)](\alpha), \tag{A.2}$$

which follows from (A.1) and $H[\eta(\cdot,t)](\alpha) = H[\tilde{\eta}(\cdot,t)](\theta_1+\alpha,\theta_2+k\alpha)$. Thus, computing $\xi_\alpha = 1+H[\eta_\alpha]$ in (2.78) gives the same result as just differentiating ξ from (A.1) and (A.2). In the 1D problem, the right-hand side of (2.74) represents complex multiplication of z_α with a bounded analytic function (namely z_t/z_α) whose imaginary part equals $-\chi$ on the real axis; thus, in (2.74), ξ_t differs from $H[\eta_t]$ by a constant. This constant is determined by comparing ξ_t in (2.74) with ξ_t from (A.2), which leads to the same formula (2.75) for dx_0/dt that is used in the torus calculation. Here we note that a phase shift does not affect the mean of a periodic function on the torus, i.e. $P_0[S_{\boldsymbol{\theta}}\tilde{u}] = P_0[\tilde{u}]$ where $S_{\boldsymbol{\theta}}[\tilde{u}](\boldsymbol{\alpha}) = \tilde{u}(\boldsymbol{\alpha}+\boldsymbol{\theta})$. We have assumed that in the 1D calculation, C_1 is chosen to agree with that of the torus calculation. Since C_1 only affects the tangential velocity of the interface parametrization, it can be specified arbitrarily. Left-multiplying (2.74) by $(-\eta_\alpha,\xi_\alpha)$ eliminates C_1 and yields the kinematic condition (2.71). Since the Bernoulli equation (2.77) holds on the torus, it also holds in the 1D calculation, as claimed. □

For each solution in the family (A.1), there are many others that represent identical dynamics up to a spatial phase shift or α-reparametrization. Changing δ merely shifts the solution in physical space. In fact, δ does not appear in the equations of motion (2.74) — it is only used to reconstruct the curve via (A.2). The relations

$$\begin{aligned}\zeta(\alpha+\alpha_0,t\,;\,\theta_1,\theta_2,\delta) &= \zeta(\alpha,t\,;\,\theta_1+\alpha_0,\theta_2+k\alpha_0,\delta+\alpha_0),\\ \varphi(\alpha+\alpha_0,t\,;\,\theta_1,\theta_2) &= \varphi(\alpha,t\,;\,\theta_1+\alpha_0,\theta_2+k\alpha_0),\end{aligned} \tag{A.3}$$

show that shifting α by α_0 leads to another solution already in the family. This shift reparametrizes the curve but has no effect on its evolution in physical space. If we identify two solutions that differ only by a spatial phase shift or α-reparametrization, the parameters $(\theta_1,\theta_2,\delta)$ become identified with $(0,\theta_2-k\theta_1,0)$. Every solution is therefore equivalent to one of the form

$$\begin{aligned}\zeta(\alpha,t\,;\,0,\theta,0) &= \alpha+\tilde{\zeta}(\alpha,\theta+k\alpha,t),\\ \varphi(\alpha,t\,;\,0,\theta) &= \tilde{\varphi}(\alpha,\theta+k\alpha,t)\end{aligned} \qquad \alpha\in\mathbb{R}\,,\ t\geq 0\,,\ \theta\in[0,2\pi). \tag{A.4}$$

Within this smaller family, two values of θ lead to equivalent solutions if they differ by $2\pi(n_1k+n_2)$ for some integers n_1 and n_2. This equivalence is due to solutions "wrapping around" the torus with a spatial shift,

$$\zeta(\alpha+2\pi n_1,t\,;\,0,\theta,0) = \zeta(\alpha,t\,;\,0,\theta+2\pi(n_1k+n_2),2\pi n_1), \quad \big(\alpha\in[0,2\pi),\ n_1\in\mathbb{Z}\big). \tag{A.5}$$

Here n_2 is chosen so that $0\leq\big(\theta+2\pi(n_1k+n_2)\big)<2\pi$ and we used periodicity of $\zeta(\alpha,t\,;\,\theta_1,\theta_2,\delta)$ with respect to θ_1 and θ_2. It usually suffices to restrict attention to $\alpha\in[0,2\pi)$ by making use of (A.5). One exception is determining whether the curve self-intersects. In that case it is more natural to tile the plane with periodic copies of the torus and consider the straight line parametrization of (A.4). Indeed, it is conceivable that

$$\zeta(\alpha,t;0,\theta,0) = \zeta(\beta,t;0,\theta,0) \tag{A.6}$$

with $|\alpha - \beta|$ as large as $2M$, where M is a bound on $|\tilde{\zeta}|$ over $\mathbb{T}^2$, and the condition (A.6) becomes hard to understand if (A.5) is used to map α and β back to $[0, 2\pi)$ with different choices of n_1 or n_2.

We now show that $\eta^{\text{phys}}(x, t\,;\, \theta_1, \theta_2, \delta)$ and $\varphi^{\text{phys}}(x, t\,;\, \theta_1, \theta_2, \delta)$ can be defined and computed easily from $\zeta(\alpha, t\,;\, \theta_1, \theta_2, \delta)$ and $\varphi(\alpha, t\,;\, \theta_1, \theta_2)$ if all of the waves in the family (A.4) are single-valued and have no vertical tangent lines, and that η^{phys} and φ^{phys} are quasi-periodic functions of x. To simplify notation, let $\boldsymbol{\alpha} = (\alpha_1, \alpha_2)$, $\boldsymbol{x} = (x_1, x_2)$ and $\boldsymbol{k} = (1, k)$.

Theorem A.1.2 *Fix $t \geq 0$ and suppose $\xi_\alpha(\alpha, t\,;\, 0, \theta, 0) > 0$ for all $(\alpha, \theta) \in [0, 2\pi) \times [0, 2\pi)$. Then the equation*

$$\mathcal{A}(\boldsymbol{x}, t) + \tilde{\xi}\big(\boldsymbol{x} + \boldsymbol{k}\mathcal{A}(\boldsymbol{x}, t)\,,\; t\big) = 0, \tag{A.7}$$

defines a unique function $\mathcal{A}(x_1, x_2, t)$ on $\mathbb{T}^2$ that is periodic and real analytic in x_1 and x_2. The inverse of the change of variables $\boldsymbol{x} = \boldsymbol{\alpha} + \boldsymbol{k}\tilde{\xi}(\boldsymbol{\alpha}, t)$ on $\mathbb{T}^2$ is given by

$$\boldsymbol{\alpha} = \boldsymbol{x} + \boldsymbol{k}\mathcal{A}(\boldsymbol{x}, t). \tag{A.8}$$

Proof: First we check that if $\mathcal{A}$ satisfies (A.7), then (A.8) is the inverse of the change of variables $\boldsymbol{x} = \boldsymbol{\alpha} + \boldsymbol{k}\tilde{\xi}(\boldsymbol{\alpha}, t)$. Given $\boldsymbol{x} \in \mathbb{T}^2$, define $\boldsymbol{\alpha}$ by (A.8). Then

$$\boldsymbol{\alpha} + \boldsymbol{k}\tilde{\xi}(\boldsymbol{\alpha}, t) = \big(\boldsymbol{x} + \boldsymbol{k}\mathcal{A}(\boldsymbol{x}, t)\big) - \boldsymbol{k}\mathcal{A}(\boldsymbol{x}, t) = \boldsymbol{x}, \tag{A.9}$$

as required. Next we show existence and uniqueness of a solution $\mathcal{A}$ of (A.7) under the assumed hypotheses. Given $\boldsymbol{\alpha} = (\alpha_1, \alpha_2) \in \mathbb{T}^2$, the definition (A.1) gives

$$\xi_\alpha(\alpha_1, t\,;\, 0, \alpha_2 - k\alpha_1, 0) = 1 + [\partial_{\alpha_1} + k\partial_{\alpha_2}]\tilde{\xi}(\alpha_1, \alpha_2, t), \tag{A.10}$$

where the left-hand side means $(d/d\alpha)\big|_{\alpha=\alpha_1} \xi(\alpha, t\,;\, 0, \alpha_2 - k\alpha_1, 0)$. We know the right-hand side is periodic and continuous on $\mathbb{T}^2$ while the left-hand is positive on the primitive cell $\{(\alpha_1, \alpha_2) : 0 \leq \alpha_1 < 2\pi\ ,\ k\alpha_1 \leq \alpha_2 < k\alpha_1 + 2\pi\}$. Therefore, both sides of (A.10) are bounded below by some $\varepsilon(t) > 0$ that does not depend on $\boldsymbol{\alpha} \in \mathbb{T}^2$. Let $M(t)$ be a bound on $|\tilde{\xi}(\boldsymbol{\alpha}, t)|$ over $\mathbb{T}^2$. Then for fixed $\boldsymbol{x} \in \mathbb{R}^2$ (with t also fixed), the function $g(\alpha) = g(\alpha; \boldsymbol{x}, t) = \alpha + \tilde{\xi}(\boldsymbol{x} + \boldsymbol{k}\alpha, t)$ is strictly monotonically increasing on $\mathbb{R}$ (as $g'(\alpha) \geq \varepsilon(t)$) and satisfies $g(-M(t)) \leq 0$ and $g(M(t)) \geq 0$. Thus, we can define $\mathcal{A}(\boldsymbol{x}, t)$ as the unique solution of $g(\alpha) = 0$. It follows that $|\mathcal{A}(\boldsymbol{x}, t)| \leq M(t)$. If n_1 and n_2 are integers, replacing $\boldsymbol{x}$ in (A.7) by $\boldsymbol{y} = (y_1, y_2) = (x_1 + 2\pi n_1, x_2 + 2\pi n_2)$ and using periodicity of $\tilde{\xi}(\boldsymbol{\alpha}, t)$ gives

$$\mathcal{A}(\boldsymbol{y}, t) + \tilde{\xi}\big(\boldsymbol{x} + \boldsymbol{k}\mathcal{A}(\boldsymbol{y}, t), t\big) = 0. \tag{A.11}$$

Since the solution of this equation is unique, $\mathcal{A}(\boldsymbol{y}, t) = \mathcal{A}(\boldsymbol{x}, t)$. This shows that $\mathcal{A}(\boldsymbol{x}, t)$ is periodic in $\boldsymbol{x}$, and hence well-defined on $\mathbb{T}^2$. It is also real analytic, which follows from the implicit function theorem, noting that $g(\alpha; x_1, x_2, t)$ is real analytic in α, x_1 and x_2 for

fixed t and $\partial g/\partial\alpha$ is never zero. For the same reason, $\mathcal{A}(\boldsymbol{x},t)$ will depend as smoothly on t as $\tilde{\xi}(\boldsymbol{\alpha},t)$ does. □

The change of variables (A.8) allows us transform the torus functions $\tilde{\xi}$, $\tilde{\eta}$ and $\tilde{\varphi}$ in conformal space to physical space

$$\begin{aligned} \tilde{\eta}^{\text{phys}}(\boldsymbol{x},t) &= \tilde{\eta}(\boldsymbol{x}+\boldsymbol{k}\mathcal{A}(\boldsymbol{x},t),\,t), & \tilde{\eta}(\boldsymbol{\alpha},t) &= \tilde{\eta}^{\text{phys}}(\boldsymbol{\alpha}+\boldsymbol{k}\tilde{\xi}(\boldsymbol{\alpha},t),\,t),\\ \tilde{\varphi}^{\text{phys}}(\boldsymbol{x},t) &= \tilde{\varphi}(\boldsymbol{x}+\boldsymbol{k}\mathcal{A}(\boldsymbol{x},t),\,t), & \tilde{\varphi}(\boldsymbol{\alpha},t) &= \tilde{\varphi}^{\text{phys}}(\boldsymbol{\alpha}+\boldsymbol{k}\tilde{\xi}(\boldsymbol{\alpha},t),\,t). \end{aligned} \tag{A.12}$$

We then write $\boldsymbol{\theta}=(\theta_1,\theta_2)$ and define the quasi-periodic slices

$$\begin{aligned} \eta^{\text{phys}}(x,t\,;\,\boldsymbol{\theta},\delta) &= \tilde{\eta}^{\text{phys}}\big(\boldsymbol{\theta}+\boldsymbol{k}(x-\delta)\,,\,t\big),\\ \varphi^{\text{phys}}(x,t\,;\,\boldsymbol{\theta},\delta) &= \tilde{\varphi}^{\text{phys}}\big(\boldsymbol{\theta}+\boldsymbol{k}(x-\delta)\,,\,t\big), \end{aligned} \tag{A.13}$$

which express $\zeta(\alpha,t\,;\,\boldsymbol{\theta},\delta)$ as a graph and $\varphi(\alpha,t\,;\,\boldsymbol{\theta})$ as a function of x:

$$\begin{aligned} \eta(\alpha,t\,;\,\boldsymbol{\theta},\delta) &= \tilde{\eta}(\boldsymbol{\theta}+\boldsymbol{k}\alpha,\,t)\\ &= \tilde{\eta}^{\text{phys}}\big(\boldsymbol{\theta}+\boldsymbol{k}\alpha+\boldsymbol{k}\tilde{\xi}(\boldsymbol{\theta}+\boldsymbol{k}\alpha,t),\,t\big)\\ &= \tilde{\eta}^{\text{phys}}\big(\boldsymbol{\theta}+\boldsymbol{k}(\xi(\alpha)-\delta),\,t\big)=\eta^{\text{phys}}\big(\xi(\alpha),t\,;\,\boldsymbol{\theta},\delta\big), \end{aligned} \tag{A.14}$$

$$\varphi(\alpha,t\,;\,\boldsymbol{\theta}) = \tilde{\varphi}^{\text{phys}}(\boldsymbol{\theta}+\boldsymbol{k}(\xi(\alpha)-\delta),\,t)=\varphi^{\text{phys}}\big(\xi(\alpha),t\,;\,\boldsymbol{\theta},\delta\big), \tag{A.15}$$

where $\xi(\alpha)=\xi(\alpha,t\,;\,\boldsymbol{\theta},\delta)=\alpha+\delta+\tilde{\xi}(\boldsymbol{\theta}+\boldsymbol{k}\alpha,t)$. These equations confirm (2.60) and (2.65), which are the assumptions connecting solutions of (2.15) to those of (2.78). Thus, $\eta^{\text{phys}}(x,t\,;\,\boldsymbol{\theta},\delta)$ and $\varphi^{\text{phys}}(x,t\,;\,\boldsymbol{\theta},\delta)$ are solutions of (2.15), the graph-based formulation of the water wave equations. In the right-hand sides of (A.14) and (A.15), we can compute the α such that $\xi(\alpha)=x$ as follows:

$$\begin{aligned} \xi(\alpha,t\,;\,\boldsymbol{\theta},\delta)=x \quad &\Leftrightarrow \quad \alpha+\delta+\tilde{\xi}(\boldsymbol{\theta}+\boldsymbol{k}\alpha,t)=x\\ &\Leftrightarrow \quad (\boldsymbol{\theta}+\boldsymbol{k}\alpha)+\boldsymbol{k}\tilde{\xi}(\boldsymbol{\theta}+\boldsymbol{k}\alpha,t)=[\boldsymbol{\theta}+\boldsymbol{k}(x-\delta)]\\ &\Leftrightarrow \quad (\boldsymbol{\theta}+\boldsymbol{k}\alpha)=[\boldsymbol{\theta}+\boldsymbol{k}(x-\delta)]+\boldsymbol{k}\mathcal{A}\big(\boldsymbol{\theta}+\boldsymbol{k}(x-\delta),t\big)\\ &\Leftrightarrow \quad \alpha=(x-\delta)+\mathcal{A}(\boldsymbol{\theta}+\boldsymbol{k}(x-\delta),t), \end{aligned} \tag{A.16}$$

where we used (A.8) with $\boldsymbol{\alpha}=\boldsymbol{\theta}+\boldsymbol{k}\alpha$ and $\boldsymbol{x}=\boldsymbol{\theta}+\boldsymbol{k}(x-\delta)$ to obtain the third line from the second.

A.2 Dynamics of Traveling Waves in Conformal Space

In this section we study the dynamics of quasi-periodic traveling waves under the evolution equations (2.78) for various choices of C_1. We show that the waves maintain a permanent form but generally travel at a non-uniform speed in conformal space. We start by showing that there is a choice of C_1 for which η and φ remain stationary in time.

We then show how C_1 changes when the waves are phase shifted by $\alpha_0(t)$, and how to determine $\alpha_0(t)$ so that C_1 takes the value in (2.80). The evolution of the torus version of (3.5) under (2.78) is also worked out.

We will need the following theorem and corollary, proved in [84]:

Theorem A.2.1 *Suppose $\varepsilon > 0$ and $z(w)$ is analytic on the half-plane $\mathbb{C}_\varepsilon^- = \{w : \operatorname{Im} w < \varepsilon\}$. Suppose there is a constant $M > 0$ such that $|z(w) - w| \le M$ for $w \in \mathbb{C}_\varepsilon^-$, and that the restriction $\zeta = z|_{\mathbb{R}}$ is injective. Then the curve $\zeta(\alpha)$ separates the complex plane into two regions, and $z(w)$ is an analytic isomorphism of the lower half-plane onto the region below the curve $\zeta(\alpha)$.*

Corollary A.2.2 *Suppose $k > 0$ is irrational, $\tilde\eta(\alpha_1, \alpha_2) = \sum_{(j_1,j_2)\in\mathbb{Z}^2} \hat\eta_{j_1,j_2} e^{i(j_1\alpha_1 + j_2\alpha_2)}$, and there exist constants C and $\varepsilon > 0$ such that*

$$\hat\eta_{-j_1,-j_2} = \overline{\hat\eta_{j_1,j_2}}, \qquad |\hat\eta_{j_1,j_2}| \le Ce^{-3\varepsilon K \max(|j_1|,|j_2|)}, \qquad (j_1, j_2) \in \mathbb{Z}^2, \tag{A.17}$$

where $K = \max(k, 1)$. Let x_0 be real and define $\tilde\xi = x_0 + H[\tilde\eta]$, $\tilde\zeta = \tilde\xi + i\tilde\eta$ and

$$\tilde z(\alpha_1, \alpha_2, \beta) = x_0 + i\hat\eta_{0,0} + \sum_{j_1+j_2k<0} 2i\hat\eta_{j_1,j_2} e^{-(j_1+j_2k)\beta} e^{i(j_1\alpha_1+j_2\alpha_2)}, \qquad (\beta < \varepsilon), \tag{A.18}$$

where the sum is over all integer pairs (j_1, j_2) satisfying the inequality. Suppose also that for each fixed $\theta \in [0, 2\pi)$, the function $\alpha \mapsto \zeta(\alpha; \theta) = \alpha + \tilde\zeta(\alpha, \theta + k\alpha)$ is injective from $\mathbb{R}$ to $\mathbb{C}$ and $\zeta_\alpha(\alpha; \theta) \ne 0$ for $\alpha \in \mathbb{R}$. Then for each $\theta \in \mathbb{R}$, the curve $\zeta(\alpha; \theta)$ separates the complex plane into two regions and

$$z(\alpha + i\beta; \theta) = (\alpha + i\beta) + \tilde z(\alpha, \theta + k\alpha, \beta), \qquad (\beta < \varepsilon) \tag{A.19}$$

is an analytic isomorphism of the lower half-plane onto the region below $\zeta(\alpha; \theta)$. Moreover, there is a constant $\delta > 0$ such that $|z_w(w; \theta)| \ge \delta$ for $\operatorname{Im} w \le 0$ and $\theta \in \mathbb{R}$.

We now prove a theorem and two corollaries that describe the dynamics of traveling waves in conformal space under the evolution equations (2.78) for various choices of C_1.

Theorem A.2.3 *Suppose $\tilde\eta_0(\alpha_1, \alpha_2)$ satisfies the torus version of (3.5) as well as the assumptions in Corollary A.2.2. Define $\tilde\xi_0 = H[\tilde\eta_0]$, $\tilde\zeta_0 = \tilde\xi_0 + i\tilde\eta_0$ and $\tilde\varphi_0 = c\tilde\xi_0$. Let $\eta_0(\alpha; \theta) = \tilde\eta_0(\alpha, \theta + k\alpha)$, $\varphi_0(\alpha; \theta) = \tilde\varphi_0(\alpha, \theta + k\alpha)$, $\xi_0(\alpha; \theta) = \alpha + \tilde\xi_0(\alpha, \theta + k\alpha)$ and $\zeta_0 = \xi_0 + i\eta_0$. Suppose that for each $\theta \in [0, 2\pi)$, $\alpha \mapsto \zeta_0(\alpha; \theta)$ is injective, i.e. none of the curves in the family (A.1) self-intersect. Then for each $\theta \in \mathbb{R}$,*

$$\zeta(\alpha, t; \theta) = \zeta_0(\alpha; \theta) + ct, \qquad \varphi(\alpha, t; \theta) = \varphi_0(\alpha; \theta) \tag{A.20}$$

satisfy (2.78) with $C_1 = cP_0[\xi_\alpha/J]$.

Proof: We have assumed the initial reconstruction of ξ from η yields $\xi(\alpha,0;\theta)=\xi_0(\alpha;\theta)$, so $x_0(0)=0$ in (2.62). We need to show that $\eta_t=0$, $\varphi_t=0$ and $dx_0/dt=c$ in (2.78), from which it follows that $\xi(\alpha,t;\theta)=\xi_0(\alpha;\theta)+ct$. Since $\tilde\xi_0=H[\tilde\eta_0]$ and none of the curves in the family (A.3) self-intersect, Theorem A.2.1 and Corollary A.2.2 above show that the holomorphic extension from $\zeta_0(\alpha;\theta)$ to $z_0(w;\theta)$ is an analytic isomorphism of the lower half-plane to the fluid region, and $1/|z_{0,w}|$ is uniformly bounded. In (2.78), we define $\xi_\alpha=1+H[\eta_\alpha]$, $\psi=-H[\varphi]$, $J=\xi_\alpha^2+\eta_\alpha^2$ and $\chi=\psi_\alpha/J$. This formula for ξ_α gives the same result as differentiating $\xi(\alpha,t;\theta)$ in (A.20) with respect to α. From $\tilde\varphi_0=c\tilde\xi_0$ and $\hat\eta_{0,0}=0$, we have $\chi=c\eta_\alpha/J$. The extension of $\zeta(\alpha,t;\theta)$ to the lower half-plane is $z(w,t;\theta)=[z_0(w;\theta)+ct]$. We have not yet established that $\zeta(\alpha,t;\theta)$ solves (2.78), but we know z_t/z_w is bounded in the lower half-plane, so there is a C_1 such that

$$\begin{pmatrix}-H\chi+C_1\\ -\chi\end{pmatrix}=\frac{1}{J}\begin{pmatrix}\xi_\alpha & \eta_\alpha\\ -\eta_\alpha & \xi_\alpha\end{pmatrix}\begin{pmatrix}c\\0\end{pmatrix}, \tag{A.21}$$

where the right-hand side represents complex division of z_t by z_α. Since $P_0H\chi=0$, we learn from (A.21) that $C_1=cP_0[\xi_\alpha/J]$. But ξ_t and η_t in (2.74) are obtained by multiplying (A.21) by $[\xi_\alpha,-\eta_\alpha;\eta_\alpha,\xi_\alpha]$, which gives $\xi_t=c$, $\eta_t=0$. Equation (2.75) is then $dx_0/dt=P_0[\xi_t]=c$. Finally, using $\chi=c\eta_\alpha/J$, $H\chi=C_1-c\xi_\alpha/J$, $\varphi_\alpha=c(\xi_\alpha-1)$ and $\psi_\alpha=c\eta_\alpha$ in (2.78) gives

$$\begin{aligned}\varphi_t&=P\Big[\frac{\psi_\alpha^2-\varphi_\alpha^2}{2J}-\varphi_\alpha H[\chi]+C_1\varphi_\alpha-g\eta+\tau\kappa\Big]\\&=P\Big[\frac{c^2\eta_\alpha^2-c^2(\xi_\alpha^2-2\xi_\alpha+1)}{2J}+c\frac{c(\xi_\alpha-1)\xi_\alpha}{J}-g\eta+\tau\kappa\Big]\\&=P\Big[\frac{c^2}{2J}\big(J-1\big)-g\eta+\tau\kappa\Big]=P\Big[-\frac{c^2}{2J}-g\eta+\tau\kappa\Big]=0,\end{aligned} \tag{A.22}$$

where we used (3.5) in the last step. □

Corollary A.2.4 *Suppose $\tilde\zeta_0(\alpha_1,\alpha_2)$, $\tilde\varphi_0(\alpha_1,\alpha_2)$, $\zeta_0(\alpha;\theta)$ and $\varphi_0(\alpha;\theta)$ satisfy the hypotheses of Theorem A.2.3 and $\alpha_0(t)$ is any continuously differentiable, real-valued function. Then*

$$\zeta(\alpha,t;\theta)=\zeta_0(\alpha-\alpha_0(t);\theta)+ct,\qquad \varphi(\alpha,t;\theta)=\varphi_0(\alpha-\alpha_0(t);\theta) \tag{A.23}$$

are solutions of (2.78) with $C_1=cP_0[\xi_\alpha/J]-\alpha_0'(t)$. The corresponding solutions of the torus version of (2.78) for this choice of C_1 are

$$\begin{aligned}\tilde\zeta(\alpha_1,\alpha_2,t)&=\tilde\zeta_0\big(\alpha_1-\alpha_0(t),\alpha_2-k\alpha_0(t)\big)+ct-\alpha_0(t),\\ \tilde\varphi(\alpha_1,\alpha_2,t)&=\tilde\varphi_0\big(\alpha_1-\alpha_0(t),\alpha_2-k\alpha_0(t)\big).\end{aligned} \tag{A.24}$$

Proof: Since ∂_α and H commute with α-translations, substitution of $\eta_0(\alpha - \alpha_0(t); \theta)$ and $\varphi_0(\alpha - \alpha_0(t); \theta)$ in the right-hand sides of (2.78) without changing C_1 would still lead to $\eta_t = 0$, $\varphi_t = 0$ and $dx_0/dt = c$, and (2.74) would still give $\xi_t = c$. Including $-\alpha_0'(t)$ in C_1 leads instead to $\eta_t = -\alpha_0'(t)\eta_\alpha$ and $\varphi_t = -\alpha_0'(t)\varphi_\alpha$ in (2.78) and $\xi_t = c - \alpha_0'(t)\xi_\alpha$ in (2.74), which are satisfied by (A.23). It also leads to $dx_0/dt = [c - \alpha_0'(t)]$ in (2.75), which keeps the reconstruction of ξ from η via (2.62) consistent with the evolution equation for ξ_t.

The functions in (A.23) and (A.24) are related by

$$\zeta(\alpha, t; \theta) = \alpha + \tilde{\zeta}(\alpha, \theta + k\alpha, t), \qquad \varphi(\alpha, t; \theta) = \tilde{\varphi}(\alpha, \theta + k\alpha, t). \tag{A.25}$$

Applying the 1d version of (2.78) to (A.25) is equivalent to applying the torus version of (2.78) to (A.24) and evaluating at $(\alpha, \theta + k\alpha, t)$. Since (A.23) satisfies the 1d version of (2.78) and every point $(\alpha_1, \alpha_2) \in \mathbb{T}^2$ can be written as $(\alpha, \theta + k\alpha)$ for some α and θ, (A.24) satisfies the torus version of (2.78). □

Corollary A.2.5 *Suppose $\tilde{\zeta}_0(\alpha_1, \alpha_2)$, $\tilde{\varphi}_0(\alpha_1, \alpha_2)$, $\zeta_0(\alpha; \theta)$ and $\varphi_0(\alpha; \theta)$ satisfy the hypotheses of Theorem A.2.3 and $\xi_{0,\alpha}(\alpha; \theta) > 0$ for $\alpha \in [0, 2\pi)$ and $\theta \in [0, 2\pi)$. Then if C_1 is chosen as in (2.80) to maintain $\tilde{\xi}(0, 0, t) = 0$, the solution of the torus version of (2.78) with initial conditions*

$$\tilde{\zeta}(\alpha_1, \alpha_2, 0) = \tilde{\zeta}_0(\alpha_1, \alpha_2), \qquad \tilde{\varphi}(\alpha_1, \alpha_2, 0) = \tilde{\varphi}_0(\alpha_1, \alpha_2) \tag{A.26}$$

has the form (A.24) with

$$\alpha_0(t) = ct - \mathcal{A}_0(-ct, -kct), \tag{A.27}$$

where $\mathcal{A}_0(x_1, x_2)$ is defined implicitly by

$$\mathcal{A}_0(x_1, x_2) + \tilde{\xi}_0\big(x_1 + \mathcal{A}_0(x_1, x_2)\,,\; x_2 + k\mathcal{A}_0(x_1, x_2)\big) = 0, \qquad (x_1, x_2) \in \mathbb{T}^2. \tag{A.28}$$

Proof: The assumption that $\xi_{0,\alpha}(\alpha; \theta) > 0$ ensures that all the waves in the family $\zeta_0(\alpha; \theta)$ are single-valued and have no vertical tangent lines. Under these hypotheses, it is proved in Theorem A.1.2 that there is a unique function $\mathcal{A}_0(x_1, x_2)$ satisfying (A.28) and that it is real analytic and periodic. We seek a solution of the form (A.24) satisfying $\tilde{\xi}(0, 0, t) = 0$,

$$\begin{aligned} \tilde{\xi}(0, 0, t) &= \tilde{\xi}_0(-\alpha_0(t), -k\alpha_0(t)) + ct - \alpha_0(t) \\ &= [ct - \alpha_0(t)] + \tilde{\xi}_0\big(-ct + [ct - \alpha_0(t)], -kct + k[ct - \alpha_0(t)]\big) = 0. \end{aligned} \tag{A.29}$$

Comparing with (A.28), we find that $[ct - \alpha_0(t)] = \mathcal{A}_0(-ct, -kct)$, which is (A.27). Since $\tilde{\eta}_0(\alpha_1, \alpha_2)$ is even, $\tilde{\xi}_0 = H[\tilde{\eta}_0]$ is odd and $\mathcal{A}_0(0, 0) = 0$. Thus, $\alpha_0(0) = 0$ and the initial conditions (A.26) are satisfied. Since $\xi(0, 0, t) = 0$, C_1 satisfies (2.80). □

Bibliography

[1] M. J. Ablowitz and T. P. Horikis. Interacting nonlinear wave envelopes and rogue wave formation in deep water. *Phys. Fluids*, 27(1):012107, 2015.

[2] B. F. Akers, D. M. Ambrose, and D. W. Sulon. Periodic travelling interfacial hydroelastic waves with or without mass II: Multiple bifurcations and ripples. *Eur. J. Appl.*, 30(4):756–790, 2019.

[3] B. F. Akers, D. M. Ambrose, and J. D. Wright. Gravity perturbed crapper waves. *Proc. R. Soc. A.*, 470(2161):20130526, 2014.

[4] B. F. Akers and P. A. Milewski. Model equations for gravity-capillary waves in deep water. *Stud. Appl. Math.*, 121(1):49–69, 2008.

[5] B. F. Akers and D. P. Nicholls. Wilton ripples in weakly nonlinear dispersive models of water waves: Existence and analyticity of solution branches. *Water Waves*, 3:25–47, 2021.

[6] E. L. Allgower and K. Georg. *Numerical continuation methods: An introduction*, volume 13. Springer Science & Business Media, 2012.

[7] D. M. Ambrose, R. Camassa, J. L. Marzuola, R. McLaughlin, Q. Robinson, and J. Wilkening. Numerical algorithms for water waves with background flow over obstacles and topography. 2020. (in preparation).

[8] D. M. Ambrose and J. Wilkening. Computation of symmetric, time-periodic solutions of the vortex sheet with surface tension. *Proc. Natl. Acad. Sci. U.S.A.*, 107(8):3361–3366, 2010.

[9] D. M. Ambrose and J. Wilkening. Dependence of time-periodic vortex sheets with surface tension on mean vortex sheet strength. *Procedia IUTAM*, 11:15–22, 2014.

[10] L. Amerio and G. Prouse. *Almost-Periodic Functions and Functional Equations*. Springer, New York, 1971.

[11] C. Aurther, R. Granero-Belinchón, S. Shkoller, and J. Wilkening. Rigorous asymptotic models of water waves. *Water Waves*, 1:71–130, 2019.

[12] S. Axler, P. Bourdon, and W. Ramey. *Harmonic Function Theory*. Springer-Verlag, New York, 1992.

[13] P. Baldi, M. Berti, E. Haus, and R. Montalto. Time quasi-periodic gravity water waves in finite depth. *Invent. Math.*, 214(2):739–911, 2018.

[14] T. B. Benjamin and J. Feir. The disintegration of wave trains on deep water. *J. Fluid Mech.*, 27(3):417–430, 1967.

[15] H. Berland, B. Owren, and B. Skaflestad. B-series and order conditions for exponential integrators. *SIAM J. Numer. Anal.*, 43(4):1715–1727, 2005.

[16] M. Berti, L. Franzoi, and A. Maspero. Traveling quasi-periodic water waves with constant vorticity, 2020. arXiv:2004.08905.

[17] M. Berti and R. Montalto. *Quasi-periodic standing wave solutions of gravity-capillary water waves*, volume 263 of *Mem. Am. Math. Soc.* American Mathematical Society, 2016.

[18] H. Bohr. *Almost Periodic Functions*. Dover, Mineola, New York, 2018.

[19] T. J. Bridges and F. Dias. Spatially quasi-periodic capillary-gravity waves. *Contemp. Math.*, 200:31–46, 1996.

[20] T. J. Bridges and A. Mielke. A proof of the benjamin-feir instability. *Arch. Ration. Mech. Anal.*, 133(2):145–198, 1995.

[21] H. Broer and F. Takens. *Dynamical Systems and Chaos*, volume 172 of *Appl. Math. Sci.* Springer, New York, 2011.

[22] B. Buffoni, E. Dancer, and J. Toland. The sub-harmonic bifurcation of stokes waves. *Arch. Ration. Mech. Anal.*, 152(3):241–271, 2000.

[23] B. Chen and P. Saffman. Steady gravity-capillary waves on deep water – 1. weakly nonlinear waves. *Stud. Appl. Math.*, 60(3):183–210, 1979.

[24] B. Chen and P. Sallman. Numerical evidence for the existence of new types of gravity waves of permanent form on deep water. *Stud. Appl. Math.*, 62(1):1–21, 1980.

[25] J. Chen and J. Wilkening. Arbitrary-order exponential time differencing schemes via Chebyshev moments of exponential functions. 2020. (in preparation).

[26] W. Choi and R. Camassa. Exact evolution equations for surface waves. *J. Eng. Mech.*, 125(7):756–760, 1999.

[27] A. J. Chorin, J. E. Marsden, and J. E. Marsden. *A mathematical introduction to fluid mechanics*, volume 168. Springer, 1990.

[28] S. Cox and P. Matthews. Exponential time differencing for stiff systems. *J. Comput. Phys.*, 176(2):430–455, 2002.

[29] W. Craig and C. Sulem. Numerical simulation of gravity waves. *J. Comput. Phys.*, 108:73–83, 1993.

[30] D. Damanik and M. Goldstein. On the existence and uniqueness of global solutions for the kdv equation with quasi-periodic initial data. *J. Amer. Math. Soc.*, 29(3):825–856, 2016.

[31] B. Deconinck and K. Oliveras. The instability of periodic surface gravity waves. *J. Fluid Mech.*, 675:141–167, 2011.

[32] B. Dodson, A. Soffer, and T. Spencer. The nonlinear schrödinger equation on z and r with bounded initial data: Examples and conjectures. *J. Stat. Phys.*, 180(1):910–934, 2020.

[33] A. I. Dyachenko. On the dynamics of an ideal fluid with a free surface. *Dokl. Math.*, 63(1):115–117, 2001.

[34] A. I. Dyachenko, E. A. Kuznetsov, M. Spector, and V. E. Zakharov. Analytical description of the free surface dynamics of an ideal fluid (canonical formalism and conformal mapping). *Phys. Lett. A*, 221(1-2):73–79, 1996.

[35] A. I. Dyachenko, P. M. Lushnikov, and V. Zakharov. Non-canonical Hamiltonian structure and Poisson bracket for two-dimensional hydrodynamics with free surface. *J. Fluid Mech.*, 869:526–552, 2019.

[36] A. I. Dyachenko, V. E. Zakharov, and E. A. Kuznetsov. Nonlinear dynamics of the free surface of an ideal fluid. *Plasma Phys. Rep.*, 22(10):829–840, 1996.

[37] S. A. Dyachenko. On the dynamics of a free surface of an ideal fluid in a bounded domain in the presence of surface tension. *J. Fluid. Mech.*, 860:408–418, 2019.

[38] S. A. Dyachenko, P. M. Lushnikov, and A. O. Korotkevich. Branch cuts of stokes wave on deep water. Part I: Numerical solution and Padé approximation. *Stud. Appl. Math.*, 137(4):419–472, 2016.

[39] S. A. Dyachenko and A. C. Newell. Whitecapping. *Studies Appl. Math.*, 137:199–213, 2016.

[40] I. A. Dynnikov and S. P. Novikov. Topology of quasi-periodic functions on the plane. *Russ. Math. Surv.*, 60(1):1, 2005.

[41] R. Feola and F. Giuliani. Quasi-periodic traveling waves on an infinitely deep perfect fluid under gravity, 2020. arXiv:2005.08280.

[42] A. M. Fink. *Almost Periodic Differential Equations*. Lecture Notes in Mathematics. Springer-Verlag, Berlin, 1974.

[43] S. Govindjee, T. Potter, and J. Wilkening. Cyclic steady states of treaded rolling bodies. *Int. J. Numer. Meth. Eng*, 99(3):203–220, 2014.

[44] E. Hairer, S. P. Norsett, and G. Wanner. *Solving Ordinary Differential Equations I: Nonstiff Problems*. Springer, Berlin, 2nd edition, 2000.

[45] Y. Hino, T. Naito, N. V. Minh, and J. S. Shin. *Almost Periodic Solutions of Differential Equations in Banach Spaces*. Taylor and Francis, New York, 2002.

[46] T. Y. Hou and R. Li. Computing nearly singular solutions using pseudo-spectral methods. *J. Comput. Phys.*, 226:379–397, 2007.

[47] T. Y. Hou, J. S. Lowengrub, and M. J. Shelley. Removing the stiffness from interfacial flows with surface tension. *J. Comput. Phys.*, 114:312–338, 1994.

[48] T. Y. Hou, J. S. Lowengrub, and M. J. Shelley. Boundary integral methods for multicomponent fluids and multiphase materials. *J. Comput. Phys.*, 169:302–362, 2001.

[49] J. K. Hunter, M. Ifrim, and D. Tataru. Two dimensional water waves in holomorphic coordinates. *Comm. Math. Phys.*, 346(2):483–552, 2016.

[50] G. Iooss and P. I. Plotnikov. *Small divisor problem in the theory of three-dimensional water gravity waves*, volume 200 of *Mem. Am. Math. Soc.* American Mathematical Society, 2009.

[51] G. Iooss, P. I. Plotnikov, and J. F. Toland. Standing waves on an infinitely deep perfect fluid under gravity. *Arch. Rat. Mech. Anal.*, 177:367–478, 2005.

[52] P. A. Janssen. Nonlinear four-wave interactions and freak waves. *J. Phys. Oceanogr.*, 33(4):863–884, 2003.

[53] A.-K. Kassam and L. N. Trefethen. Fourth-order time-stepping for stiff PDEs. *SIAM J. Sci. Comput.*, 26(4):1214–1233, 2005.

[54] P. Lax. Almost periodic solutions of the KdV equation. *SIAM Rev.*, 18(3):351–375, 1976.

[55] T. Levi-Civita. Determination rigoureuse des ondes permanentes d'ampleur finie. *Math. Ann.*, 93(1):264–314, 1925.

[56] Y. A. Li, J. M. Hyman, and W. Choi. A numerical study of the exact evolution equations for surface waves in water of finite depth. *Stud. Appl. Math.*, 113(3):303–324, 2004.

[57] M. S. Longuet-Higgins. The instabilities of gravity waves of finite amplitude in deep water. II. Subharmonics. *Proc. R. Soc. Lond. A*, 360:489–505, 1978.

[58] D. I. Meiron, S. A. Orszag, and M. Israeli. Applications of numerical conformal mapping. *J. Comput. Phys.*, 40(2):345–360, 1981.

[59] P. A. Milewski, J.-M. Vanden-Broeck, and Z. Wang. Dynamics of steep two-dimensional gravity–capillary solitary waves. *J. Fluid Mech.*, 664:466–477, 2010.

[60] P. A. Milewski, J.-M. Vanden-Broeck, and Z. Wang. Two-dimensional flexural–gravity waves of finite amplitude in deep water. *IMA J. Appl. Math.*, 78(4):750–761, 2013.

[61] L. M. Milne-Thomson. *Theoretical Hydrodynamics*. MacMillan, London, 5th edition, 1968.

[62] J. Moser. On the theory of quasiperiodic motions. *SIAM Rev.*, 8(2):145–172, 1966.

[63] A. I. Nekrasov. On steady waves. *Izv. Ivanovo-Voznesensk. Politekhn. In-ta*, 3:52–65, 1921.

[64] H. Q. Nguyen and W. A. Strauss. Proof of modulational instability of stokes waves in deep water. *arXiv preprint arXiv:2007.05018*, 2020.

[65] J. Nocedal and S. J. Wright. *Numerical Optimization*. Springer, New York, 1999.

[66] M. Onorato, A. R. Osborne, and M. Serio. Modulational instability in crossing sea states: A possible mechanism for the formation of freak waves. *Phys. Rev. Lett.*, 96(1):014503, 2006.

[67] A. R. Osborne, M. Onorato, and M. Seria. The nonlinear dynamics of rogue waves and holes in deep-water gravity wave trains. *Phys. Letters A*, 275:386–393, 2000.

[68] P. Plotnikov and J. Toland. Nash-moser theory for standing water waves. *Arch. Rat. Mech. Anal.*, 159:1–83, 2001.

[69] C. H. Rycroft and J. Wilkening. Computation of three-dimensional standing water waves. *J. Comput. Phys*, 255:612–638, 2013.

[70] G. G. Stokes. On the theory of oscillatory waves. *Trans. Cambridge Philos. Soc.*, 8:441–455, 1880.

[71] D. J. Struik. Détermination rigoureuse des ondes irrotationelles périodiques dans un canal à profondeur finie. *Math. Ann.*, 95(1):595–634, 1926.

[72] R. Tiron and W. Choi. Linear stability of finite-amplitude capillary waves on water of infinite depth. *J. Fluid Mech.*, 696:402, 2012.

[73] O. Trichtchenko, B. Deconinck, and J. Wilkening. The instability of Wilton's ripples. *Wave Motion*, 66:147–155, 2016.

[74] M. R. Turner and T. J. Bridges. Time-dependent conformal mapping of doubly-connected regions. *Adv. Comput. Math.*, 42:947–972, 2016.

[75] J.-M. Vanden-Broeck. *Gravity–Capillary Free–Surface Flows*. Cambridge University Press, Cambridge, 2010.

[76] J.-M. Vanden-Broeck. On periodic and solitary pure gravity waves in water of infinite depth. *J. Eng. Math.*, 84(1):173–180, 2014.

[77] J.-M. Vanden-Broeck and F. Dias. Gravity-capillary solitary waves in water of infinite depth and related free-surface flows. *J. Fluid Mech.*, 240:549–557, 1992.

[78] C. Viotti, D. Dutykh, and F. Dias. The conformal-mapping method for surface gravity waves in the presence of variable bathymetry and mean current. *Procedia IUTAM*, 11:110–118, 2014.

[79] P. Whalen, M. Brio, and J. Moloney. Exponential time-differencing with embedded Runge–Kutta adaptive step control. *J. Comput. Phys.*, 280:579–601, 2015.

[80] J. Wilkening. Relative-periodic elastic collisions of water waves. *Contemp. Math.*, 635:109–129, 2015.

[81] J. Wilkening. Traveling-standing water waves. 2021. (in preparation).

[82] J. Wilkening and J. Yu. Overdetermined shooting methods for computing standing water waves with spectral accuracy. *Comput. Sci. Discov.*, 5(1):014017, 2012.

[83] J. Wilkening and X. Zhao. Quasi-periodic travelling gravity–capillary waves. *J. Fluid Mech.*, 2021. (accepted).

[84] J. Wilkening and X. Zhao. Spatially quasi-periodic water waves of infinite depth. *J. Nonlinear Sci.*, 2021. (accepted).

[85] J. R. Wilton. On ripples. *London, Edinburgh Dublin Philos. Mag. J. Sci.*, 29(173):688–700, 1915.

[86] V. E. Zakharov. Stability of periodic waves of finite amplitude on the surface of a deep fluid. *J. Appl. Mech. Tech. Phys.*, 9(2):190–194, 1968.

[87] V. E. Zakharov, A. I. Dyachenko, and O. A. Vasilyev. New method for numerical simulation of a nonstationary potential flow of incompressible fluid with a free surface. *Eur. J. Mech. B Fluids*, 21(3):283–291, 2002.